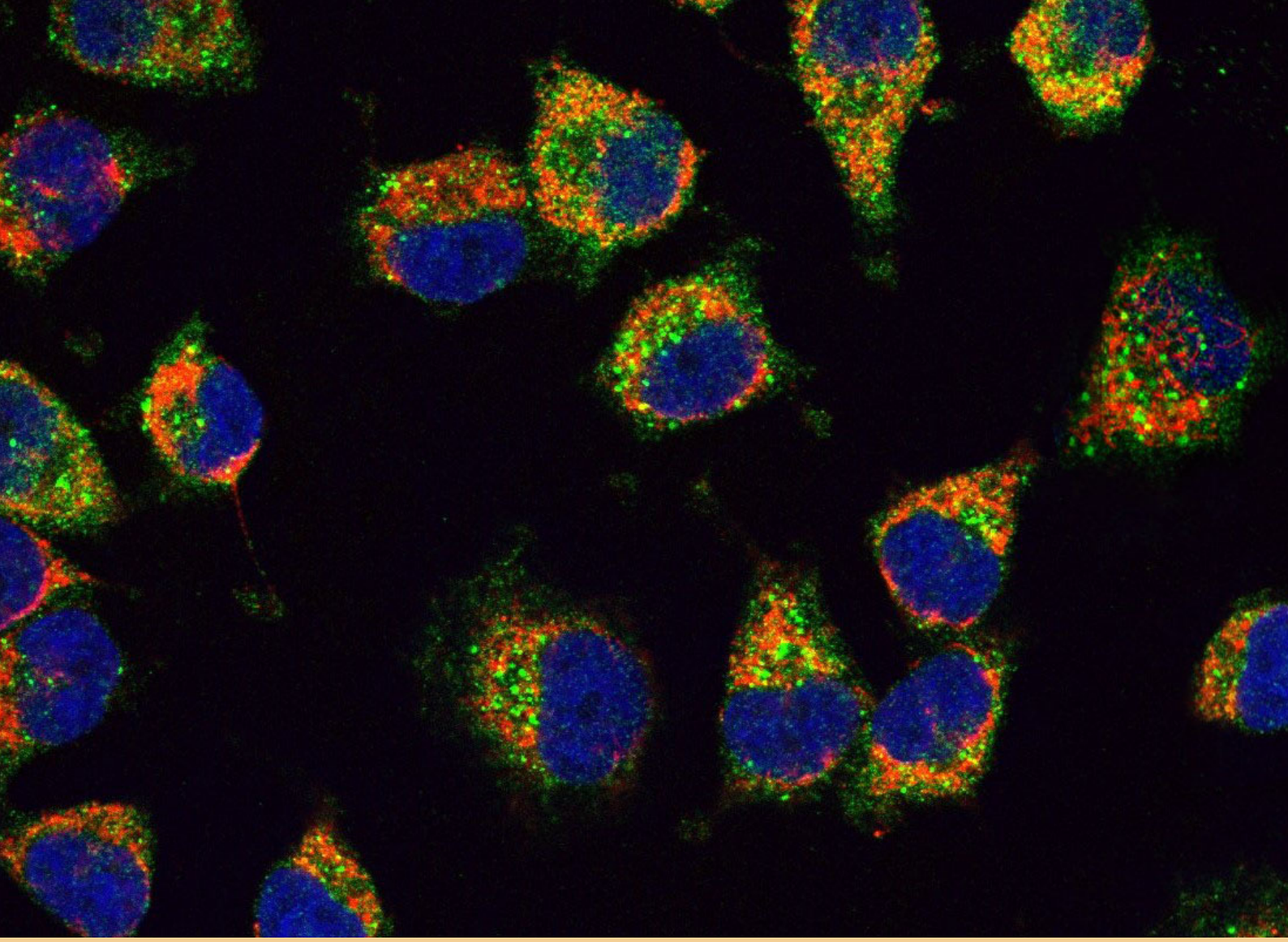

Filipa Luísa Lourenço de Almeida

Characterization of mitochondrial function and dynamics in models of Machado-Joseph disease

Dissertação para a obtenção do grau de Mestre em Investigação Biomédica sob a orientação científica da Professora Doutora Ana Cristina Rego e apresentada à Faculdade de Medicina da Universidade de Coimbra

2016

· U C ·

Universidade de Coimbra

Filipa Luísa Lourenço de Almeida

Characterization of mitochondrial function and dynamics in models of Machado-Joseph disease

Dissertação para a obtenção do grau de Mestre em Investigação Biomédica sob a orientação científica da Professora Doutora Ana Cristina Rego e apresentada à Faculdade de Medicina da Universidade de Coimbra

2016

UNIVERSIDADE DE COIMBRA

Figure on the cover:

Confocal images of PC6-3 Q108 cells obtained with a 63x objective, NA=1.4 on a Zeiss LSM 70 inverted microscope. Q108 cells were immunostained with an antibody for Hsp60 (red) to label mitochondria, an antibody for LC3 (green) and stained with Hoechst 33342 (blue) in order to visualize the nuclei.

Agradecimentos

Apesar de estar apenas um nome presente na capa, este trabalho reflete o empenho e a dedicação de um grande número de pessoas sem o qual nunca teria sido possível.

À minha orientadora, a Professora Doutora Ana Cristina Rego por me ter proporcionado a incrível oportunidade de integrar o grupo e da confiança que depositou em mim ao me inserir neste projeto. Por toda a disponibilidade e amabilidade que me demonstrou e por tudo o que me ajudou a aprender e a alcançar, um muito obrigado.

À Luana Naia, que apesar de não puder ser minha co-orientadora oficial, se embrenhou neste projeto e esteve comigo desde o início, que me ensinou, que me apoiou e que me ajudou a tornar numa pessoa e numa profissional melhor.

À Doutora Luísa Ferreira por toda a disponibilidade e ajuda que me prestou ao longo deste trabalho, especialmente nas experiências com os animais e nesta última fase de entrega da tese.

À Catarina Carmo, a minha colega de mesa, que apesar de não ter qualquer obrigação para comigo sempre se mostrou disponível para me ajudar e ensinar e foi sempre uma presença calorosa no laboratório.

À Carina Maranga e à Lígia Fão, as minhas companheiras de mestrado com as quais tive o prazer de partilhar este percurso. Não conseguia imaginar este último ano sem vocês.

A todas as pessoas do grupo MDSN (Sahana, Sandra, Carla, Mário, Elizabete, António e Diogo), pela vossa hospitalidade e disponibilidade, e por sempre me terem feito sentir bem-vinda.

À Doutora Patrícia Maciel pela sua colaboração e confiança ao ter fornecido os murganhos que acabaram por ser um elemento fundamental do meu trabalho.

À Sara Silva-Fernandes pela ajuda prestada em relação aos animais e pela disponibilidade que sempre demonstrou.

A todos os meus amigos de curso, de Torres Vedras, de Coimbra e colegas de casa que me apoiaram neste processo.

Aos meus colegas MIBs que, mais do que colegas, tornaram-se amigos, confidentes e companheiros de viagens inesquecíveis.

À minha família, especialmente aos meus pais e ao meu irmão, por me apoiarem incondicionalmente e confiarem nas minhas decisões.

Ao João, o meu pilar durante todo este percurso, aquele que me aturou mais do ninguém tanto nos bons e nos maus momentos e esteve sempre ao meu lado.

This work was supported by: ‘Fundo Europeu de Desenvolvimento Regional’ - FEDER funds through the ‘Programa Operacional Factores de Competitividade’ COMPETE, projects reference PEst-C/SAU/LA0001/2013-2014 and UID/NEU/04539/2013.

Table of contents

Abbreviations

AD - Alzheimer's disease

ADP - Adenosine diphosphate

AMP - Adenosine monophosphate

AntA - Antimycin A

ATP - Adenosine triphosphate

ATXN3 - Ataxin-3

Atg16L - Autophagic protein 16

Bax - Bcl2 associated X protein

BS - Brainstem

BSA - Bovine serum albumin

Ca^{2+} - Calcium

CB - Cerebellum

CBP - cAMP response element-binding protein

CCCP - Carbonyl cyanide 3-chlorophenylhydrazone

CK2 - Casein kinase 2

Drp1 - Dynamin-related protein 1

DRPLA - Dentatorubral-pallidoluysian atrophy

DTT - Dithiothreitol

ERAD - Endoplasmatic reticulum-associated degradation

FBS - Fetal bovine serum

FCCP - Carbonyl cyanide 4-(trifluoromethoxy) phenylhydrazone

Fis1 - Mitochondrial fission 1

FOXO - Forkhead box O

GSK 3 β - Glycogen synthase kinase 3β

GTP - Guanosine triphosphate

H^+ - Proton

H_2O_2 - Hydrogen peroxide

HD - Huntington's disease

HDAC - Histone deacetylase

HPLC - High-performance liquid chromatography

HRP - Horseradish Peroxidase

HRR - High-resolution respirometric

HS - Horse serum

Hsp - Heat shock protein

IMM - Inner mitochondrial membrane

IMS - Intermembrane space

KCN - Potassium cyanide

LC3 - Protein 1 light chain 3

LIR - LC3-interacting region

MAP2 - Microtubule associated protein 2

MAS - Mitochondrial assay solution

MCU - Mitochondrial calcium uniporter

Mfn - Mitofusin

MJD - Machado-Joseph disease

MMP2 - Matrix metalloproteinase-2

mtDNA - Mitochondrial DNA

MTOC - Mitcrotubule organizing center

NaF - Sodium fluoride

NCoR1 - Nuclear receptor co-repressor

NEED8 - Neuronal precursor cell expressed developmentally downregulated 8

NES - Nuclear export signals

NIs - Nuclear inclusions

NLS - Nuclear localization signal

O_2 – Oxygen

$O_2^{\bullet -}$ - Superoxide anion radical

OCR - Oxygen consumption rate

OMM - Outer mitochondrial membrane

OPA1 - Optic atrophy 1

OXPHOS - Oxidative phosphorylation

PBS - Phosphate-buffered saline

PCAF - p300/CBP-associated factor

PD - Parkinson's disease

PE - Phosphatidylethanolamine

PGC-1α - Peroxisome proliferator-activated receptor γ coactivator-1

PINK1 - PTEN-induced putative kinase 1

PLIC1 - Protein linking IAP to the cytoskeleton

PMAIP1 - PUMA, p53 upregulated modulator of apoptosis

PolyQ - Polyglutamine

PVDF - Polyvinylidene fluoride

Q - Glutamine

RCR - Respiratory control ratio

RFU - Relative fluorescence units

Rh123 - Rhodamine 123

ROS - Reactive oxygen species

RPMI - Roswell Park Memorial Institute's

SBMA - Spinal and bulbar muscular atrophy

SCA - Spinocerebellar ataxia

SCA3 -Spinocerebellar ataxia type 3

SDS - Sodium dodecyl sulfate

SDS-PAGE - SDS-polyacrylamide gel electrophoresis

SOD2 - Superoxide dismutase 2

SQSTM1 - Sequestosome-1

TAF4 - TBP-associated factor 4

TBP - TATA binding protein

TBS-T - Tris buffered saline with 0.1% Tween-20

TCA - Trichloroacetic acid

TFAM - Mitochondrial transcription factor A

Ub - Ubiquitin

UIM - Ubiquitin interacting motif

UCP - Uncoupling protein

UPP - Ubiquitin proteassome pathway

VCP - Vasolin-containing protein

WT - Wild-type

Δp - Electrochemical proton motive force

$\Delta\psi_m$ - Mitochondrial membrane potential

List of Figures

List of Tables

Abstract

Machado-Joseph disease (MJD) is an autosomal dominant inherited neurodegenerative disease that affects 1-2 individuals per 100,000 people. It belongs to the group of polyglutamine (polyQ) expansion disorders caused an increase in the number of CAG repeats. In MJD the mutation occurs in the *MJD1/ATXN3* gene that encodes the protein ataxin-3 with an abnormal polyQ expansion at the C-terminal. Neuropathologically it is characterized by selective depigmentation of the *substantia nigra* and atrophy of the cerebellum, pons, and medulla oblongata.

Previous studies have proposed mitochondrial dysfunction as a mechanism of neurodegeneration in many diseases, including Huntington's disease (HD), another polyQ expansion disorder; however little is known about mitochondrial bioenergetics impairment in MJD. In the present study two different MJD models were used, namely 24 week-old CMVMJD135 (MJD135) transgenic mice expressing *ATXN3* with Q135 *versus* wild-type (WT) mice, and PC6-3 cell line expressing *ATXN3* either with Q28 (control) or Q108 (mutant), in order to characterize the changes in mitochondrial function and dynamics.

Firstly we analysed mitochondrial biogenesis by evaluating the levels of PGC-1α and TFAM. We observed a significant decrease in the levels of PGC-1α in Q108 cells, which was not accompanied by altered levels of TFAM in Q108. TFAM levels were also unchanged in mitochondria isolated from cerebellum and brainstem of MJD135, as compared to WT mice. When evaluating the oxygen consumption rate, mitochondria from both areas displayed decreased maximal respiration, however only cerebellar mitochondria exhibited decreased ATP production and proton leak. No differences were observed in the activity of mitochondrial complexes of both brain areas, but mitochondrial cytochrome c protein levels were significantly reduced in cerebellar mitochondria. Cerebellar mitochondria from MJD135 mice also exhibited decreased mitochondrial membrane potential associated with abnormal calcium handling. On the other hand, brainstem mitochondria exhibited decreased calcium uptake capacity, but no changes in membrane potential. Conversely, Q108 cells demonstrated decreased mitochondrial membrane potential, without major changes in mitochondrial calcium

accumulation. Despite the previous results mitochondrial production of hydrogen peroxide remained unaltered in both MJD135 brain areas.

When analyzing mitochondrial dynamics Q108 cells exhibited decreased levels of the fission proteins Drp1 and Fis1, whilst the levels of the fusion proteins Mfn2 and OPA1 were unchanged, suggesting more elongated mitochondria in mutant PC6-3 cells. To evaluate the possible occurrence of mitophagy in PC6-3 Q108 cells, the levels of PINK1, parkin, p62, LC3-II and the LC3-II/LC3-I ratio were also measured. We observed decreased levels of the cargo effector p62 and LC3-II, increased cytosolic levels of PINK1, as well as no changes in parkin or in autophagossome formation, indicating altered levels of macroautophagy and mitophagy-associated proteins tending towards autophagy activation.

Overall mitochondrial function and dynamics was show to be differentially compromised in both models tested, namely isolated mitochondria from MJD135 transgenic mice and PC6-3 Q108 cells.

Resumo

A doença de Machado-Joseph (MJD) é uma doença neurodegenerativa autossómica dominante que afeta cerca de 1 a 2 indivíduos em 100,000 habitantes. Pertence ao grupo das doenças de expansão poliglutaminica que são causadas pelo aumento do número de repetições CAG. Na MJD a mutação ocorre no gene *MJD1/ATXN3* que codifica a proteína ataxina-3 com uma expansão poliglutaminica aberrante no seu C-terminal. Neuropatologicamente é caracterizada por depigmentação seletiva da *substantia nigra* e pela atrofia do cerebelo, pons e medula oblongata.

Estudos anteriores propuseram a disfunção mitocondrial como um mecanismo de neurodegeneração em várias doenças, incluindo a doença de Huntington (HD), uma outra doença poliglutaminica; no entanto, muito pouco se sabe sobre o dano bioenergética mitocondrial na MJD. No presente estudo dois modelos diferentes de MJD foram utilizados, nomeadamente murganhos de 24 semanas de idade CMVMJD135 (MJD135) transgénicos que expressam ATXN3 com Q135 *versus* murganhos wild-type (WT), e uma linha celular PC6-3 que expressa ATXN3 ou com Q28 (controlo) ou com Q108 (mutante), de modo a caracterizar as alterações na função e dinâmica mitocondrial.

Em primeiro lugar, foi analisado a biogénese mitocondrial através da avaliação dos níveis de PGC-1α e TFAM. Foi possível observar uma diminuição significativa nos níveis de PGC-1α nas células Q108 que não foi acompanhada de alterações nos níveis de TFAM nas células Q108. Os níveis de TFAM mantiveram-se inalterados nas mitocôndrias isoladas do cerebelo e do tronco cerebral dos murganhos MJD135 quando comparadas com os murganhos WT. Quando se avaliou o consumo de oxigénio, as mitocôndrias de ambas as áreas demonstraram uma diminuição na respiração máxima, no entanto, apenas as mitocôndrias de cerebelo exibiram uma diminuição na produção de ATP e na fuga de protões. Não foram observadas diferenças nas atividades dos complexos mitocondriais, mas os níveis mitocondriais de citocromo c encontravam-se significativamente reduzidos nas mitocôndrias do cerebelo. As mitocôndrias do cerebelo de murganhos MJD135 também exibiram uma

diminuição no potencial da membrana mitocondrial associado com uma aberrante capacidade de captar cálcio. Pelo contrário, as mitocôndrias do tronco cerebral apresentaram um decréscimo na capacidade de reter cálcio, mas não apresentaram alterações no potencial da membrana mitocondrial. Reciprocamente, as células Q108 demonstraram diminuído potencial da membrana mitocondrial sem demonstrarem alterações na capacidade de acumularem cálcio. Apesar dos resultados anteriores, a produção mitocondrial de peróxido de hidrogénio manteve-se inalterada em ambas as áreas cerebrais dos murganhos MJD135.

Quando se realizou a análise da dinâmica mitocondrial, as células Q108 exibiram níveis diminuídos das proteínas de fissão Drp1 e Fis1, enquanto os níveis das proteínas de fusão Mfn2 e OPA1 se mantiveram inalterados, o que sugere que as mitocôndrias das células PC6-3 mutantes sejam mais alongadas. De modo a avaliar a ocorrência de mitofagia nas células PC6-3 Q108, os níveis de PINK1, parkin, p62, LC3-II e o rácio LC3-II/LC3-I também foram analisados. Foi possível observar a diminuição dos níveis de p62 e LC3-II, o aumento dos níveis citosólicos de PINK1 e, também, não se observaram diferenças em relação à parkin ou na formação de autofagossomas, o que indica níveis alterados de macroautofagia e de proteínas associadas com a mitofagia, indicando uma ativação da autofagia.

Em geral, a função e a dinâmica mitocondrial estavam comprometidas em ambos os modelos testados, nomeadamente, Nas mitocôndrias isoladas dos murganhos transgénicos MJD135 e nas células PC6-3 Q108.

Chapter 1

Introduction

1.1. Polyglutamine disorders

Polyglutamine (polyQ) expansion disorders are a group of nine hereditary neurodegenerative diseases that have as genetic cause an increase in the number of CAG repeats. Consequently, this increased CAG repeat is translated into an abnormally long tract of glutamines (Q) in the protein encoded by the respective mutated gene. The discovery of this mechanism known as the "triplet repeat" expansion occurred in 1991 in X-linked spinal bulbar muscular atrophy (SBMA) (Fu *et al.*, 1991; La Spada *et al.*, 1991)). Over the following years many diseases presenting an expansion of CAG repeats were also classified as polyQ disorders. Nowadays, this group is composed of Huntington's disease (HD, the most prevalent), spinal and bulbar muscular atrophy, also known as Kennedy's disease, dentatorubral-pallidoluysian atrophy (DRPLA) and spinocerebellar ataxias (SCA) type 1, 2, 3, 6, 7 and 17 (**Table 1**) (Zoghbi and Orr, 2000; Gatchel and Zoghbi, 2005; Shao and Diamond, 2007).

Although they are caused by a CAG expansion, the gene in which the mutation occurs is different for each disorder leading to the codification of different expanded proteins. Despite the fact that the affected proteins are physiologically and functionally different from each other, these diseases share some similarities amongst themselves. They are all late onset diseases, characterized by neurodegeneration and selective neuronal loss occurring in different brain regions thus leading to different clinical features. Apart from SBMA, all polyQs are autossomal dominant inherited diseases (Gatchel and Zoghbi, 2005). Also all polyQs present a dominant toxic effect as the disease can be caused by a single mutated allele. Previous studies claimed that the polyQ stretch confers toxic properties to the expanded protein; however whether it leads to a gain or loss of function of the respective protein varies (Gusella and MacDonald, 2000). Moreover, studies have demonstrated that there is an inverse correlation between the length of the CAG repeat and the age of disease onset, as the age of onset decreases with the increase in CAG expansion (Maciel *et al.*, 1995; Ranum *et al.*, 1995; Dürr *et al.*, 1996). When increased, the CAG repeats are extremely instable, as they tend to expand with paternal transmission and reduce when transmitted through maternal transmission. This instability results in longer polyQ stretches and earlier age of onset in the next generations.

One major hallmark of polyQ diseases is the formation of large intracellular macromolecular aggregates of the expanded proteins in the cytoplasm or nucleus of neurons being the latter denominated nuclear inclusions (NIs) (Zoghbi and Orr, 2000). Firstly they were considered to be responsible for inducing toxicity, however recent studies have refuted this hypothesis. In fact the relevance of these inclusions for the pathogenesis of polyQ disease is not well understood. The mechanisms underlying the toxicity of polyQ disorders have not been well established, as it appears that there is more than one associated mechanism. The most impactful mechanisms discovered so far have been: polyQ stretch-induced modifications, transcriptional deregulation, impaired axonal transport, mitochondrial dysfunction and apoptosis.

Table 1 - Features and characteristics of polyglutamine expansion disorders.

Disease	Gene/Locus	Normal	Expanded	Neuropathology
DRPLA	Atrophin-1 12p 12	3-35	49-88	Cerebellum, red nucleus, globus pallidus, subthalamic nucleus
HD	Huntingtin 4p 16.3	6-35	40-121	Striatum, cerebral cortex
SBMA	Androgen receptor Xq 11-12	9-36	38-62	Anterior horn cells in the brainstem and spinal cord
SCA1	ATXN1 6p 22-23	6-38	39-82	Cerebellum, red nucleus, pons, brainstem
SCA2	ATXN2 14q 23-24	14-31	32-77	Cerebellar Purkinje cells, fronto-temporal-lobes, brainstem
SCA3/MJD	ATXN3/MJD1 14q 24.3-31	12-42	52-84	Cerebellum, brainstem, spinal cord, basal ganglia
SCA6	CACNA1A 19p 13	4-19	20-30	Cerebellar Purkinje cells, dentate nucleus, inferior olive
SCA7	SCA7 3p 12-p 21.1	4-35	37-306	Cerebellum, macula, brainstem visual cortex
SCA 17	TATA Binding Protein (TBP) 6q 27	29-42	47-63	Cerebellum, cortex, caudate and putamen

(Adapted from: Ross, 1995; Paulson, 1999; Todd and Paulson, 2010; Zoghbi and Orr, 2000).

1.2. Machado-Joseph disease

Machado-Joseph disease (MJD) also known as spinocerebellar ataxia type 3 (SCA3), is an autosomal dominantly inherited neurodegenerative disease. It is the most common form of dominantly-inherited ataxia worldwide and the second most common polyQ expansion disorder (Schöls *et al.*, 2004; Bettencourt and Lima, 2011; Paulson, 2013). MJD is considered a rare disease as its prevalence varies around the world. It affects 1 or 2 individuals per 100,000 people in Portugal, however it is very predominant in the Azores islands as the highest prevalence, 1 in 239 individuals, occurs in Flores Island (Bettencourt *et al.*, 2008).

MJD was first described as a hereditary ataxia in an American-Portuguese family of Azorean descent, named Machado (Nakano *et al.*, 1972). Later it was also described in other Portuguese families, such as the Thomas and Joseph families, and along the years was known as "Nigro-spino-dentatal degeneration with nuclear opthalmoplegia", "Azorean disease of the nervous system" and "Autossomal dominant striatonigral degeneration" (Woods and Schaumburg, 1972; Rosenberg *et al.*, 1976; Romanul *et al.*, 1977). In initial studies MJD and SCA3 were thought to be two separate diseases, however, due to the overlapping symptoms found in different patients and the mapping of the associated genes to the same chromosomal locus they were eventually recognized as the same disease (Takiyama *et al*., 1993; Kawaguchi *et al*., 1994; Haberhausen *et al*., 1995). Presently, both terms, MJD and SCA3, are used.

MJD was first thought to be a disease of Portuguese descent which was spread throughout the world due to the Portuguese discoveries. Nowadays, MJD has been diagnosed in individuals from different backgrounds and are endowed with a heterogeneous epidemiology. It has a high prevalence in countries such as Brazil, Portugal, China, Japan, Germany and The Netherlands. It presents a lower prevalence in Canada, the United States, Australia and France, whilst in countries such as South Africa, India, Italy and the United Kingdom it is less common (Bettencourt and Lima, 2011).

MJD is a chronic and ultimately fatal disease with an average age of onset of 40 years and a life expectancy rate of around 20-30 years after diagnosis. Despite the ongoing research and knowledge about this disease there are still no effective

neuroprotective therapies and only symptomatic treatments are available (Bauer and Nukina, 2009).

1.2.1. Genetics

In MJD the mutation occurs in the *MJD1/ATXN3* gene, which is located on the 10th exon at the human chromosomal locus 14q32, that encodes the protein ATXN3. The CAG repeat-containing gene associated with this disease was first mapped in 1993, cloned the following year and denominated *MJD1* (Takiyama *et al.*, 1993; Kawaguchi *et al.*, 1994). Nowadays, the official name of the gene is *ATXN3* but both denominations, *MJD1* or *ATXN3*, can be found in the literature.

Healthy individuals have 12 to 42 CAG repeats within the *MJD1/ATXN3* gene, whereas in patients diagnosed with MJD the number of CAG repeats is expanded from 52 to 84. Individuals with CAG repeats between this interval do not necessarily express the phenotype, however, they exhibit a higher predisposition to develop the disease. The smallest repeat number found in a patient with MJD was 45, whereas the longest number detected in a healthy individual was 51 (Cummings and Zoghbi, 2000; Zoghbi and Orr, 2000; Maciel *et al.*, 2001; Riess *et al.*, 2008).

1.2.2. Pathology and clinical features

Machado-Joseph is a motor disease that mostly affects the central nervous system (CNS) and as the name implies, is mainly characterized by atrophy of the cerebellum and severe neurodegeneration and gliosis, however almost all brains regions are affected in this disease. Patients diagnosed with MJD exhibit depigmentation of the *substantia nigra*, atrophy of the pons, medulla oblongata, basal ganglia, midbrain, cranial nerves and optical nerves. Magnetic resonance imaging demonstrated that MJD patients also exhibit enlargement of the fourth ventricule and reduction of the caudate and putamen (Rüb *et al.*, 2002; Klockgether *et al.*, 1998).

MJD has a wide variety of symptoms depending on many factors, more specifically the sub-type of the disease. The disease can be categorised in 5 different

sub-types that vary in the age of onset, progression as well as clinical features (**Table 2**). One of the first and most common symptoms of MJD is progressive ataxia, which affects balance, gait and speech. Overall, some common clinical features include weakness, spasticity, postural instability, dysarthria, vision problems, dystonia and frequent urination (Coutinho and Andrade, 1978; Lima and Coutinho, 1980; Rüb *et al.*, 2002; Riess *et al.*, 2008). Symptoms such as restless leg syndrome and weight loss are commonly found in patients with different subtypes of the disease. Although not so common, mild cognitive and behavioural problems are also associated with more than one subtype (Kawai *et al.*, 2004; Paulson, 2007; Riess *et al.*, 2008).

MJD can be divided into type 1 ("type Joseph"), type 2 ("type Thomas"), type 3 ("type Machado") and type 4. A type 5 was also considered when a rare case of two siblings diagnosed with spastic paraplegia but showing no signs of cerebellar ataxia was observed (Sakai and Kawakami, 1996; Bettencourt and Lima, 2011).

Table 2 - Prevalence, age of onset, progression and clinical features of the different subtypes of MJD.

Subtype	Prevalence	Age of onset	Progression	Clinical Features
Type I	13%	Before 20 years old	Fast	Ataxia Pyramidal features: spasticity and rigidity Extrapyramidal features: dystonia and bradykinesia
Type II	Most common (57%)	Between 20-50 years old	Intermediate	Ataxia Progressive external opthalmoplegia Pyramidal features
Type III	30%	Between 40-75 years old	Slow	Muscle atrophy Motor neuropathy Vision problems
Type IV	Most Rare	-	-	Parkinsonian symptoms
Type V	Proposed more recently rare cases	-	-	Resembles spastic paraplegia

(Adapted from: Ross, 1995; Paulson, 1999; Todd and Paulson, 2010; Zoghbi and Orr, 2000).

1.3. Ataxin-3

Ataxin-3 (ATXN3) is the smallest existing polyQ diseased protein having a molecular weight of approximately 42 kDa. Besides being present in humans, ATXN3 can also be found in eukaryotic organisms, nematodes, fungi, plants and animals. ATXN3 is expressed throughout the entire human body and in all brain regions, even those not affected by the disease. However, studies have demonstrated that, in certain brain areas, it is not expressed in all types of neurons (Paulson *et al.*, 1997a). ATXN3 is a mainly cytosolic protein, especially in neurons, but it is capable of translocating towards the nucleus, where it associates with the nuclear matrix, (Paulson *et al.*, 1997; Schmidt *et al.*, 1998) Moreover, it can also be found in mitochondria, since a previous study demonstrated the presence of two small ATXN3 isoforms (29 and 49 kDa) in mitochondrial-enriched fractions of Hela cells (Trottier *et al.*, 1998).

The high mobility of ATXN3 between the nucleus and the cytosol is mediated by a nuclear localization signal (NLS) and around 6 nuclear export signals (NES) (Antony *et al.*, 2009; Macedo-Ribeiro *et al.*, 2009; Reina *et al.*, 2009; Tait *et al.*, 1998). The localization of ATXN3 in the nucleus is also mediated by heat shock, oxidative stress and phosphorylation events, since it is targeted by the serine-threonine casein kinase 2 (CK2) and glycogen synthase kinase 3β (GSK 3β). The phosphorylation of ATXN3 is also required for its stability (Mueller *et al.*, 2009; Fei *et al.*, 2007).

ATXN3 belongs to the family of cysteine proteases and is considered a deubiquitylase (DUB) protein. It contains a catalytic Josephin domain in its N-terminal, two or three ubiquitin-interacting motifs (UIM), depending on the spliced isoform, in its C-terminal, and a variable polyQ tract (Masino *et al.*, 2011; Burnett *et al.*, 2003; Berke *et al.*, 2005; Gales *et al.*, 2005). The Josephin domain has ubiquitin hydrolase activity and is composed of a globular catalytic domain and a helical hairpin. It also contains the aminoacids cysteine (C14), histidine (H119), asparagine (N134) and glutamine (Q9), which are believed to be responsible for this catalytic activity c; Nicastro *et al.*, 2005). The UIMs are α-helical structures that give ATXN3 the ability to bind ubiquitin (Ub) and K48-linked polyUb chains (Song *et al.*, 2010). ATXN3 normally binds to Ub chains with more than four Ubs (Burnett *et al.*, 2003; Mao *et al*., 2005).

Due to its DUB activity, ATXN3 is also capable of catalyzing the cleavage of ubiquitin (Ub) and is itself regulated by ubiquitination (Wilkinson, 1997; Burnett *et al.*, 2003).

ATXN3 appears to have a role in protein degradation due to its DUB activity and ability to interact with the ubiquitin-proteassome pathway (UPP) and several chaperones (Chai *et al.*, 1999). Vasolin-containing protein (VCP/p97) and hHR23A are capable of directly interacting with human ATXN3 (Laço *et al.*, 2012). VCP/97 is a ATPase that regulates the degradation of misfolded proteins through endoplasmatic reticulum-associated degradation (ERAD) whilst hHR23A is the human homolog of the RAD23 yeast protein that is involved in directing ubiquitaned proteins to the proteassome and repairing DNA (Wang *et al.*, 2000; Zhong and Pittman, 2006; Dantuma *et al.*, 2009). Ataxin-3 also interacts with the Ub-like protein neuronal precursor cell expressed developmentally downregulated 8 (NEDD8) and interacts with the mitophagy associated protein parkin, inducing its deubiquitination (Ferro *et al.*, 2007; Durcan *et al.*, 2011).

The role of ATXN3 in transcriptional regulation has also been highlighted as it can regulate the expression of several genes, interact with various transcriptional regulators (both repressors and activators) and bind to DNA through a leucine zipper motif (Li *et al.*, 2002; Evert *et al.*, 2006). ATXN3 interacts with histone deacetylase (HDAC) 3 and 4, forkhead box O (FOXO) transcription factor FOXO4, p330, p300/CBP-associated factor (PCAF), nuclear receptor co-repressor (NCoR1), cAMP response element-binding protein (CBP) and TATA box-binding protein (TBP)-associated factor 4 (TAF4) (McCampbell *et al.*, 2000; Shimohata *et al.*, 2000; Chai *et al.*, 2002; Li *et al.*, 2002; Burnett and Pittman, 2005; Evert *et al.*, 2006; Araujo *et al.*, 2011). Moreover, studies have demonstrated that it impairs the transcription of matrix metalloproteinase-2 (MMP2) (Mueller *et al.*, 2009).

Furthermore, ATAXN3 appears to be involved in the organization of the cytoskeleton, myogenesis and aggresome formation. ATXN3 was found to be associated with the microtubule organizing center (MTOC), tubulin, dynein, microtubule associated protein 2 (MAP2) and protein linking IAP to the cytoskeleton (PLIC1) (Burnett and Pittman, 2005; Mazzucchelli *et al.*, 2009; Mueller *et al.*, 2009; Heir *et al.*, 2006). Studies have demonstrated that silencing ATXN3 leads to severe changes in cellular cytoskeleton. It promotes an immature cytoskeleton, decreased cell

adhesion and disorganization of microfilaments, microtubules and intermediate filaments (Costa *et al.*, 2010; Rodrigues *et al.*, 2010).

The discovery of ATXN3's DUB activity suggests that it is responsible for activating and stabilizing several proteins involved in a wide variety of cellular processes, however, the exact function of this protein still remains elusive. Furthermore, the importance of this protein for normal cell survival has also not yet been well established.

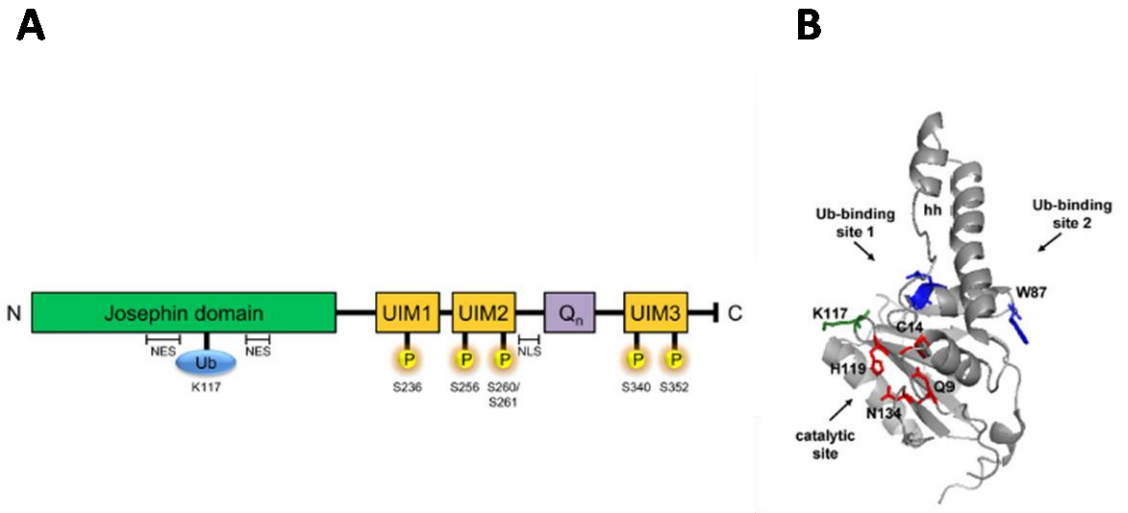

Figure 1.1 - Domain architecture, structure and post-translation modifications of ATXN3.
(**A**) Ataxin-3 is composed of a globular N-terminal catalytic Josephin domain, followed by a flexible C-terminal containing two or three ubiquitin-binding motifs (UIMs) and a variable polyQ stretch (Q_n). The UIMs contain five serine residues – S236, S256, S260/S261, S340, S352 – which are phosphorylation sites. Two nuclear export signals (NES) in the Josephin domain and one nuclear localization signal near the second UIM are depicted. ATXN3 is monoubiquitinated primarily at residue K117 in the Josephin domain. (**B**) Three-dimensional representation of the Josephin domain composed by a catalytic domain and a helical hairpin (hh), highlighting the major ubiquitinated site – K117 – (green), the residues of Ub-binding sites (blue) and the catalytic residues (red). The aminoacids C14, H119, N134 and Q9 are located in a catalytic pocket. (Adapted from: Matos *et al.*, 2011; Costa and Paulson, 2012).

1.3.1 Mutant Ataxin-3

As in all polyQ disorders increased CAG repeat encodes for a polyQ stretch, leading to the codification of an abnormal/misfolded protein with modified biochemical and biophysical properties. Expanded ATXN3 is still capable of "travelling" between the nucleus and the cytoplasm, however it tends to aggregate in the nuclear compartment. In fact, many studies suggest that the main site of toxicity in MJD is the nucleus and that this nuclear aggregation exacerbates the phenotype of the disease (Chai *et al.*, 2002; Perez *et al.*, 1998; Bichelmeier *et al.*, 2007). Aggregation of ATXN3 appears to undergo a twostep process: first is the formation of soluble sodium dodecyl sulfate (SDS) fibrils and the second is the generation of insoluble SDS aggregates (Ellisdon *et al.*, 2006). ATXN3 aggregates appear to be enriched in β-sheet fibrillar structures, contributing to irreversible aggregation (Bevivino and Loll, 2001; Natalello *et al.*, 2011).

Previous studies have demonstrated that the molecular phenotype of MJD can be rescued in a transgenic mouse model of MJD expressing the full human disease gene with depletion of the mutant ATXN3 allele in the brain (Rodríguez-Lebrón *et al.*, 2013). This indicates that the presence of expanded ATXN3 has a central role in the pathogenesis of MJD.

1.4. Pathogenic mechanisms in MJD

The true extent of the mechanisms by which ATXN3 causes cellular toxicity in MJD have not yet been fully studied and understood. Along the years many novel candidates have emerged being the most prominent: proteolytic cleavage and formation of toxic ataxin-3 fragments, transcriptional deregulation, impaired protein degradation and few evidences of mitochondrial dysfunction. RNA toxicity and axonal transport have also been proposed as pathogenic mechanisms.

1.4.1 Formation of toxic ataxin-3 fragments

Many studies have supported the "toxic fragment hypothesis", which claims that selective neuronal loss is caused by the cleavage of a toxic mutant ATXN3 fragment. This hypothesis arouse from the discovery that the C-terminal, containing the polyQ expansion, of mutant ATXN3 is more toxic than the rest of the protein and that it could alter the conformation of wild-type ATXN3 (Ikeda *et al.*, 1996; Paulson *et al.*, 1997; Haacke *et al.*, 2006). After cleavage, the toxic fragment supposedly aggregates and recruits other proteins in order to form nuclear inclusions (Li *et al.*, 2002; Donaldson *et al.*, 2003; Paulson, 2007).

1.4.2. Transcriptional deregulation

Due to the interaction of ATXN3 with several transcriptional regulators and its ability to bind to DNA, transcription deregulation in MJD has been widely investigated. Studies have shown that mutant ATXN3 promotes the downregulation of a wide variety of genes, such as genes involved in heat shock proteins (Hsp) responses, MAP kinase pathways, glutamatergic neurotransmission, as well as genes that regulate cell survival (Chou *et al.*, 2008). On the other hand, the expression of inflammatory genes and proteins such as interleukin, MMP2 and β-protein was increased. Concordantly, inflammatory markers were observed in the brains of MJD patients (Evert *et al.*, 2001, 2003).

Another study demonstrated that mutant ATXN3 is capable of upregulating mRNA expression of pro-apoptotic genes such as Bcl2-associated X protein (Bax) and PUMA, p53 upregulated modulator of apoptosis (PMAIP1). This eventually triggers mitochondrial apoptotic pathways and leads to neuronal death both *in vivo* and *in vitro* due to increased activity and phosphorylation of p53 (Chou *et al.*, 2006; Chou *et al.*, 2011). Other proteins involved in neuronal death such as cyclin D1 and CDK5-p39 also presented an increased expression in mutant cell models (Chou *et al.*, 2008).

1.4.3. Impaired protein degradation

Since wild-type ATXN3 is a known DUB capable of binding and cleaving Ub and interacting with the UPP, alterations in protein degradation have been suggested to play a central role in MJD. Some authors claim that ATXN3 maintains its DUB activity when mutated, however, in a cell model of MJD a decrease in the amount of deubiquitinated proteins was observed (Winborn *et al.*, 2008).

This hypothesis was highlighted when studies demonstrated that the polyQ tract enhances the interaction between ATXN3 and VCP/97 and that VCP/97 was co-localized with the aggregates (Boeddrich *et al.*, 2006). Moreover, both autophagy and ERAD appear to be impaired in MJD (Nascimento-Ferreira *et al.*, 2011). In MJD brains the presence of aggregates containing autophagy-associated proteins such as beclin-1, were observed. Furthermore, when a therapy that stimulated autophagy was used in a transgenic mice model of MJD a significant amelioration of the phenotype, along with increased levels of beclin-1 and LC3-II, was observed (Silva-Fernandes *et al.*, 2014).

1.4.4. Mitochondrial dysfunction

Mitochondrial dysfunction has been correlated with the pathogenic mechanisms of several neurodegenerative disorders including MJD; in fact, some studies have demonstrated the association between impaired mitochondrial dynamics and function in this disease. In a study using a stable PC12 cell line expressing either normal or expanded human ATXN3, mutant cells not only exhibited neuronal cell death, but also

decreased mitochondrial membrane potential and potassium channel dysfunction. This indicated that the electrophysiological properties were compromised in cells expressing expanded ATXN3 (Jeub *et al.*, 2006). Another studied demonstrated that when SCA3-YAC-84Q mice were treated with dantrolene, a stabilizer of intracellular Ca^{2+} signaling, there was an improvement in MJD symptoms, accompanied by a decrease in neuronal cell death, thus indicating that intracellular Ca^{2+} is compromised in MJD (Chen *et al.*, 2008). In accordance are the findings showing that genes involved in calcium signalling and glutamatergic neurotransmission are downregulated in neurons obtained from the cerebellum of transgenic mice expressing ATXN3 Q79 (Chou *et al.*, 2010).

Moreover, studies have demonstrated that mutant ATXN3 reduces the levels of antioxidant enzymes and leads to increased mitochondrial DNA (mtDNA) damage (Yu *et al.*, 2009). A recent study also demonstrated that mutant ATXN3 reduces the transcription of superoxide dismutase (SOD2), thus making cells more vulnerable to oxidative stress (Araujo *et al.*, 2011). Decreased copy numbers of mtDNA were also observed in the pontine nuclei of a transgenic mice model of MJD and in mutant cells and MJD patient samples (Yu *et al.*, 2009; Kazachkova *et al.*, 2013).

Previous studies have also demonstrated a small decrease in the activity of mitochondrial complex II in differentiated PC6-3 cells expressing ataxin-3 with 108 glutamines, suggesting that the mitochondrial respiratory chain might be compromised in MJD (Laço *et al.*, 2012). Despite these findings, the impact of ATXN3 on other vital mitochondrial processes has yet to be clarified.

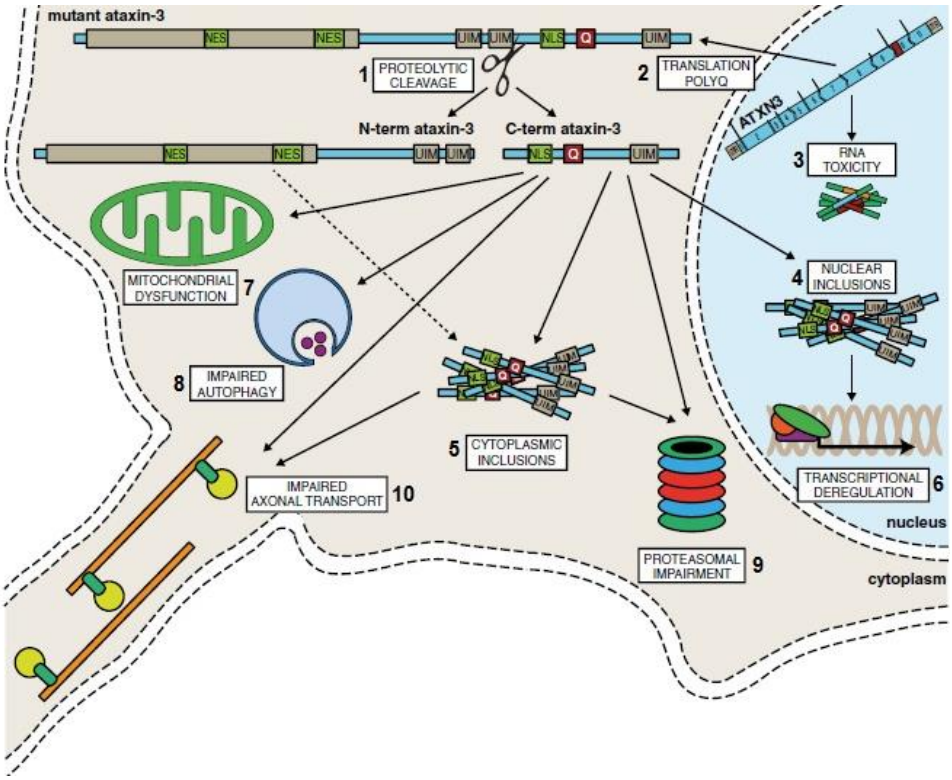

Figure 1.2 - Molecular pathways of neurodegeneration in Machado-Joseph disease.
Several mechanisms underlying the pathogenesis of MJD have been proposed such as: **1**) proteolytic cleavage, **2)** translation of polyQ, **3**) RNA toxicity, **4,5**) formation of inclusions, **6**) transcriptional deregulation, **7**) mitochondrial dysfunction, **8**) impaired autophagy, **9**) proteassome impairment and **10**) impaired axonal transport (Adapted from: Evers *et al*., 2014).

1.6. Objectives

Over the years, mitochondrial dysfunction has been considered a pathogenic mechanism of several neurodegenerative disorders and, as such, many promising therapeutics strategies targeting mitochondrial processes have proposed. Despite these findings the toxic mechanisms behind the pathogenesis of disease still remain elusive and the role of mitochondrial dysfunction in MJD pathogenesis has not yet been fully studied.

Thus, in the present study we aimed to characterize the alterations in mitochondrial function and dynamics in two different MJD models: mitochondria isolated from 24 week-old CMVMJD135 transgenic mice and PC6-3 cell line expressing *ATXN3* with Q135 and Q108, respectively, *versus* each control. In order to characterize mitochondrial dynamics we evaluated fission/fusion balance and mitophagy, whereas to characterize mitochondrial function we analysed mitochondrial biogenesis, mitochondrial respiration, electron flow in the respiratory chain, mitochondrial membrane potential, calcium handling and mitochondrial hydrogen peroxide production.

Overall, this study aims to shed some light on whether mitochondrial dysfunction plays an impactful role in MJD. By understanding the basic mechanisms underlying the pathogenesis of this disease more effective therapeutic strategies could be envisioned in the future.

Chapter 2

Methods

2.1. Materials

Roswell Park Memorial Institute's medium (RPMI) hygromycin, doxicyclyne hyclate, carbonyl cyanide 4-(trifluoromethoxy) phenylhydrazone (FCCP), adenosine triphosphate (ATP), adenosine diphosphate (ADP), oligomycin A, protease inhibitor cocktail, peroxidase from horseradish, antimycin A, rotenone, pyruvate, Tetramethyl-p-phenylenediamine (TMPD) and mostly all other reagents were acquired from Sigma-Aldrich Co. (St. Louis, MO, USA). Blasticidin and Lipofectamine® 3000 were obtained from Invitrogen (Paisley, UK). Fetal bovine serum (FBS) and horse serum (HS) and OPTIMEM medium were purchased from GIBCO (Paisley, UK). Hoechst 33342 nucleic acid stain was purchased from Invitrogen/Molecular probes (Life Technologies Corporation, Carlsbad, CA, USA). Bovine serum albumin (BSA) was acquired from Santa Cruz Biotechnology (Santa Cruz Biotechnology, Inc., TX, USA). Biorad Protein Assay and Polyvinylidene fluoride (PVDF) membrane were obtained from BioRad Laboratories, Inc. (Munich, Germany). ECF substrate was purchased from GE Healthcare (GE Healthcare Bio-Sciences, PA, USA). XF24 cell culture microplates were purchased from Seahorse Bioscience (Billerica, MA, USA). Fura-2/AM, Rhodamine 123 (Rh123) and Amplex®Red were obtained from Molecular Probes/Invitrogen (Eugene, OR, USA). The plasmid pDsRed2-Mito (MitoDsRed; ref: 632421) used for transfection was obtained from Clontech (CA, USA). The primary and secondary antibodies used for western blotting and immunocytochemistry are presented in **Table 1** and **Table 2**, respectively.

Table 3 - Primary antibodies.

Primary Antibodies	Host Species	Dilution	Brand/Reference
Actin β	Mouse	1:50000 (WB)	Sigma A5316 (Sigma St. Louis, MO, USA)
Ataxin-3	Mouse	1-1000 (WB)	Chemicon MAB5360 (Merck Millipore, Darmstadt, Germany)
Cytochrome c	Mouse	1:500 (WB)	BD Biosciences Pharmingen (San Diego, CA, USA)
Complex II (70 kDa subunit)	Mouse	1:10000 (WB)	Molecular Probes A11142 (Molecular Probes – Invitrogen (Eugene, OR, USA)
Drp1	Mouse	1:500 (WB)	BD biosciences 611112 (BD Biosciences, Franklin Lakes, NJ, USA)
Fis 1 (TTC11)	Rabbit	1:1000 (WB)	Novus NB100-56646 (Novus Biologicals, LLC, CO, USA)
Hsp60	Mouse	1:300 (ICC)	Chemicon (Hampshire, UK)
LC3 A/B	Rabbit	1:1000 (WB)	Cell Signaling #12741 (Cell Signaling, Danvers, MA, USA)
Mfn2	Rabbit	1:1000 (WB)	Sigma M6319 (Sigma, St. Louis, MO, USA)
OPA1	Mouse	1:500 (WB)	BD Biosciences 612606 (BD Biosciences, Franklin Lakes, NJ, USA)
p62 (SQSTM1)	Rabbit	1:500 (WB)	BIOMWA-AP2138B (Biomol GmbH, Hamburg)
Parkin	Rabbit	1:1000 (WB)	Abcam ab15954 (Abcam, Cambridge, UK)
Phospho-Parkin (S65)	Rabbit	1:500 (WB)	Abcam ab154995 (Abcam, Cambridge, UK)
PGC 1-α (K15)	Goat	1:300 (WB)	sc-5816 (Santa Cruz Biotechnology, Inc., TX, USA)
PINK1	Rabbit	1:500 (WB)	Abcam ab23707 (Abcam, Cambridge, UK)
Polyglutamine (IC2)	Mouse	1:1000 (WB)	MAB 1574 (Merck Millipore, Darmstadt, Germany)
TFAM	Rabbit	1:500 (WB)	Abcam ab131607 (Abcam, Cambridge, UK)

Table represents the primary antibodies used, the species where they were produced, the dilution used and the supplier.

Table 4 - Secondary antibodies.

Secondary Antibodies	Host Species	Dilution	Brand/Reference
Alexa Fluor-594 goat anti-mouse	Goat	1:300	#A11005 (Molecular Probes – Invitrogen, Eugene, OR, USA)
Anti-goat (H+L) Alkaline Phosphatase Conjugated	Donkey	1:20 000	sc-2022 (Santa Cruz Biotechnology, Inc., TX, USA)
Anti-mouse (H+L) Alkaline Phosphatase Conjugated	Goat	1:20 000	Thermo Scientific Pierce #31320 (Pierce Thermo Fisher Scientific, Rockford, IL, USA)
Anti-rabbit (H+L) Alkaline Phosphatase Conjugated	Goat	1:20 000	Thermo Scientific Pierce #31340 (Pierce Thermo Fisher Scientific, Rockford, IL, USA)

Table represents the secondary antibodies used, the species where they were produced, the dilution used and the supplier.

2.2. Cell culture

PC6-3 cell lines expressing wild-type (Q28) or expanded (Q108) human ataxin-3 were obtained from Dr. Henry L. Paulson, Department of Neurology, University of Michigan, USA. PC6-3 cell line is a subline of the immortalized PC12 cell line, which is obtained from rat adrenal gland pheochromocytoma (Pittman *et al.*, 1993). Cells were maintained in RPMI medium supplemented with 10% (v/v) inactivated HS, 5% (v/v) inactivated FBS, 1% (v/v) streptomycin/penicillin (100 Units/mL Penicillin + 100 μg/mL Streptomycin), 100 μg/mL hygromycin and 2.2 μg/mL blasticidin. The expression of ATXN3 was regulated through the addition of 1 μg/mL doxycycline to the medium, for 48 hours before experiments. Cells were kept in uncoated T75 flasks, in upright position, using an incubator chamber containing in a 95% air and 5% CO_2 humidified atmosphere at 37°C. Cells were plated at a density of $6x10^4$ cells/mL on 16-mm-diameter glass coverslips coated with Poly-D-lysine until desired confluence was achieved, for immunocytochemistry.

2.3. Transfection

PC6-3 cells were transiently transfected with MitoDsRed plasmid DNA using Lipofectamine® 3000, 24 hours previous to their analysis, according to the manufactures' protocol. The cells were incubated in OPTIMEN medium (containing 28.5 mM $NaHCO_3$) for 4 hours after transfection and then the medium was replaced with RPMI medium supplemented with 1 μg/mL doxycycline.

2.4. Animals

CMVMJD135 (MJD135) and wild-type (WT) 24 week-old male mice, C57B1/6 background, were kindly gifted from Dr. Patrícia Maciel, Life and Health Sciences Research Institute (ICVS), School of Health Sciences, University of Minho, Braga, Portugal. The MJD135 mouse colony was previously described by Silva-Fernandes et al. (2014) and expresses the ATXN3a cDNA variant carrying approximately 135 CAG repeats into the pCMV vector. Throughout the experiments, mice were housed at the Center for Neuroscience and Cell Biology (CNC), University of Coimbra, Coimbra, Portugal, under conditions of controlled temperature (22-23ºC) and under a 12 h light/12 h dark cycle. Food and water were available *ad libitum*. Animal maintenance and procedures were performed in accordance with the guidelines of the Institutional Animal Care and Use of Committee and the European Community directive. Health monitoring was performed according to FELASA guidelines. The animals were sacrificed by decapitation as described in section 2.4 and the brain was collected and weighed (Fig. **2.1**). Next the cerebellum and brainstem were dissected out and weighted too. In concordance with the previous characterization of this mice model (Silva-Fernandes *et al.*, 2014) and with studies performed with MJD patients showing weight loss and decreased brain weight (Rüb *et al.*, 2008; Horimoto *et al.*, 2011). MJD135 mice, used in the present study, also exhibited lower body weight (Fig. **2.1 A**) and brain weight (Fig. **2.1 B**) when compared to WT mice. Although there were no significant differences in cerebellum weight a significant decrease in the brainstem weight of MJD135 was observed when compared with WT mice (Fig. **2.1 C**).

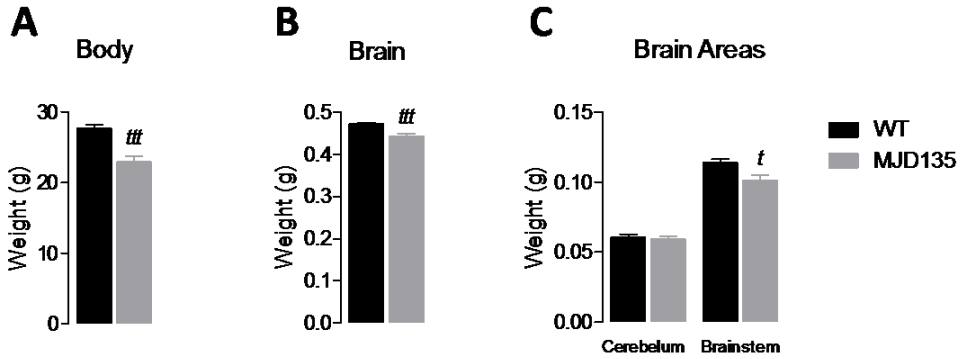

Figure 2.1 - Decreased body, total brain and brainstem weight in MJD135 mice.
Body (**A**), total brain (**B**), cerebellum and brainstem weight (**C**) were determined in 24-week-old MJD135 and WT mice. After sacrifice, brains were removed from the skull and cerebellum and brainstem dissected out from the brain. Data are the mean ± SEM of 8-9 different mice from each genotype. Statistical analysis was performed by Student's *t*-test: $^{t}p<0.05$ and $^{ttt}p<0.001$, compared to WT mice.

2.5. Mitochondria Isolation

Mice were sacrificed by decapitation (EU guideline 86/609/EEC) and the brain was immediately removed from the skull. The cerebellum and brainstem were further dissected out and immediately subjected to mitochondria isolation using discontinuous Percoll density gradient centrifugation, according to (Wang *et al.*, 2011), with some minor modifications. Briefly cerebellum and brainstem were homogenized in ice-cold isolation buffer (225 mM manitol, 75 mM sucrose, 5 mM HEPES-KOH, 1 mM EGTA – pH 7.2). The homogenized tissue was centrifuged at 1100x*g* at 4°C for 2 min. The supernatant was mixed with freshly made 80% Percoll prepared in ice-cold dilution buffer (1 mM sucrose, 50 mM HEPES and 10 mM EGTA – pH 7.0) and carefully layered on top of freshly made 10% Percoll (80% Percoll diluted in isolation buffer) and centrifuged at 18500x*g* at 4°C for 10 min. The pellet was washed once with washing buffer (250 mM sucrose, 5 mM HEPES-KOH and 0.1 mM EGTA – pH 7.2) and further centrifuged at 10000x*g* at 4°C for 5 min. The final pellet containing isolated mitochondria was resuspended in washing buffer and subjected to protein quantification by the BioRad protein assay. Mitochondrial fractions were immediately used for measurement of oxygen (O_2) consumption, mitochondrial membrane potential, calcium (Ca^{2+}) uptake and hydrogen peroxide (H_20_2) production or kept at -80°C for further use in western blotting.

2.6. Sample Preparation and Western Blotting

2.6.1. Total fractions

PC6-3 cells were centrifuged at 800x*g* for 5 min at 4°C, washed in ice-cold phosphate-buffered saline (PBS) solution (137 mM NaCl, 2.7 mM KCl, 1.4 mM K_2HPO_4, and 4.3 mM KH_2PO_4 – pH 7.4.) and centrifuged again. The remaining pellet was resuspended in 50 μL of ice-cold RIPA buffer (50 mM TRIS-HCl, 5 mM EGTA, 150 mM NaCl, 0.5% DOC, 0.1% SDS and 1% Triton X-100 – pH 7.4), supplemented with 1 mM sodium ortovanadate, 1 mM phenylmethylsulfonyl fluoride (PMSF), 180 nM okadaic acid, 1 mM dithiothreitol (DTT), 1 μg/mL protease inhibitor cocktail (chymostation, pepstatin A, leupeptin and atipain) and 50 mM sodium fluoride (NaF). The homogenates were sequentially frozen and thawed in liquid nitrogen three times and centrifuged at 20,800x*g* at 4°C for 10 min. The resulting supernatant were collected and stored for later use.

2.6.2. Mitochondrial and cytosolic-enriched fractions

Cells were centrifuged at 800x*g* at 4°C for 5 min, washed in ice-cold PBS and centrifuged again. The remaining pellet was resuspended in 500 μL of ice-cold sucrose buffer (250 mM Sucrose, 20 mM HEPES, 10 mM KCl, 1.5 mM $MgCl_2$, 1 mM EDTA, 1 mM EGTA – pH 7.4), supplemented as described in section 2.5.1. Then they were homogenized with 40 strokes using a Potter-Elvejhem 377 homogenizer with a Teflon pestle at 280 rpm and then centrifuged at 1,300x*g* at 4°C for 12 min to pellet the nuclei and cell debris. The obtained supernatant was centrifuged again at 11,900x*g* at 4°C for 20 min. The remaining pellet containing the mitochondrial-enriched fraction was resuspended in sucrose buffer. Supernatant (cytosolic fraction) was further subjected to protein precipitation by using 15% trichloroacetic acid (TCA) and the extracts were then centrifuged at 16,300x*g* at 4°C for 10 min. The cytosolic-enriched pellet was resuspended in sucrose buffer and pH adjusted to 7.0 with 10 M KOH.

2.6.3 Preparation of mitochondrial extracts from isolated mitochondria

Freshly isolated mitochondria from the cerebellum and brainstem as described above were resuspended in supplemented ice-cold RIPA buffer (1:1). Each sample was then subjected to sonication three times (5-10 seconds/pulse) and centrifuged for 10 min at 20,800x*g* at 4°C. Supernatant containing soluble mitochondrial proteins was collected and kept for further analysis.

2.6.4. Western Blotting

Equivalent amounts of protein were denatured with denaturing buffer (50 mM Tris-HCl pH 6.8, 5% glycerol, 2% SDS, 600 mM DTT and 0.01% bromophenol blue), at 95°C for 5 min. Protein separation was performed by electrophoresis on 7.5-15% sodium dodecyl polyacrylamide gel electrophoresis (SDS-PAGE) gels and electroblotted onto PVDF membranes. The membranes were blocked for 1 hour at room temperature in 5% (w/v) BSA in Tris buffered saline with 0.1% Tween-20 (TBS-T), followed by overnight incubation with primary antibodies (**Table 1**) at 4°C. Membranes were washed with TBS-T 3 times for 15 min and then incubated with the secondary antibodies (**Table 2**) for 1 hour at room temperature. All antibodies were prepared in 5% (w/v) BSA in TBS-T. Immunoreactive bands were visualized after incubation with ECF substrate using ChemiDoc Touch Imaging System (Bio-Rad). Bands were quantified using the Image Lab software (Bio-Rad).

2.7. Immunocytochemistry

Cells were washed with warm PBS, at 37°C, fixed with 4% paraformaldehyde for 20 minutes and washed again with PBS 4 times, at 37°C. Then cells were permeabilized with 0.1% Triton X-100 for 2 minutes and washed again 3 times before being blocked with 3% (w/v) BSA for 1 hour at room temperature. Cells were incubated with the primary antibodies (**Table 1**) overnight at 4°C, washed and then incubated with the secondary antibodies (**Table 2**) at room temperature for 1 hour. All antibodies were prepared in 3% (w/v) BSA in PBS. At last, cells were incubated for 20 minutes with

Hoechst 33342 (4 μg/mL) and the coverslips were mounted using Mowiol 40-88 (Sigma Chemical and Co., St. Louis, MO, USA). Confocal images were obtained using a Plan-Apochromat/1.4NA 63x lens on an Axio Observer.Z1 confocal microscope (Zeiss Microscopy, Germany) with Zeiss LSM 710 software.

2.8. Seahorse XF24 Analysis

Cell culture XF24 microplates were coated with polyethylenimine (PEI, 1:15000 dilution prepared from a 50% solution, Sigma-Aldrich, St. Louis), overnight at room temperature, in the dark. The XF24 extracellular flux assay plate kit, containing the sensor cartridge was allowed to hydrate overnight at 37°C. In the day of the experiments, PEI was washed out and the wells washed 1 time with water and let to dry at room temperature. Then, 5 μg of fresh mitochondria, isolated from the cerebellum and brainstem of MJD135 *versus* WT mice, resuspended in ice-cold mitochondrial assay solution (MAS: 70 mM sucrose, 220 mM mannitol, 10 mM KH_2PO_4, 5 mM $MgCl_2$, 2 mM HEPES, 1 mM EGTA and 0.2% (w/v) fatty acid-free BSA) was added to each well and further centrifuged for 20 min, at 4,000x*g* at 4°C. Then, the multiwell plate was allowed to incubate for 8 min, at 37°C in a non-$C0_2$ incubator. Mitochondria respiration was assessed in coupled conditions by sequential addition of 4 mM ADP, 2.5 μg/ml oligomycin (Oligo), 4 μM FCCP and 4 μM antimycin A (AntA), in MAS medium containing 10 mM succinate (Complex II substrate) and 2 μM rotenone (Complex I inhibitor). In a second protocol, the activity of mitochondrial complexes was assessed by sequential addition of 2 μM rotenone (Rot), 10 mM succinate (Suc), 4 μM antimycin A and 10 mM/100 μM Ascorbate/TMPD (Asc/TMPD), in medium containing 10 mM pyruvate, 2 mM malate (mitochondrial substrates) and 4 μM FCCP (mitochondrial uncoupler) as previously described (Rogers *et al.*, 2011). Oxygen consumption rate (OCR) was measured in three consecutive timepoints before and after the injection of each drug using Seahorse XF24 flux analyser (Seahorse Bioscience, Billerica, MA, USA).

2.9. Measurement of total levels of adenine nucleotides

Cerebellum or brainstem tissues were subjected to acidic extraction using 0.6 M perchloric acid supplemented with 25 mM EDTA-Na^+. Extracts were then centrifuged at 20,800×*g* for 2 min at 4 °C to remove cell debris; the resulting pellet solubilized in 1 M NaOH and further analysed for protein content by the Bio-Rad Protein assay. After neutralization with 3 M KOH/1.5 M Tris, samples were centrifuged at 20,800×*g* for 5 min, at 4 °C. The resulting supernatants were assayed for ATP, ADP, and AMP determination by separation in a reverse-phase high-performance liquid chromatography (HPLC), as described previously (Stocchi *et al.*, 1985). The chromatographic apparatus used was a Beckman-System Gold controlled by a computer. The detection wavelength was 254 nm, and the column used was a Lichrospher 100 RP-18 (5 μM). An isocratic elution with 100 mM phosphate buffer (KH_2PO_4), pH 6.5, and 1 % methanol was performed with a flow rate of 1 mL/min. Peak identity was determined by following the retention time of standards: 2.213 min ATP, 2.589 min ADP, 3.560 min AMP. The energy charges are defined as the ratio of the complete adenylate pool and are calculated as ([ATP]+0.5 [ADP])/([ATP]+[ADP]+[AMP]) (Atkinson, 1977).

2.10. O_2 consumption using Clark Electrode

Isolated mitochondria (400 μg) were resuspended in a standard KCl-reaction buffer (125 mM KCl, 3 mM K_2HPO_4, 0.5 mM $MgCl_2$, 10 mM HEPES and 10 μM EGTA – pH 7.4), as previously described (Pellman *et al.*, 2015), and placed in an oxygen electrode chamber (DW1, Clark electrode, Hansatech, UK), at 30°C, after calibration for dissolved oxygen. After recording the basal rate of oxygen consumption (in nmol/mL/min), mitochondria were energized with 3 mM succinate and O_2 consumption recorded. Then, mitochondria were challenged with 25 μM of ADP-K^+, followed by 2 μg/mL oligomycin and 2.5 μM carbonyl cyanide 3-chlorophenylhydrazone (CCCP) to achieve maximum respiration. Potassium cyanide (KCN) (700 μM) was added at the end of the experiment to confirm the involvement of mitochondrial complex IV on O_2 consumption.

2.11. Mitochondrial Membrane Potential

Mitochondrial membrane potential ($\Delta\psi_m$) was assessed using the fluorescent probe Rhodamine 123 (Rh123), which predominantly accumulates in polarized mitochondria, in both fresh isolated mitochondria from the cerebellum and brainstem and also in PC6-3 cells. Briefly, 10 μg of mitochondria isolated as previously described were resuspended in the previously described standard KCl-reaction buffer containing 50 nM Rh123, 0.1 mM ADP and supplemented either with 3 mM succinate (Suc) plus 3 mM glutamate (Glut) or 3 mM pyruvate (Pyr) plus 1 mM malate (Mal) to feed mitochondrial Complex II or Complex I, respectively, and basal fluorescence was immediately recorded. Succinate was used in combination with glutamate to prevent the accumulation of oxaloacetate and inhibition of succinate dehydrogenase, as previously described (Pellman *et al.*, 2015). PC6-3 cells ($0.5x10^6$ cells/condition) were incubated in KREBS buffer (132 mM NaCl, 4 mM KCl, 1 mM $CaCl_2$, 1.2 mM NaH_2PO_4, 1.4 mM $MgCl_2$, 6 mM glucose and 10 mM HEPES – pH 7.4) containing 3 μM Rh123 for 30 min at 37°C. In both experiments basal fluorescence was measured for 5 min, followed by the addition of 2.5 μM FCCP plus 2.5 μg/mL oligomycin, which produced maximal mitochondrial depolarization. Fluorescence (505 nm excitation and 525 nm emission) was measured (at 30°C for isolated mitochondria; 37°C for PC6-3 cells) using a microplate reader Spectrofluorometer Gemini EM (Molecular Devices, USA).

2.12. Mitochondrial Ca^{2+} uptake capacity

Mitochondrial calcium uptake was assessed in mitochondria isolated from the cerebellum and brainstem using the fluorescence probe Calcium Green-5N (Ca^{2+} Green), which binds extramitochondrial calcium. Fluorescence was measured at 30°C using a microplate reader Spectrofluorometer Gemini EM (Molecular Devices, USA). For this purpose, 5 μg of isolated mitochondria were resuspended in the standard KCl-reaction buffer containing 150 nM Ca^{2+} Green plus 0.1 mM ADP and 1 μM oligomycin, supplemented either with succinate (3 mM) plus glutamate (3 mM) or pyruvate (3 mM) plus malate (1 mM) to feed mitochondrial Complex II or Complex I, respectively. After basal fluorescence recording, mitochondria were subjected to two sequential loads of

10 μM Ca^{2+}, following a third load of 2 μM FCCP. The effect of 10 μM of RU 360, a mitochondrial calcium uniporter (MCU) inhibitor, was also tested.

2.13. Intracellular Ca^{2+} Recordings

The levels of intracellular free calcium were measured in PC6-3 using the fluorescent probe Fura-2/AM, which permeates the plasma membrane and has high affinity for calcium. Cells ($0.5x10^6$ cells/condition) were incubated in the previously described KREBS buffer (with 1 mM $CaCl_2$) containing 5 μM of Fura-2/AM at 37°C, for 30 min. Cells were then centrifuged at 70x*g*, at 20°C for 5 min and the pellet was resuspended in KREBS buffer without the probe. Basal fluorescence was measured at 37°C using a microplate reader Spectrofluorometer Gemini EM (Molecular Devices, USA) with 340/380 nm excitation and 510-nm emission wavelengths. After a baseline recording, cells were subjected to the addition of 2.5 μM FCCP plus 2.5 μg/mL oligomycin to depolarize mitochondria. The levels of intracellular free calcium were calculated as the ratio of the fluorescence intensity at 340 nm and 380 nm corresponding to maximal fluorescence of the probe in the presence of calcium and in the absence of calcium, respectively.

2.14. Mitochondrial H_2O_2 Production

The production of mitochondrial H_2O_2 was measured through Amplex®Red Hydrogen Peroxide/Peroxidase method. The reagent Amplex®Red (10-acetyl-3.7-dihydroxyphenoxazine), in the presence of the enzyme Horseradish peroxidase (HRP), reacts with H_2O_2 forming resorufin, a fluorescent product of oxidation. This way the fluorescence intensity is proportional to the amount of H_2O_2. Mitochondria were incubated in the standard reaction buffer containing 2 μM Amplex®Red and 0.5 units HRP, supplemented either with 3 mM succinate plus 3 mM glutamate or 3 mM pyruvate plus 1 mM malate as previously described. Basal fluorescence (571 nm excitation and 585 nm emission) was measured at 30°C using a microplate reader Spectrofluorometer Gemini EM (Molecular Devices, USA). A control was performed in

which 0.25 μM of H_2O_2 was added to the medium containing Amplex®Red plus HRP (in the absence of mitochondria).

2.15. Image analysis

Mitochondrial morphology was analysed using Macros deigned by Dr. Jorge Valero (CNC, University of Coimbra, presently at Achucarro – Basque Centre for Neuroscience, Spain) in Fiji (ImageJ, National Institute of Health, USA) (Attachment **1.2**). In the first place, to be considered for analysis each cell was delineated as a region of interest (ROI) (Attachment **1.1**). Then the background image was normalized using the function Subtract Background. In order to analyse mitochondrial morphology the cells were tansfected with MitoDsRed, which targets mitochondria, or incubated with an antibody that targets the protein Hsp60. Images were extracted to grayscale. Consequently, in order to show mitochondria specific fluorescence, the function *FindFoci* was used as it identifies the peak intensity regions (Herbert *et al.*, 2014). A threshold was applied to optimally resolve individual mitochondria. The function *Analyse Particles* traces the mitochondrial outlines. The Aspect Ratio, the ratio between the major and minor axis of mitochondria, as well as Roundness, the relation between mitochondrial area and its major axis, were obtained.

2.16. Statistical analysis

All statistical analysis and graphs were performed using GraphPad Prism 5 (GraphPad Software, San Diego, CA, USA). Data were expressed as mean ± SEM of the number of experiments as described in the figure legends. Comparisons among multiple groups were analysed using two-way ANOVA followed by Bonferroni *post-hoc* test or by Student's *t*-test for comparison between two groups, as indicated in the figure legends. Significance was accepted at $p<0.05$.

Chapter 3

Results

3.1. Analysis of mutant ATXN3 in PC6-3 cells and MJD135 mice

In order to evaluate the presence of mutant ATXN3 in the MJD models used in this work the expression of mutant ATXN3 was verified by western blotting (Fig. **3.1**), by using an antibody specific for ATXN3 and another that detects polyQ expansions higher than 37 glutamines (Q). PC6-3 Q108 cells demonstrated a clear shift in bands corresponding to mutant ATXN3 (Fig. **3.1 A**), since the polyglutamine expansion increases the protein's molecular weight (~66 kDa), whereas Q28 cells presented a band with lower molecular weight corresponding to wild-type ATXN3 (~47 kDa). In both cases we were able to observe the presence of a band with an even lower molecular weight (~42 kDa) corresponding to endogenous ATXN3 (Fig. **3.1 A**). Q108 cells also exhibited a band with a higher molecular weight, when incubated with the antibody for the polyglutamine expansion, corresponding to mutant ATXN3 (Fig. **3.1 B**). Regarding the mice model, western blotting was performed using mitochondria isolated from cerebellum and brainstem of MJD135 and WT mice. The presence of endogenous ATXN3 was observed in isolated mitochondria from both brain regions (Fig. **3.1 C**). Although ATXN3 is a mainly cytosolic and nuclear protein, our results are in accordance with studies demonstrating that it can be also found in mitochondria (Trottier *et al.*, 1998). However our results evidenced no differences in the levels of mutant ATXN3 and the polyglutamine expansion (data not shown) between MJD135 and WT mice which could indicate that mutated ATXN3 may not be capable of translocating towards this organelle and/or that the amount of protein was not sufficient to detect the mutant form of the protein associated with mitochondria.

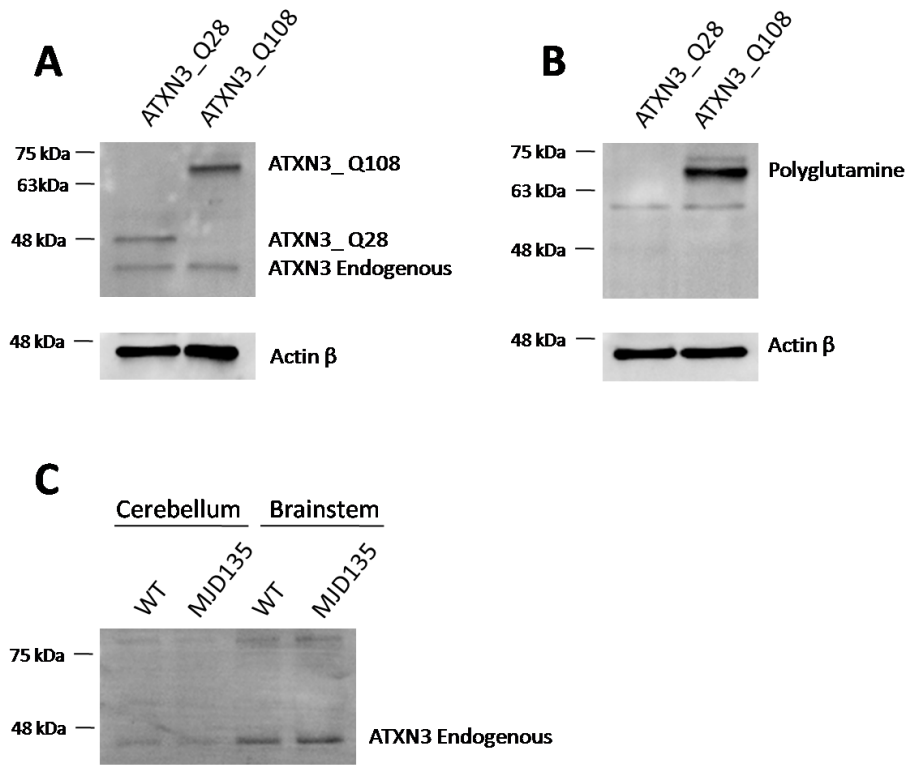

Figure 3.1 - Analysis of mutant ATXN3 in PC6-3 cells and MJD mice.

Total protein levels of ATXN3 (**A**) and the polyglutamine expansion (**B**) were evaluated in total extracts obtained from PC6-3 cells. Total protein levels of ATXN3 were assessed in mitochondria isolated from the cerebellum and brainstem of MJD135 *versus* WT mice (**C**), by western blotting.

3.2. PC6-3 Q108cells exhibit decreased levels of PGC-1α and unaltered levels of TFAM

Mitochondrial biogenesis is a multistep process that plays an important role in regulating the number of mitochondria in the cell. Previous studies have demonstrated that several neurodegenerative disorders exhibit reduced number of mitochondria and decreased levels of proteins involved in mitochondrial biogenesis (Cui *et al.*, 2006; St-Pierre *et al.*, 2006; Kim *et al.*, 2010). Therefore, we decided to evaluate the levels of peroxisome proliferator-activated receptor γ coactivator-1 (PGC-1α) and mitochondrial transcription factor 1 (TFAM), two proteins that play key roles in mitochondrial biogenesis.

PGC-1α plays an important role in enhancing cell viability, regulating mitochondrial biogenesis, stimulating mitochondrial respiration and increasing the levels of proteins involved oxidative phosphorylation (OXPHOS). Previous studies have demonstrated that overexpression of PGC-1α increases the number of mitochondria, enhances mitochondrial respiration and increases the levels of anti-apoptotic proteins (Mäkelä *et al.*, 2015). Our results showed that PC6-3 Q108 cells exhibited a significant decrease in the levels of PGC-1α when compared to Q28 cells (Fig. **3.2 A**). Thus, the decrease observed in proteins levels of PGC-1α in mutant cells could indicate impairment in mitochondrial biogenesis and associated processes, such as respiration.

TFAM is the main transcriptional regulator of mitochondrial DNA (mtDNA) as it coordinates the assembly of multiple DNA molecules and organizes mitochondrial chromatin (Kaufman *et al.*, 2007). TFAM's transcription is modulated by nuclear respiratory factor (NRF) 1 and 2, which are also regulated by PGC-1α. Taking this into account, we also analysed the levels of TFAM in PC6-3 cells and isolated mitochondria derived from cerebellum or brainstem of MJD135 *versus* WT mice (Fig. **3.2 B**, **C**). Data showed a tendency for a decrease that did not reach statistical significance in both MJD models, when compared with the respective controls (Fig. **3.2 B**, **C**). Our data indicates that although PGC-1α regulates TFAM, the decrease in PGC-1α was not accompanied by a significant decrease in TFAM levels.

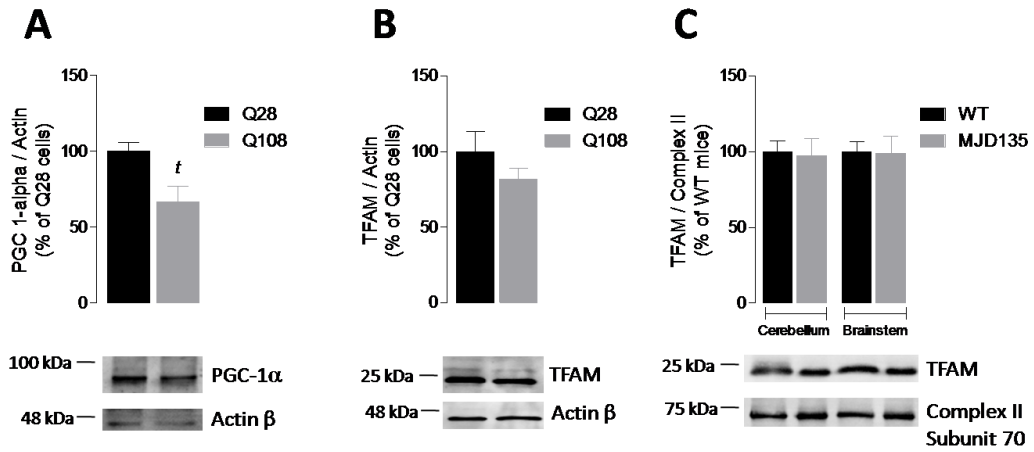

Figure 3.2 - Decreased levels of PGC-1α in PC6-3 Q108 cells and unaltered levels of TFAM in Q108 cells and brain mitochondria from MJD135 mice.

Total protein levels of PGC1-α (**A**) and TFAM (**B**) were evaluated in total extracts through western blotting. Data are the mean ± SEM of 4 different experiments. Total protein levels of TFAM were evaluated in mitochondria isolated from the cerebellum and brainstem of MJD135 *versus* WT mice (**C**), by western blotting. Data are the mean ± SEM of 6 different mice from each genotype. Statistical analysis was performed by Student's *t*-test: $^{t}p<0.05$, compared to Q28 cells.

3.3. MJD135 mice exhibit decreased cerebellar and brainstem maximal respiration and reduced cerebellar ATP production

Impairment of mitochondrial respiration is a common hallmark in several neurodegenerative disorders. Recently, a study using a sensitive high-resolution respirometric (HRR) method demonstrated that mitochondria from the striatum of the R6/2 mouse model of HD exhibited decreased respiration (Aidt, *et al*., 2013). Since we observed decreased PGC-1α, which is involved in mitochondrial biogenesis and function, in the cellular model of MJD, we further analysed mitochondrial respiration in isolated mitochondria obtained from the cerebellum and brainstem of MJD135 *versus* WT mice by using Seahorse XF24 flux analyser (Fig. **3.3**). Cerebellar mitochondria from MHD135 mice exhibited a decrease in mitochondrial respiration after full energizing with ADP (Fig. **3.3 A-C**), however, no differences in basal respiration or state 3/sate 4 ratio were observed in both brain regions (Fig. **3.3 D**, **G**). Both cerebellar and brainstem mitochondria exhibited decreased maximal respiration (Fig. **3.3 E**), achieved after FCCP stimulus in order to completely depolarize the organelle; however decreased mitochondrial ATP production (evaluated after addition of oligomycin) and decreased proton leak were only observed in cerebellar mitochondria from MJD135 mice, when compared to WT mice (Fig. **3.3 A, B, C, F**, **H**). These data suggest that mitochondria from MJD135 have lower respiratory capacity than mitochondria from WT mice and that mitochondria from cerebellum appear to be more susceptible than mitochondria from brainstem.

Analysis of mitochondrial respiration was also performed using a different technique, the Clark electrode. Oxygen consumption was evaluated in mitochondria isolated from the brainstem of MJD135 *versus* WT mice. However, no differences were found between MJD135 and WT mice regarding basal respiration, ATP production, state 3/state 4 and maximal respiration (Fig. **S2 A-D**).

Mitochondria are responsible for the production of ATP in the cells. Since we observed a significant decrease in ATP production in cerebellar mitochondria we decided to evaluate the total levels of adenine nucleotides, in tissue obtained from the cerebellum and brainstem of MJD135 *versus* WT mice, by reverse phase HPLC. We

observed unchanged ATP, ADP and AMP, as well as the ADP/ATP ratio (Fig. **S1 A-D**). We also analysed energy charges and found that cerebellar mitochondria from MJD135 exhibit a tendency to decrease (Fig. **S1 E**), but with no statistical significance (*p=0.06*).

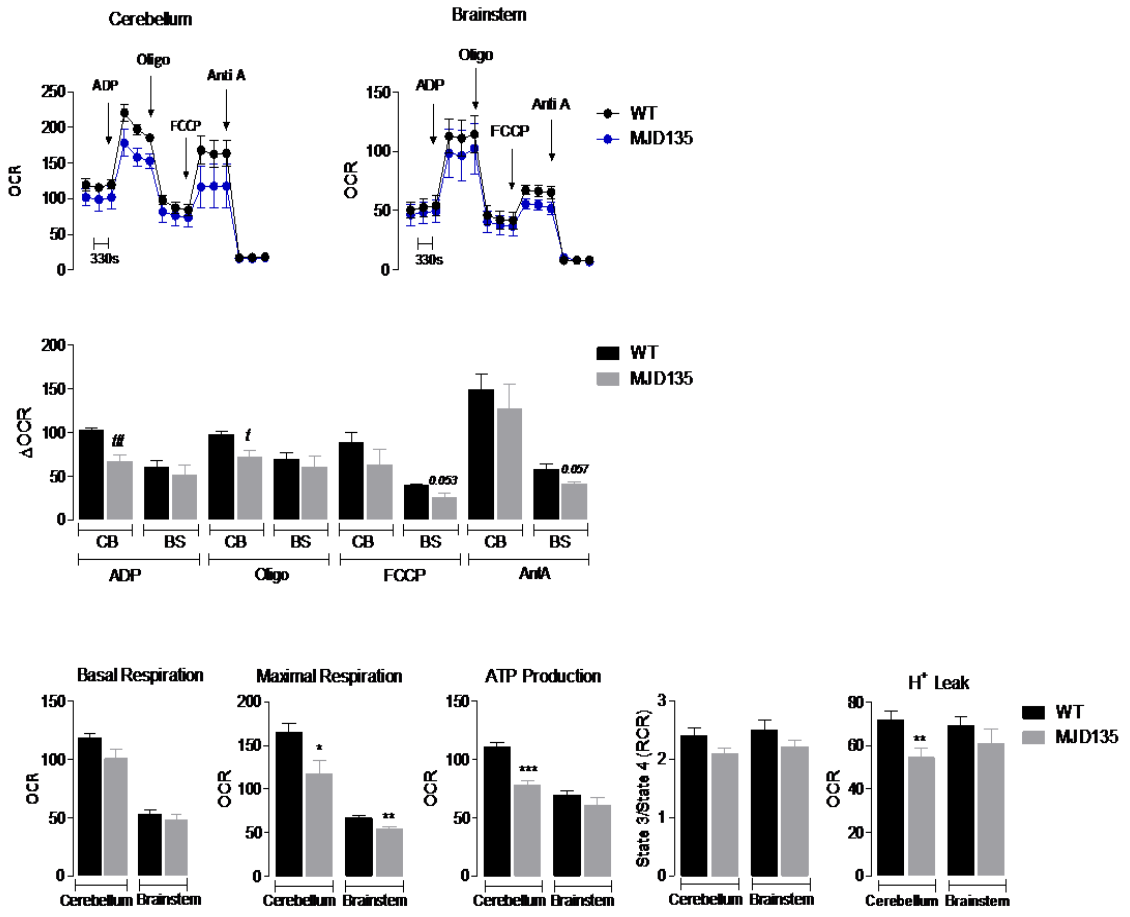

Figure 3.3 - MJD135 mice exhibit decreased cerebellar and brainstem maximal respiration and reduced cerebellar ATP production and H^+ proton leak.

Oxygen consumption rate (OCR; pmol/min/μg protein) were evaluated in mitochondria isolated from cerebellum and brainstem as described in *Methods 2.4.* Mitochondria were resuspended in MAS supplemented with 10 mM succinate (Complex II substrate) and 2 μM rotenone (Complex I inhibitor). Mitochondria respiration was assessed by sequential addition of 4 mM ADP, 2.5 μg/ml oligomycin (Oligo), 4 μM FCCP and 4 μM antimycin A (AntA) by using Seahorse XF24 flux analyser. Representative traces are shown in cerebellum (**A**) and brainstem (**B**). Variations in OCR (ΔOCR) for both regions are represented in (**C**). Mitochondrial basal respiration (**D**), maximal respiration (**E**), ATP production (**F**), state 3/state 4 (**G**) and proton (H^+) leak (**H**) were calculated accordingly to *XF Cell Mito Stress Test Parameters.* Data are the mean ± SEM of 3-6 mice from each genotype. Statistical analysis by Student's *t*-test: $^{t}p<0.05$, $^{tt}p<0.01$ and $^{ttt}p<0.001$, compared to WT mice.

3.4. MJD135 mice exhibit unaltered cerebellar and brainstem mitochondrial complexes activities but decreased levels of cytochrome c

As shown before (section 3.3) MJD135 mice exhibited decreased mitochondrial respiration, therefore we decided to evaluate if this decrease could be associated with alterations in the activity of the mitochondrial respiratory chain. Thus, we analysed the activity of complexes I, II, III and IV of the mitochondrial respiratory chain, using the Seahorse XF24 flux analyser (Fig. **3.4 A**, **B**). This was achieved by sequential addition of complex modulators and inhibitors, such as rotenone (Rot), a complex I inhibitor; succinate (Suc), a substrate of complex II; antimycin A (AntA), an inhibitor of complex III and Ascorbate /TMPD (Asc/TMPD), which allow electron flow to complex IV, to mitochondria isolated from the cerebellum and brainstem of MJD135 *versus* WT mice. The modulation of the mitochondrial respiratory chain was only possible because the MAS medium was previously supplemented with FCCP which leads to mitochondrial uncoupling thus allowing us to modulate the different complexes. The medium also contained pyruvate and malate, which feed mitochondrial complex I. Data showed no differences in mitochondrial complexes activities of either brain region (Fig. **3.4 D-G**).

In order to further explain the changes in mitochondrial respiration in cerebellum and brainstem of MJD135 *versus* WT mice, we analysed the protein levels of cytochrome c by western blotting. Interestingly, cerebellar mitochondria from MJD135 mice exhibited a significant decrease in total cytochrome c protein levels, whilst no differences were observed in brainstem mitochondria (Fig. **3.4 H**). Cytochrome c promotes the transfer of electrons from complex III to complex IV, culminating with the production of ATP (Rich and Marechal, 2010). Thus the decrease in protein levels of cytochrome c may lead to decreased ATP production, correlating with the results previously obtained in cerebellar mitochondria.

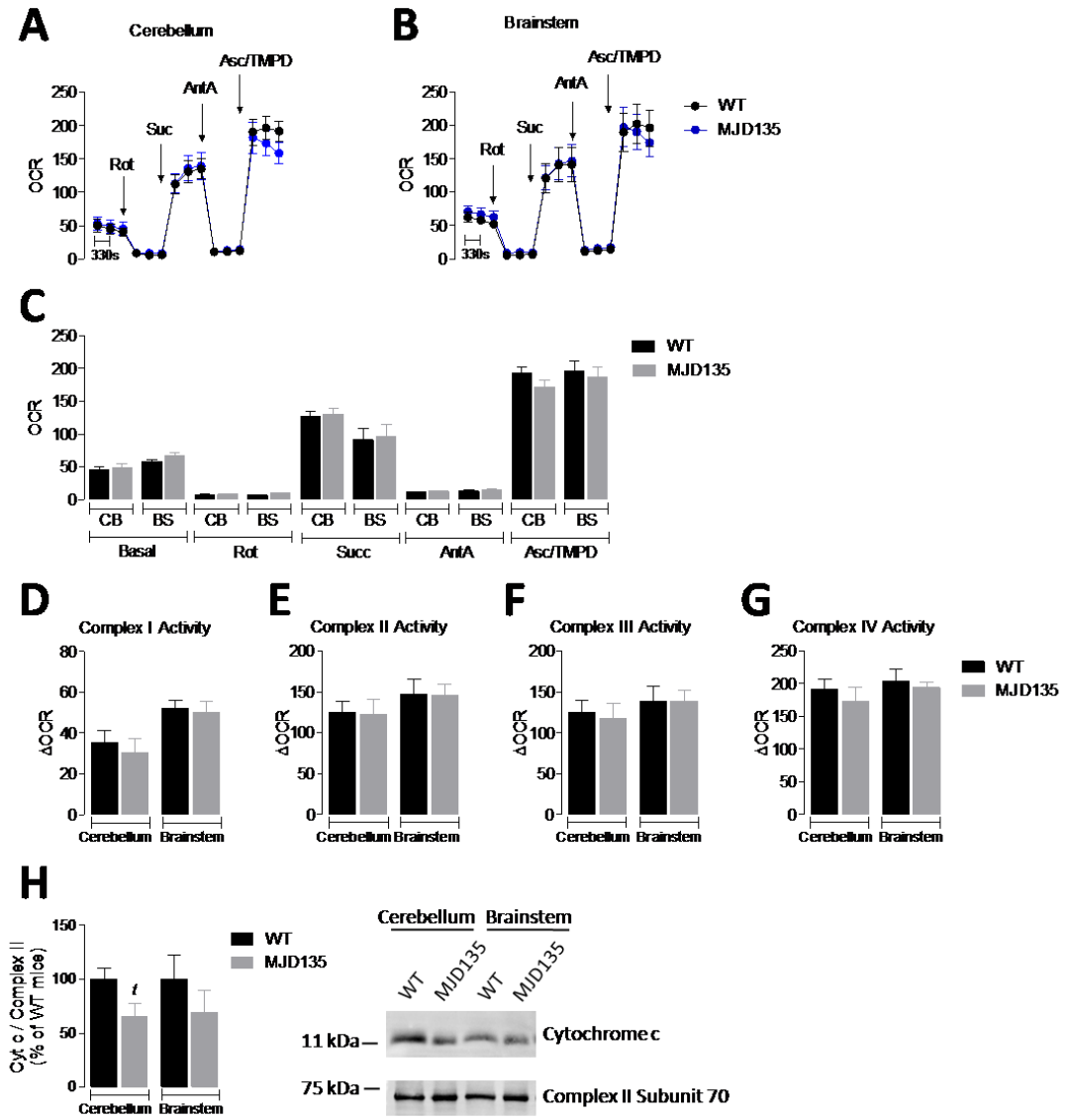

Figure 3.4 - Unchanged cerebellar and brainstem mitochondrial complexes activities but decreased cytochrome c protein levels in cerebellar mitochondria from MJD135 mice.

Oxygen consumption rate (OCR; pmol/min/µg protein) were evaluated in mitochondria isolated from the cerebellum and brainstem as described in *Methods 2.4.* Isolated mitochondria were resuspended in MAS supplemented with 10 mM pyruvate, 2 mM malate (mitochondrial substrates) and 4 µM FCCP (mitochondrial uncoupler). Mitochondrial respiration were assessed by sequential addition of 2µM rotenone (Rot), 10 mM succinate (Suc), 4 µM antimycin A (AntA) and 10 mM/100 µM Ascorbate /TMPD (Asc/TMPD) by using Seahorse XF24 flux analyser. Representative traces for cerebellum and brainstem are shown in (**A**, **B**), respectively. Maximal and minimal values achieved in (**A**, **B**) are represented in (**C**) for both brain regions. Complex I (**D**), Complex II (**E**), Complex III (**F**) and Complex IV (**G**) activities were calculated based on the response to the addition of mitochondrial modulators (inhibitors and substrates). (**H**) Total protein levels of cytochrome c were analysed in mitochondria isolated from the cerebellum and brainstem of MJD135 *versus* WT mice through western blotting. Data are the mean ± SEM of 3-6 mice from each genotype run in triplicates and 5 experiments. Statistical analysis was performed by Student's *t*-test: $^{t}p<0.05$, compared to WT mice.

3.5. MJD135 mice and PC6-3 Q108 cells display decreased mitochondrial membrane potential

The ability of mitochondria to perform their functions greatly depends on the maintenance of the mitochondrial membrane potential ($\Delta\psi_m$), as depolarized mitochondria activate mitophagy pathways and exhibit altered mitochondrial dynamics. It has been demonstrated that mitochondria from accurate models of HD exhibit decreased $\Delta\psi_m$ and, consequently, decreased ability to retain calcium (Oliveira *et al*., 2006.). Thus the analysis of mitochondrial membrane potential was assessed in both MJD135 mice and PC6-3 cells expressing mutant ATXN3.

We were able to observe that MJD135 mice show a significant decrease in membrane potential of cerebellar mitochondria whereas no alterations could be found in mitochondria from brainstem (Fig. **3.5 A-C**). Concordantly, these results were validated by our cell model as PC6-3 Q108 cells also exhibited a significant decrease in mitochondrial membrane potential (Fig. **3.5 D, E**). This suggests expression of ATXN3 causes that mitochondrial depolarization, particularly affecting cerebellar mitochondria. We were also able to observe a significant difference between the two supplemented media as brainstem mitochondria incubated in the medium supplemented with pyruvate plus malate showed a significant decrease in $\Delta\psi_m$ when compared to the medium supplemented with succinate plus glutamate. As succinate and glutamate are substrates of complex II, while pyruvate plus malate are substrates for complex I, our results suggest that feeding complex II, which then affects complex III activity, may play a role in mediating alterations in $\Delta\psi_m$. Since the maintenance of $\Delta\psi_m$ is essential for normal mitochondrial functioning, many cellular processes could be altered in these MJD models, such as calcium handling, mitochondrial dynamics and ROS production, among others.

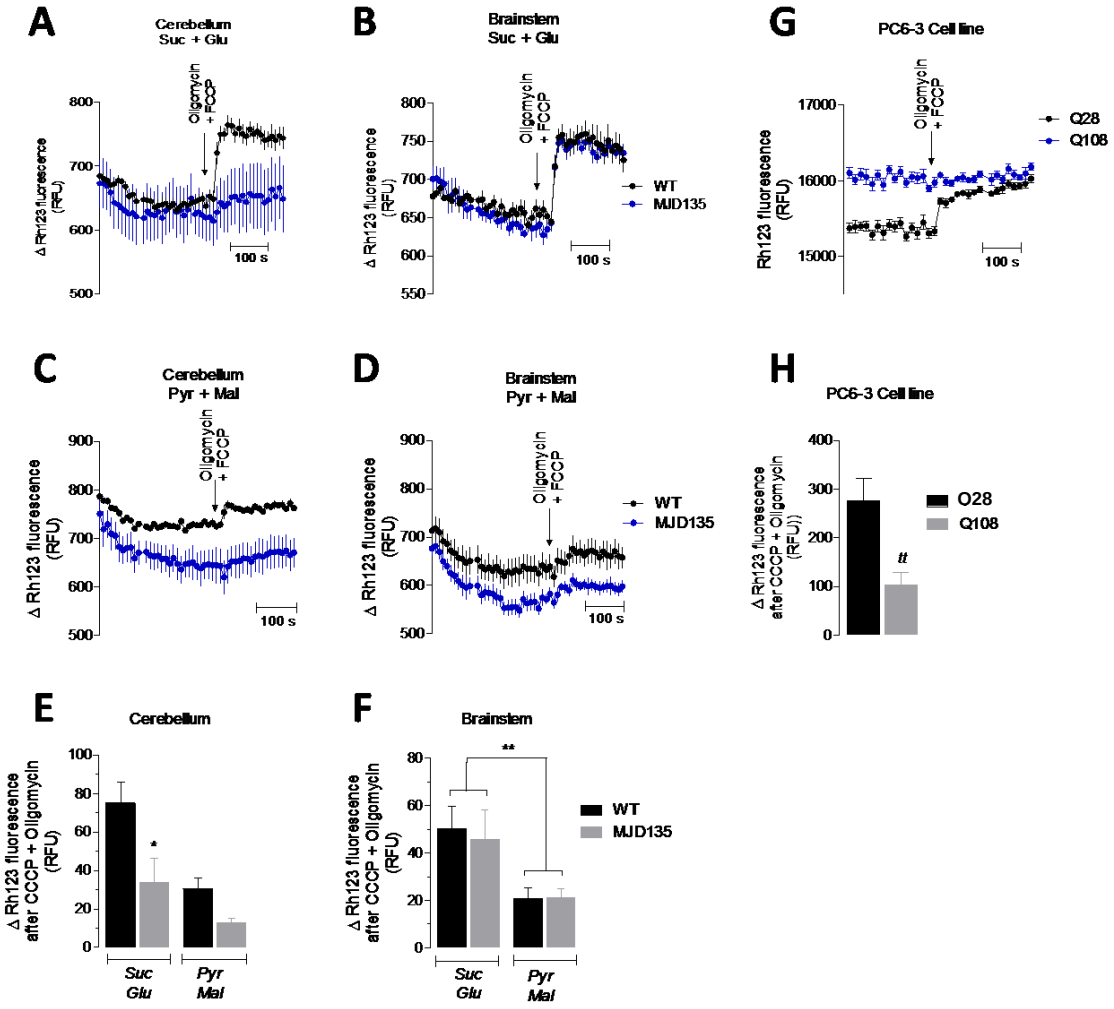

Figure 3.5 - MJD135 mice and PC6-3 Q108 cells display decreased mitochondrial membrane potential.

Mitochondrial membrane potential was assessed in mitochondria isolated from the cerebellum and brainstem of MJD135 *versus* WT mice (**A-F***)* and in PC6-3 cells (**G, H**) using the fluorescence probe Rhodamine 123. Isolated mitochondria were incubated in a standard KCl-based incubation medium containing 50 nM Rh123 and 0.1 mM ADP, supplemented either with 3 mM succinate plus 3 mM glutamate (**A, B**) or 3 mM pyruvate plus 1 mM malate (**C, D**). PC6-3 cells were incubated in KREBS buffer containing 3 µM Rh123 for 30 min at 37°C. In both experiments basal fluorescence (505 nm excitation and 525 nm emission) was measured using a microplate reader Spectrofluorometer Gemini EM (Molecular Devices, USA), for 5 min, followed by the addition of 2.5 µM FCCP plus 2.5 µg/mL oligomycin, which produced maximal mitochondrial depolarization. Data are mean ± SEM of 5-6 mice from each genotype, run in quadruplicates and 4 experiments, run in triplicates. Statistical analysis was performed by two-way ANOVA, followed by Bonferroni post-hoc test: $^{*}p<0.05$ compared to WT mitochondria; $^{**}p<0.01$, compared to medium with succinate plus glutamate and by Student's *t*-test: $^{tt}p<0.01$, compared to Q28 cells.

3.6. MJD135 mice exhibit decreased cerebellar mitochondrial calcium handling

One of the main cellular functions of mitochondria is regulating intracellular calcium homeostasis, which is fundamental for cell survival as the accumulation of calcium can lead to excitotoxicity. Impaired calcium handling has already been linked to MJD as ATXN3-expressing neurons exhibited decreased intracellular free calcium (Chen *et al.*, 2008). Thus mitochondrial calcium handling was evaluated in mitochondria isolated from MJD135 *versus* WT mice whereas intracellular free calcium was measured in PC6-3 cells.

Isolated mitochondria were incubated in the standard reaction buffer supplemented either with succinate plus glutamate (Fig. **3.6 A**, **B**) or pyruvate plus malate (data not shown). Both cerebellar and brainstem mitochondria, supplemented with succinate plus glutamate, exhibited decreased Ca^{2+} uptake capacity when subjected to a stimulus of 10 μM Ca^{2+}. Furthermore, MJD135 cerebral mitochondrial appeared to be more sensitive to calcium as their ability to uptake calcium significantly decreased after the second stimulus (Fig. **3.6 A**, **C**), whereas mitochondria isolated from the brainstem of MJD135 mice exhibited significant decrease after both stimulus but no significant difference between the first and second load (Fig. **3.6 B**, **C**). Mitochondria supplemented with pyruvate and malate were not able of taking up calcium (data not shown). This difference between the two mediums was also observed in the previous $\Delta\psi_m$ experiments leading to the conclusion that alterations in mitochondrial function are more aggravated when mitochondria are incubated with substrates of complex II. In order to evaluate if the uptake of calcium was mediated by the mitochondrial calcium uniporter (MCU), the reaction buffer supplemented with succinate plus glutamate was supplemented with RU 360, an inhibitor of the MCU. When incubated with RU 360 mitochondria lost their calcium retention capacity, meaning that the uptake of calcium by mitochondria is indeed mediated by the MCU (Fig. **3.6 E**, **F**). Regarding the PC6-3 cell line, no differences were observed in intracellular levels of free calcium between Q108 and Q28 cells (Fig. **3.6 I**, **J**).

Data implies that calcium handling is compromised in mitochondria from MJD135 mice. Results in cerebellar mitochondria are in agreement with the previous data showing decreased mitochondrial membrane potential, as depolarized mitochondria are less capable of retaining calcium. Also mitochondria obtained from the MJD mouse brain (particularly the cerebellum) appear to be more sensitive to changes in mitochondrial in MJD PC6-3 cells.

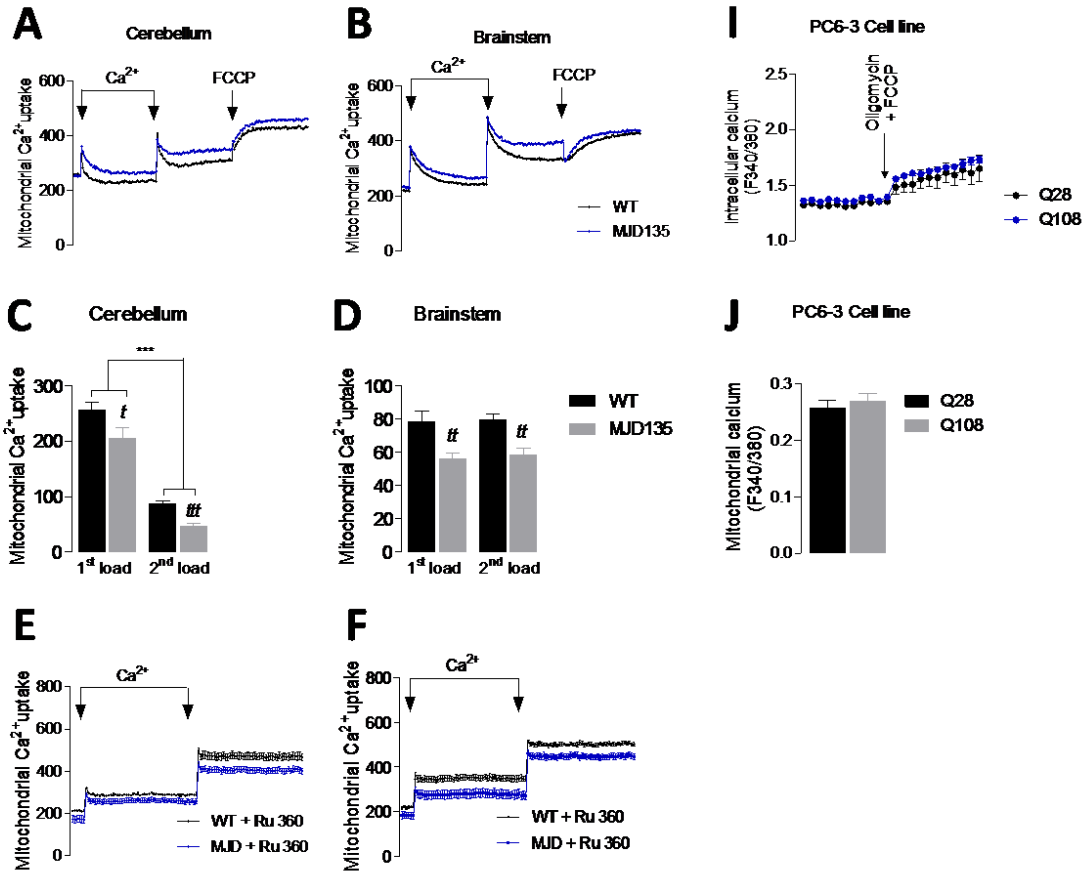

Figure 3.6 - MJD135 mice exhibit decreased cerebellar mitochondrial calcium retention.
Mitochondrial calcium uptake was assessed in mitochondria isolated from the cerebellum (**A, C, E**) and brainstem (**B**, **D**, **F**) of MJD135 *versus* WT miceusing the fluorescence probe Ca^{2+} Green (150 nM), and mitochondrial intracellular Ca^{2+} was assessed in PC6-3 cells (**I, J**) using FURA 2AM (5μM). Isolated mitochondria were incubated in a standard KCl-based incubation medium containing 0.1 mM ADP and 1 μM oligomycin, supplemented with 3 mM succinate plus 3 mM glutamate. Mitochondria were subjected to 2 loads of 10 μM Ca^{2+}, in (**A**, **B**) a third load of FCCP (2 μM) was applied. In (**E**, **F**), the effects of 10 μM RU 360, a mitochondrial calcium uniporter (MCU) inhibitor, were tested in medium supplemented with succinate plus glutamate. In (**I**) PC6-3 cells were subjected to2.5 μM FCCP plus 2.5 μg/mL oligomycin. Data are mean ± SEM of 4 mice from each genotype, run in quadruplicates and 4 experiments run in triplicates. Statistical analysis was performed by two-way ANOVA and Bonferroni post-hoc test: $^{***}p<0.001$, and by Student's *t*-test: $^{t}p<0.05$, $^{tt}p<0.01$ and $^{ttt}p<0.001$, when compared to WT mice.

3.7. Unchanged basal mitochondrial H_2O_2 production in MJD135 mice

Mitochondria are the major producers of reactive oxygen species (ROS). Oxidative phosphorylationis characterized by the generation of ATP in an oxygen-dependent manner due to electrons flow in the respiratory chain, culminating with the reduction of oxygen to water in mitochondrial complex IV (Murphy, 2009). Complexes I and III are the main producers of ROS in the brain (Hroudová *et al.*, 2014). ROS are electrophilic molecules that can be divided in to two distinct groups: radical forms such as superoxide anion radical ($O_2^{\bullet -}$), and non-radical forms such as hydrogen peroxide (H_2O_2) (Holmström and Finkel, 2014). Increased ROS levels can be very damaging to the cell as it leads to increased mtDNA damage. Moreover, several studies have considered oxidative stress, due to imbalance in the production of ROS, as a hallmark of many neurodegenerative diseases, such as Alzheimer's disease (AD) and HD.

Therefore, we decided to analyse the production of H_2O_2 in mitochondria isolated from the cerebellum and brainstem of MJD135 *versus* WT mice. No differences were observed regarding basal mitochondrial H_2O_2 production in either region (Fig. **3.7 E**, **F**). However, mitochondria incubated in the reaction buffer supplemented with succinate plus glutamate (Fig. **3.7 A**, **B**) exhibited a significant increase in H_2O_2 production when compared to medium supplemented with pyruvate plus malate (Fig. **3.7 D**, **C**), which was consistent in both brain regions. In order to corroborate the accuracy of our experiments, a control was performed in which 0.25 μM H_2O_2 was added to the reaction buffer without the presence of mitochondria (Fig. **3.7 G**).

Mitochondrial production of ROS depends on reverse electron flow which in turn depends on mitochondrial membrane potential (Korshunov *et al.*, 1997). Decreased $\Delta\psi_m$ is commonly associated with decreased production of ROS and vice-versa; however, we were able to observe decreased $\Delta\psi_m$ in cerebellar mitochondria of MJD135 mice but no differences in ROS production.

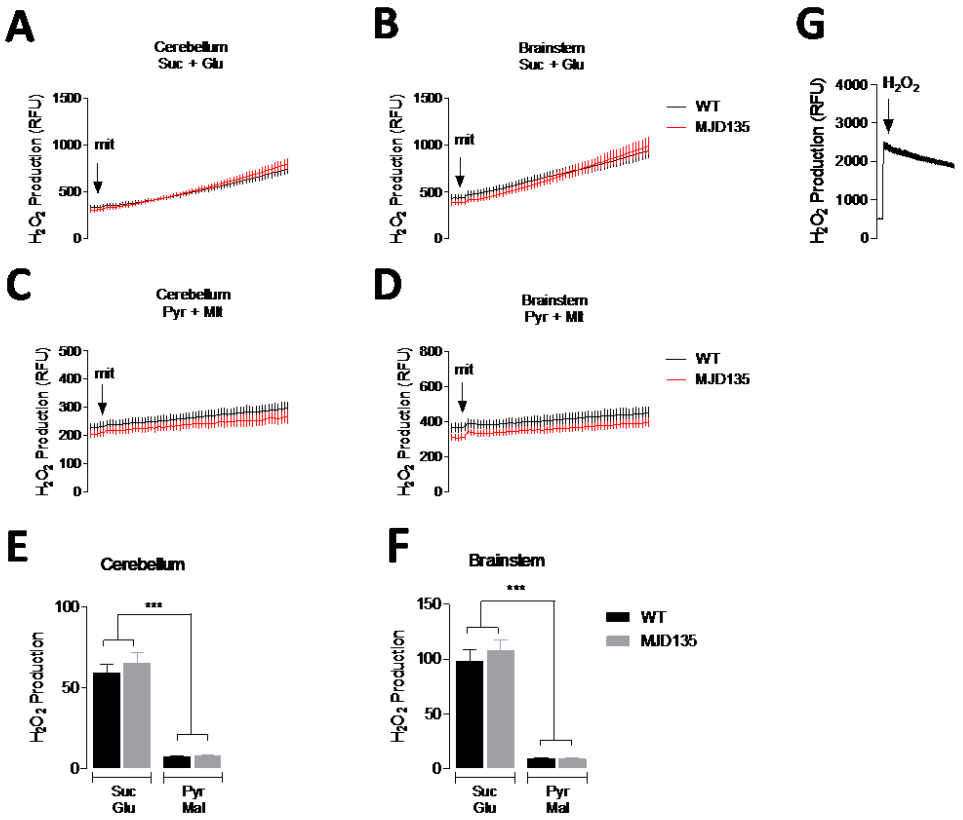

Figure 3.7 - Unaltered basal mitochondrial H_2O_2 production in MJD135 mice.

Mitochondrial H_2O_2 production was analysed in mitochondria isolated from the cerebellum (**A**, **C**, **E**) and brainstem (**B**, **D**, **F**) of 24-week-old MJD135 *versus* WT mice. The increase in mitochondrial H_2O_2 production was measured, at 30°C, under basal conditions by Amplex red (2 μM)/ Horseradish Peroxidase (0.5 U) fluorometry. Mitochondria were resuspended in the standard incubation medium supplemented either with 3 mM succinate plus 3 mM glutamate (**A**, **B**) or 3 mM pyruvate plus 1 mM malate (**C**, **D**). In (**G**) a control was performed in which 0.25 μM H_2O_2 was added to the medium without mitochondria. Data are mean ± SEM of 3-4 mice from each genotype, run in duplicates. Statistical analysis was performed by two-way ANOVA and by Bonferroni post-hoc test: $^{***}p<0.001$, when compared to the medium with succinate plus glutamate.

3.8. PC6-3 Q108 cells exhibit decreased fission and unaltered fusion

The balance between mitochondrial fission and fusion plays an important role in maintaining mitochondrial morphology and distribution (Su *et al.*, 2010). In order to better understand alterations in mitochondrial dynamics in MJD we analysed the levels of proteins involved in both fission and fusion using PC6-3 cells and MJD135 mice. To evaluate if mitochondrial fission is altered we analysed the proteins dynamin-related protein 1 (Drp1) and mitochondrial fission 1 (Fis1), whereas to evaluate fusion we analysed the protein levels of Mitofusin 2 (Mfn2) and optic atrophy 1 (OPA1). Drp1 is a guanosine triphosphate (GTP)ase that regulates fission of the outer mitochondrial membrane (OMM) by oligomerizing into ring-like structures at the sites of division, promoting constriction and scission (Mears *et al.*, 2011). Fis1 is a Drp1 receptor located at the OMM that mediates fission by binding Drp1 (Chen and Chan, 2004).

We observed significantly decreased levels of Drp1 in mitochondria-enriched subcellular fractions of Q108 cells, through western blotting, however no differences were observed regarding Drp1 levels in cytosolic-enriched fractions. We also evaluated the levels of Drp1 in mitochondria isolated from the cerebellum and brainstem of MJD135 mice, however, the results were not consistent with the cellular model, as no significant differences were observed between mutant and WT mice (Fig. **3.6 B**). Furthermore, Q108 cells exhibited decreased levels of Fis1 in mitochondrial enriched-fractions (Fig. **3.6 C**).

Fusion of the OMM is regulated by Mfn 1 and 2 which contain a GTP-binding domain capable of tethering OMMs together. Since Mfn 2 has a higher GTPase activity than Mfn1 only this protein was evaluated (Ishihara *et al.*, 2004; Koshiba, 2004). On the other hand, OPA1 is responsible for mediating IMM fusion and it can be cleaved into two functional isoforms (Ishihara *et al.*, 2006). No differences were found in the protein levels of Mf2 (Fig. **3.8 D**). We also analysed the levels of the isoform b of OPA1 (Fig. **3.8 E**), which has a lower molecular weight, and total levels of OPA1 (data not shown), however no differences were observed in either case, which suggests that mitochondrial fusion is not impaired in Q108 cells.

Overall, these data suggest that there is a decrease in mitochondrial fission and unchanged mitochondrial fusion in MJD cell models. Since an increase in mitochondrial

fission-associated proteins is correlated with mitochondria presenting a more fragmented morphology, one could argue that mitochondria from Q108 cells might present a more tubular morphology. However, in order to fully understand the impact of mitochondrial dynamics on the morphology of PC6-3 cells, other experiments must be performed such as the analysis of mitochondrial morphology by immunocytochemistry.

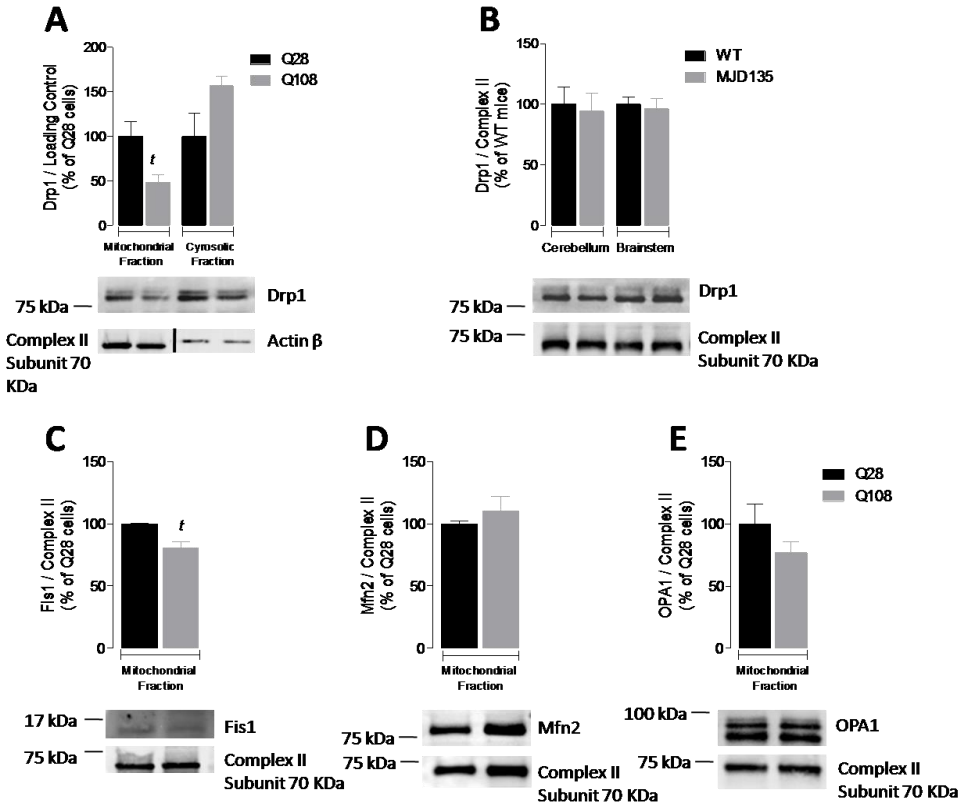

Figure 3.9 - Analysis of proteins involved in the fusion/fission machinery –Drp1 and Fis1 are decreased in PC6-3 Q108 cells only.

(**A**) Total protein levels of Drp1 were assessed in mitochondrial and cytosolic-enriched subcellular fractions and (**B**) in mitochondria isolated from the cerebellum and brainstem of MJD135 *versus* WT mice through western blotting. (**C, D, E**) Total proteins levels of Fis1, Mfn2 and OPA1 were assessed in mitochondrial-enriched subcellular fractions through western blotting. Data are mean ± SEM of 3-4 independent experiments and 5 mice from each genotype. Statistical analysis was performed by Student's *t*-test: $^{t}p<0.05$, compared to Q28 cells.

3.9. Alterations in proteins associated with autophagy and mitophagy

Autophagy is the process that occurs in eukaryotic cells by which intracellular components are degraded in the lysosome. This process can be divided in three mechanisms: microautophagy, chaperone-mediated autophagy, and macroautophagy (Codogno *et al.*, 2012). Mitophagy is a form of macroautophagy responsible for recognizing and removing dysfunctional mitochondria through degradation, thus playing an important role in maintaining cellular homeostasis. Previous studies have demonstrated that both autophagy and mitophagy are altered in many neurodegenerative disorders and that the accumulation of damaged mitochondria can increase disease pathogenesis. Therefore we decided to evaluate alterations in autophagy and mitophagy-associated proteins.

Sequestosome-1 (SQSTM1), also known as p62 is a polyubiquitin-binding protein that also serves as a cargo receptor for autophagic degradation. It is known for binding the autophagic effector protein LC3 (protein 1 light chain 3), due to its LC3-interacting region (LIR) motif, and other ubiquitinated proteins (Bjørkøy *et al.*, 2005; Pankiv *et al.*, 2007; Lin *et al.*, 2013). LC3,a member of the autophagy-related (ATG) proteins family, is a protein anchored in the membrane of the phagophore that binds and directs other proteins towards the lysossome for degradation. Both p62 and LC3 play crucial roles in the autophagic machinery.

Q108 cells exhibited significantly lower levels of p62 (Fig. **3.9 A**) when compared to Q28 cells, which could be corelated with an increase in autophagy.To evaluate the formation of autophagossomes we analysed the LC3-II/I ratio, since cytosolic LC3-I is converted into phosphatidylethanolamine (PE) conjugated LC3 (LC3-II), which is recruited to the membrane of the phagossome (Tanida *et al.*, 2008). However no significant differences were found betwen mutant and control cells (Fig. **3.9 B**), which indicates that there is no impairment in autophagossome formation. Nonetheless, when the levels of the LC3-II isoform, which is present in the membrane of the phagossome, were analysed, a significant decrease was observed in Q108 cells (Fig. **3.9 C**). Many studies associate neurodegenerative disorders with impaired autophagic

mechanisms, however, since p62 and the LC3 II isoform are degradated along with the autophagossome, thedecrease in the levels of both these proteins could possibly indicate that autophagy is being activated in mutant cells.

To better understand the impact of mutant ATXN3 inautophagic pathaways the PINK1/parkin-mediated mitophagy pahtway was evaluated through analysis of total protein levesl of PTEN-induced putative kinase 1 (PINK1) and phosphorilated parkin at serine 65 (S65). PINK1 is a serine/threonine kinase that accumulates in the OMM when mitchondria are depolarized. The accumluation of PINK1 recruits the E3 ligase parkin that is phosporilated by PINK1 at S65, consequently promoting the recruitment of atophagic receptors, such as p62 (Geisler *et al.*, 2010; Jin *et al.*, 2010; Shiba-Fukushima *et al.*, 2012; Chen and Dorn II, 2013).

Q108 cells exhibited a significant increase in total protein levels of PINK1 (Fig. **3.9 D**). However, no differences were found in the levels of phosphorylated parkin (S65) in either mitochondrial and cytosolic-enriched fractions, or in mitochondria isolated from the cerebellum and brainstem of MJD135 *versus* WT mice (Fig. **3.9 E**, **F**). The increased levels of PNIK1 associated with a decrease in p62 suggests that in Q108 cells there is activation of autophagic associated pathways. Furtermore, PC6-3 cells exhibited decreased $\Delta\psi_m$ which corroborrates these findings as mitophagy commonly targets damaged/depolarized mitochondria. Still, very little is known about the impact of altered autophagy in MJD and further studies must be carried out in order to corroborrate this hypothesis.

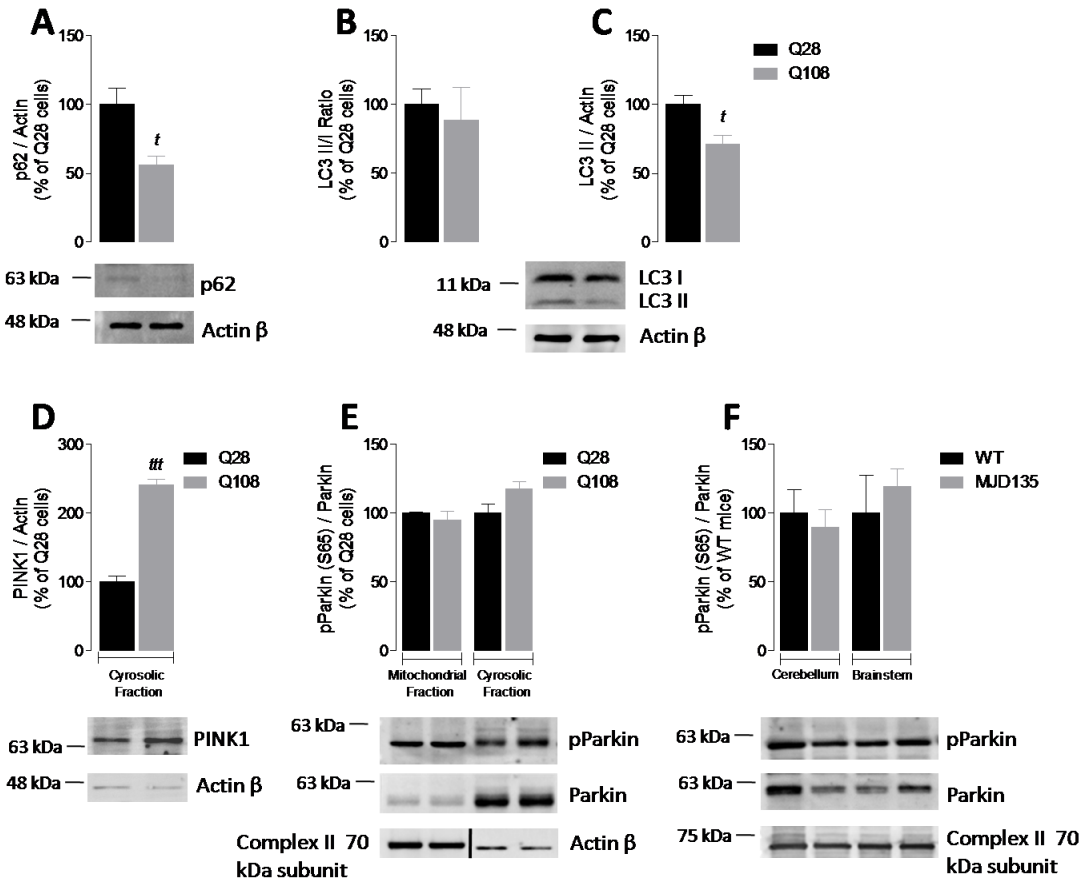

Figure 3.9 - Analysis of autophagy associated proteins in PC6-3 cells - Decreased levels of p62 in Q108 cells.

(**A**, **B**, **C**) Total protein levels of p62, LC3 A/B and total LC3 B were assessed in total extracts through western blotting. (**D**) Total proteins levels of PINK1 were assessed in cytosolic-enriched subcellular fractions through western blotting. (**E**) Total protein levels of pParkin were assessed in mitochondrial and cytosolic-enriched subcellular fractions and (**F**) in mitochondria isolated from the cerebellum and brainstem of MJD135 versus WT mice, through western blotting. Data are mean ± SEM of 4 independent experiments and 4 mice from each genotype. Statistical analysis was performed by Student's *t*-test: $^{t}p<0.05$ and $^{ttt}p<0.001$, compared to Q28 cells.

Chapter 4

Discussion

4.1. Discussion

Mitochondria are highly dynamic organelles that play an important role in maintaining cell homeostasis as they are responsible for regulating many processes vital for cell survival. One of the major roles of mitochondria is the synthesis of ATP, which is the main source of energy of the cell, through OXPHOS. Mitochondria also regulate calcium homeostasis, ROS production, apoptosis and overall cell metabolism.

Mitochondrial dysfunction has long been considered a hallmark of many neurodegenerative and polyQ disorders. The impact of alterations in mitochondrial function and dynamics has been thoroughly studied in disorders such as Alzheimer's, Parkinson's and Huntington's disease. Specifically in HD, which also belongs to the group of polyQ disorders, many mitochondrial processes have been shown to be compromised, namely mitochondrial biogenesis, respiration, membrane potential, calcium handling and fusion/fission balance. However, very little is known about the impact of mitochondrial dysfunction in MJD.

The co-transcriptional activator, PGC-1α, is involved in many mitochondrial processes such as mitochondrial biogenesis and respiration, among others. Its role on ROS metabolism has also been highlighted as PGC-1α overexpression was shown to be neuroprotective against oxidative stress (St-Pierre *et al.*, 2006; Mäkelä *et al.*, 2015). Therefore, the first step in evaluating mitochondrial dysfunction is characterizing mitochondria biogenesis as it is the major process responsible for regulating the number of mitochondria existing in the cell. To achieve this, the levels of PGC-1α, as well as, the levels of TFAM, which regulates mtDNA, were analysed. Previous studies have shown that both are decreased in HD and the profound impact of PGC-1α was further demonstrated when the knock-out of this co-transcription factor exacerbated the phenotype of HD mice whilst its overexpression promoted neuroprotection (Li and Li, 2004; Cui *et al.*, 2006; Kim *et al.*, 2010). Concordantly, Q108 cells exhibited decreased levels of PGC-1α (Fig. **3.2 A**). Although TFAM is regulated by PGC-1αneither MJD135 mice nor Q108 cells displayed alterations in the total levels of TFAM (Fig. **3.2. B**, **C**). Besides regulating TFAM, PGC-1α also regulates the activity of NRF 1 and 2, ATP synthase and superoxide dismutase 2 (SOD2). ATP synthase catalyses the conversion of

ADP and phosphate into ATP, whilst SOD2 is an antioxidant enzyme, which means that a decrease in these enzymes could promote decreased ATP production and increased ROS, respectively. These results represent the first clue suggesting impairment in mitochondrial biogenesis which could be translated into a decrease in the number of mitochondria and overall compromised mitochondrial function.

To further investigate this matter we analysed mitochondrial respiration in the cerebellum and brainstem of MJD135 mice (Fig. **3.3 A**, **B**), a topic that has not yet been thoroughly studied in MJD. We decided to study these specific brains regions since they are among the most affected in MJD; MJD135 mice were shown to exhibit higher accumulation of human ataxin-3 in the cerebellum, followed by the brainstem, forebrain and spinal cord (the last two were not evaluated in this study), and these results were similar when the human ATXN3 mRNA was analysed (Silva-Fernandes *et al.*, 2014).

The impact of mitochondrial respiration in polyQ models has been somewhat contradictory over the years. Using the YAC128 mice, Hamilton and co-authors observed similar O_2 consumption and argued against respiratory deficiency in this HD mouse model whilst a previous study using asensitive high-resolution respirometric (HRR) method demonstrated that mitochondria from the striatum of HD R6/2 mice exhibited decreased respiration (Aidt *et al.*, 2013; Hamilton *et al.*, 2015). Regarding the MJD135 mice model no alterations were found in basal respiration (Fig. **3.3 C**), however, both cerebellar and brainstem mitochondria exhibited decreased maximal respiration (Fig. **3.3 D**). No alterations in the state 3/sate 4 were observed in both brain regions, (Fig. **3.3 F**) but there was a decrease in ATP production and proton leak in cerebellar mitochondria (Fig. **3.3 F**, **G**). Proton leak is the process by which protons return to the mitochondrial matrix independently/alternatively of ATP synthase (e.g. Jastroch *et al.*, 2011) such as through the uncoupling proteins (UCPs). In order to further explore this concept, measuring the levels of UCP2 in isolated mitochondria and in PC6-3 cells could be a promising strategy. The observed ATP depletion and impaired respiration is in agreement with the decrease in PGC-1α, promoting the decrease in ATP due to decreased activity of ATP synthase. Data of total adenine nucleotide levels (determined in brain tissue extracts) did not corroborate the results obtained with Seahorse XF24 flux analyser, in which we analysed the production of

ATP in isolated mitochondria, but one should consider that the first accounts for both mitochondrial and glycolytic ATP production. Furthermore, the number of experiments performed with HPLC was lower (n=3), when compared to the analysis by the Seahorse apparatus, so we cannot fully make a conclusion from these results. We also analysed mitochondrial respiration in the brainstem using the Clark electrode. Although our previous results had shown a decrease in maximal mitochondrial respiration, no differences were observed using the Clark electrode (Fig. **S2**). Analyzing O_2 consumption in cerebellar mitochondria and in PC6-3 cells, through Clark electrode, would help enhance our findings. Nonetheless, the overall respiratory experiments demonstrated that the cerebellum is more affected in terms of mitochondrial dysfunction than the brainstem.

A small decrease in the activity of mitochondrial complex II was previously observed in differentiated PC6-3 cells expressing ATXN3 with 108 glutamines (Laço *et al.*, 2012b). Nevertheless, no differences were observed in the activity of either complex (Fig. **3.4**). This posed a controversy as we observed decreased respiration but no alterations in complexes activities, which lead to evaluate the levels of cytochrome c, a soluble protein located in the intermembrane space (IMS) that transfers electrons from complex III to complex IV, enabling complex IV to reduce molecular O_2 into water. Interestingly, this protein was significantly diminished in cerebellar mitochondria (Fig. **3.4 H**), which indicates that despite the normal activity of complex IV, less cytochrome c is available to promote electron flow along the respiratory chain thus resulting in decreased ATP production and respiration. The decrease in cytochrome c could be caused by an induction in apoptosis which results in mitochondrial cytochrome c being released into the cytosol or due to decreased transcription mediated by decreased levels of PGC-1α (which was already verified). An interesting approach to better clarify these results would be to measure the levels of cytochrome c mRNA in PC6-3 cells.

The primary mitochondrial bioenergetics parameter is the electrochemical proton motive force (Δp) which is primarily composed of the mitochondrial membrane potential ($\Delta\psi_m$) and mitochondrial pH gradient. Whilst the Δp controls mitochondrial ATP synthesis, the $\Delta\psi_m$ provides the charge gradient for calcium handling and ROS production thus playing an important role in cell survival (Nicholls and Ward, 2000; Perry *et al.*, 2011). Many studies have highlighted the importance of the maintenance

of the $\Delta\psi_m$ in the normal functioning of mitochondria. Striatal neurons from YAC128 HD mice presented decreased $\Delta\psi_m$ which compromised their ability to regulate calcium homeostasis thus contributing to neuronal dysfunction and eventually death (Oliveira *et al.*, 2006). In order to successfully characterize mitochondrial dysfunction in MJD both $\Delta\psi_m$ and mitochondrial calcium uptake capacity were evaluated. Accordingly with the results found in YAC128 HD mice (Oliveira *et al*., 2006), MD135 mice exhibited decreased cerebellar mitochondrial membrane potential (Fig. **3.5 A**, **C**) and decreased cerebellar mitochondrial Ca^{2+} uptake capacity (Fig. **3.6 A**, **C**). On the other hand, brainstem mitochondria exhibited decreased Ca^{2+} uptake capacity (Fig. **3.6 B**, **D**) but no alterations in mitochondrial membrane potential (Fig. **3.5 B, F**). In concordance with cerebellar mitochondria, Q108 cells also displayed a significant decrease in $\Delta\psi_m$ (Fig. **3.5 G**); however no changes were observed in intracellular calcium levels in Q108 cells (Fig. **3.6 I**, **J**). Furthermore, when mitochondria were incubated with an inhibitor of the MCU (RU360) no differences were observed in extramitochondrial calcium levels, meaning that mitochondria were not capable of taking up calcium, thus confirming that mitochondria from both brain regions mediate calcium handling through the MCU (Fig. **3.6 G**, **H**). These results support the earlier findings in which neurons expressing expanded ATXN3 exhibited depolarized mitochondria, compromised calcium handling and downregulation of genes involved in calcium signalling (Jeub *et al.*, 2006; Chen *et al.*, 2008; Chou *et al.*, 2008). Due to the relevance of decreased levels of PGC-1α, decreased respiration and decreased$\Delta\psi_m$ associated with decreased calcium uptake, several mitochondrial functions, such as mitochondria morphology, mitophagy and ROS production could be altered.

Some authors were able to demonstrate that the depletion of PGC-1α increased the sensitivity of neurons to oxidative stress (St-Pierre *et al.*, 2006). Taking into account the observed decrease in PGC-1α in Q108 cells, one could argue that it would translate into increased ROS production. On the other hand, the observed decrease in $\Delta\psi_m$ and proton leak could also be translated into changes in ROS levels. However, no alterations in basal mitochondrial H_2O_2 production were observed in either brain region (Fig. **3.7**), which could indicate that these processes might be balancing each other to maintain a steady production of H_2O_2, or that, contrary to what is seen in HD,

oxidative stress does not play an important role in MJD pathogenesis. One helpful approach that would allow a better understanding of this mechanism would be to analyse the levels of SOD2, as its activity is regulated by PGC-1α, coupled with the analysis of MitoSox, a mitochondrial superoxide indicator for live-imaging, in PC6-3 cells.

Mitochondrial morphology, distribution and number are regulated by the balance between fusion and fission events which in turn are mediated by several associated proteins, such Drp1 and Fis1 which mediated fission; Mfn2 and OPA1 which mediate fusion. Alterations in mitochondrial morphology can lead to mitochondrial fragmentation and cristae remodeling which play an important part in apoptosis (Frank *et al.*, 2001; Scorrano *et al.*, 2002; Oettinghaus *et al.*, 2016). Therefore, the characterization of mitochondrial fusion and fission-associated proteins in MJD models allow us to understand if mutant ATXN3 is capable of altering mitochondrial shape and size. Studies in both HD and PD have shown a more fragmented mitochondrial morphology and thus higher levels of fission-associated proteins (Kim *et al.*, 2010; Wang *et al.*, 2015). In contrast, Q108 cell exhibited decreased proteins levels of both Drp1 and Fis1 (Fig. **3.8 A**, **C**), indicating a decrease in fission events. Unfortunately, isolated mitochondria from MJD135 mice exhibited no alterations in the levels of Drp1 (Fig. **3.8 B**). The proteins Mfn2 and OPA1 remained unaltered in Q108 cells, indicating unaltered fusion (Fig. **3.8 D**, **E**). These results suggest that in Q108 cells fusion is favored which could cause mitochondria to be more elongated and fewer in number which has not been assessed yet.

In a recent study using the CMVMJD94 mouse model, treatment with 17-DMAG, an Hsp90 inhibitor, ameliorated the motor phenotype, increased proteins levels of beclin-1 and LC3-II, which led the authors to conclude that autophagy was being activated (Silva-Fernandes *et al.*, 2014). Zhou and collaborators (2014) demonstrated that the effector macroautophagy cargo protein p62 was capable of directly interacting with ATXN3 and promote aggresome formation. Moreover, they demonstrated that when p62 was inhibited there was an increase in mutant ATXN3-induced cell death. Another study demonstrated that, in several MJD models(tissue from patients, a lentiviral-rat model and a transgenic mouse model), there was accumulation of autophagy-associated markers, such as p62, LC3 and autophagic

protein 16 (Atg16L) and a decrease in the levels of beclin-.1 Furthermore, when beclin-1, which is essential for autophagy, was overexpressed there was an improvement in the clearance of ATXN3 and a decrease in neuronal dysfunction (Nascimento-Ferreira *et al.*, 2011).

Considering the evidences of reduced autophagy in MJD (Winborn *et* al., 2008; Nascimento-Ferreira *et* al., 2011) we further analysed the protein levels of p62, LC3-II and the formation of autophagosomes (LC3-II/I ratio) in the PC6-3 cell line. Q108 cells exhibited a significant decrease in p62 (Fig. **3.9 A**), which could indicate an increase in autophagy. We also observed no alterations in the LC3-II/I ratio (Fig. **3.9 B**), meaning that the formation of autophagosomes was not impaired, but were able to observe a decrease in LC3-II levels in Q108 cells (Fig. **3.9 C**). Several studies have shown that when autophagy is impaired there is an accumulation of p62 within ubiquitin aggregates (Rusten and Stenmark, 2010), whereas other studies have associated the decrease in LC3-II/I ratio and total proteins levels of LC3-II with decreased autophagy, which renders our results puzzling as we observed decreased levels of p62 and LC3-II. Moreover, in a conjunction of guidelines for measuring and interpreting autophagy it is claimed that the accumulation of LC3-II can be obtained by interrupting the autophagosome-lysosome fusion step or by inhibiting lysosome-mediated proteolysis. Conversely, a decrease in LC3-II relative to LC3-I could also be observed if degradation of LC3-II via lysosomal turnover is particularly rapid (Klionsky *et al.*, 2012). Consequently, the decrease observed in LC3-II could indicate that LC3-II is being degraded along with the authophagosome also leading to reduced p62 levels, thus suggesting autophagy activation in Q108 cells.

To better understand the impact of expanded ATXN3 in autophagic degradation we analysed a specific type of macroautophagy responsible for removing damaged mitochondria, mitophagy, which role has remained unknown in MJD. When mitochondria are depolarized (decreased $\Delta\psi_m$) PINK1 is incapable of crossing the OMM thus accumulating in the cytosol and initiating the mitophagy signalling network (Geisler *et al.*, 2010; Jin *et al.*, 2010; Shiba-Fukushima *et al.*, 2012; Chen and Dorn II, 2013). In steady-state conditions PINK1 travels to IMS where it is degraded which means that the cell normally presents low levels of basal PINK1. Therefore, the increased levels of PINK1 observed in Q108 cytosolic extracts (Fig. **3.9 C**) could indicate

a potential activation of mitophagy which is consistent with previous results as Q108 cells displayed decreased $\Delta\psi_m$. Moreover, we were incapable of detecting the presence of PINK1 in mitochondrial-enriched fractions (data not shown). Although the decrease observed in LC3-II is a controversial result, taken as a whole the results suggest that autophagy is being activated and possibly through the PINK1/parkin pathway. Mitochondria of Q28 and Q108 cells were labelled using targeted mitoDsRed (Fig. **S3**). When immunocytochemistry was performed using an antibody for Hsp 60, which targets mitochondria, Q108 cells presented a slight decrease in the population of mitochondria (data not shown). This could indicate that activated autophagy in Q108 cells could be responsible for the decreased number of mitochondria. However, due to the small number of experiments performed and the decrease in PGC-1α, we cannot fully make a conclusion, since the possible decrease in mitochondrial number could be due to decreased biogenesis. In order to better evaluate this hypothesis, as it contradicts some studies found in the literature, more experiments should be performed. More specifically by testing a control using bafilomycin A, which inhibits autophagy by inhibiting autophagosome-lysosome fusion, could prove whether the decrease in LC3-II was indeed caused by activation of autophagic pathways. Fluorescent imaging of both LC3 autophagosomes and LC3-II punctate and evaluate the levels of beclin-1 could also help shed some light regarding this matter. Furthermore, PINK1/parkin pathway is not the only existing pathway capable of removing damaged mitochondria. In fact, over the years several others mitophagy-associated pathways have emerged that should be further explored in order to better understand their relation towards MJD.

Overall, data strongly suggest impairment in mitochondrial function and dynamics in models of MJD thus highlighting the role of mitochondrial dysfunction as a pathogenic mechanism of MJD. Nonetheless, other parameters regarding mitochondrial dysfunction could enhance the veracity of our findings such as mitochondrial motility and proper characterization of mitochondrial morphology. Besides mitochondrial dysfunction several other processes have been linked to the pathogenesis of MJD, such as formation of aggregates, transcriptional deregulation, impaired axonal transport, compromised neuronal signaling, protein degradation, RNA toxicity and formation of alternatively spliced transcripts; which are worth being

further explored. Nowadays many authors abide by the idea that an optimal therapeutic strategy for neurodegenerative disorders should be multi-target and since most diseases have more than one toxic mechanism it is vital to try to understand all of them. The more is known about the pathogenesis underlying a disease the better approaches could de proposed to efficiently target this fatal disease. Considering the dysfunctional features of mitochondria observed in our study, more selective therapeutic strategies could be applied, such as the use of antioxidants, preventing transcriptional deregulation, modulating autophagy and modulating calcium homeostasis.

References

Aidt, F. H., Marie, S., Nielsen, B., Kanters, J., Pesta, D., Nielsen, T. T., Nørremølle, A., Hasholt, L., Christiansen, M., and Hagen, C. M. (2013). Dysfunctional mitochondrial respiration in the striatum of the Huntington ' s disease transgenic R6 / 2 mouse model. 1–13.

Antony, P. M. A., Mäntele, S., Mollenkopf, P., Boy, J., Kehlenbach, R. H., Riess, O., and Schmidt, T. (2009). Identification and functional dissection of localization signals within ataxin-3. Neurobiol. Dis. *36*, 280–292.

Araujo, J., Breuer, P., Dieringer, S., Krauss, S., Dorn, S., Zimmermann, K., Pfeifer, A., Klockgether, T., Wuellner, U., and Evert, B. O. (2011). FOXO4-dependent upregulation of superoxide dismutase-2 in response to oxidative stress is impaired in spinocerebellar ataxia type 3. Hum. Mol. Genet. *20*, 2928–2941.

Atkinson, D. (1977). Cellular energy control. Tibs, 198–200.

Bauer, P. O., and Nukina, N. (2009). The pathogenic mechanisms of polyglutamine diseases and current therapeutic strategies. J. Neurochem. *110*, 1737–1765.

Berke, S. J. S., Chai, Y., Marrs, G. L., Wen, H., and Paulson, H. L. (2005). Defining the role of ubiquitin-interacting motifs in the polyglutamine disease protein, ataxin-3. J. Biol. Chem. *280*, 32026–32034.

Bettencourt, C., and Lima, M. (2011). Machado-Joseph Disease: from first descriptions to new perspectives. Orphanet J. Rare Dis. *6*, 35.

Bettencourt, C., Santos, C., Kay, T., Vasconcelos, J., and Lima, M. (2008). Analysis of segregation patterns in Machado-Joseph disease pedigrees. J. Hum. Genet. *53*, 920–923.

Bevivino, A. E., and Loll, P. J. (2001). An expanded glutamine repeat destabilizes native ataxin-3 structure and mediates formation of parallel ␣ -fibrils.

Bichelmeier, U. *et al.* (2007). Nuclear localization of ataxin-3 is required for the manifestation of symptoms in SCA3: in vivo evidence. J. Neurosci. *27*, 7418–7428.

Bjørkøy, G., Lamark, T., Brech, A., Outzen, H., Perander, M., Øvervatn, A., Stenmark, H., and Johansen, T. (2005). p62/SQSTM1 forms protein aggregates degraded by autophagy and has a protective effect on huntingtin-induced cell death. J. Cell Biol. *171*, 603–614.

Boeddrich, A. *et al.* (2006). An arginine/lysine-rich motif is crucial for VCP/p97-mediated modulation of ataxin-3 fibrillogenesis. EMBO J. *25*, 1547–1558.

Burnett, B. G., and Pittman, R. N. (2005). The polyglutamine neurodegenerative protein ataxin 3 regulates aggresome formation. Proc. Natl. Acad. Sci. U. S. A. *102*, 4330–4335.

Burnett, B., Li, F., and Pittman, R. N. (2003). The polyglutamine neurodegenerative protein ataxin-3 binds polyubiquitylated proteins and has ubiquitin protease activity. Hum. Mol. Genet. *12*, 3195–3205.

Chai, Y., Koppenhafer, S. L., Shoesmith, S. J., Perez, M. K., and Paulson, H. L. (1999). Evidence for proteasome involvement in polyglutamine disease: localization to nuclear inclusions in SCA3/MJD and suppression of polyglutamine aggregation in vitro. Hum. Mol. Genet. *8*, 673–682.

Chai, Y., Shao, J., Miller, V. M., Williams, A., and Paulson, H. L. (2002). Live-cell imaging reveals divergent intracellular dynamics of polyglutamine disease proteins and supports a sequestration model of pathogenesis. Proc. Natl. Acad. Sci. U. S. A. *99*, 9310–9315.

Chen, H., and Chan, D. C. (2004). Mitochondrial Dynamics in Mammals. Curr. Top. Dev. Biol. *59*, 119–144.

Chen, X., Tang, T., Tu, H., Nelson, O., Pook, M., and R (2008). Deranged calcium signaling and neurodegeneration in spinocerebellar ataxia type 3. J. *28*, 12713–12724.

Chen, Y., and Dorn II, G. W. (2013). PINK1- Phosphorylated Mitofusin 2 is a Parkin Receptor for Culling Damaged Mitochondria. *340*, 471–475.

Chou, A. H., Chen, C. Y., Chen, S. Y., Chen, W. J., Chen, Y. L., Weng, Y. S., and Wang, H. L. (2008). Polyglutamine-expanded ataxin-7 causes cerebellar dysfunction by inducing transcriptional dysregulation. Neurochem. Int. *56*, 329–339.

Chou, A. H., Lin, A. C., Hong, K. Y., Hu, S. H., Chen, Y. L., Chen, J. Y., and Wang, H. L. (2011). P53 activation mediates polyglutamine-expanded ataxin-3 upregulation of Bax expression in cerebellar and pontine nuclei neurons. Neurochem. Int. *58*, 145–152.

Chou, A. H., Yeh, T. H., Kuo, Y. L., Kao, Y. C., Jou, M. J., Hsu, C. Y., Tsai, S. R., Kakizuka, A., and Wang, H. L. (2006). Polyglutamine-expanded ataxin-3 activates mitochondrial apoptotic pathway by upregulating Bax and downregulating Bcl-xL. Neurobiol. Dis. *21*, 333–345.

Codogno, P., Mehrpour, M., and Proikas-Cezanne, T. (2012). Canonical and non-canonical autophagy: variations on a common theme of self-eating? Nat. Rev. Mol. Cell Biol. *13*, 7–12.

Costa, M. do C., Bajanca, F., Rodrigues, A. J., Tomé, R. J., Corthals, G., Macedo-Ribeiro, S., Paulson, H. L., Logarinho, E., and Maciel, P. (2010). Ataxin-3 plays a role in mouse myogenic differentiation through regulation of integrin subunit levels. PLoS One *5*.

Costa, M. do C., and Paulson, H. L. (2012). Toward understanding Machado-Joseph disease. Prog. Neurobiol. *97*, 239–257.

Coutinho, P., and Andrade, C. (1978). Autosomal dominant system degeneration in Portuguese families of the Azores Islands: A new genetic disorder involving cerebellar, pyramidal, extrapyramidal and spinal cord motor functions. Neurology *28*, 703–709.

Cui, L., Jeong, H., Borovecki, F., Parkhurst, C. N., Tanese, N., and Krainc, D. (2006). Transcriptional Repression of PGC-1α by Mutant Huntingtin Leads to Mitochondrial Dysfunction and Neurodegeneration. Cell *127*, 59–69.

Cummings, C. J., and Zoghbi, H. Y. (2000). Trinucleotide Repeats : Mechanisms and Pathophysiology. 281–328.

Dantuma, N. P., Heinen, C., and Hoogstraten, D. (2009). The ubiquitin receptor Rad23: At the crossroads of nucleotide excision repair and proteasomal degradation. DNA Repair (Amst). *8*, 449–460.

Donaldson, K. M., Li, W., Ching, K. A., Batalov, S., Tsai, C.-C., and Joazeiro, C. A. P. (2003). Ubiquitin-mediated sequestration of normal cellular proteins into polyglutamine aggregates. Proc. Natl. Acad. Sci. U. S. A. *100*, 8892–8897.

Durcan, T. M., Kontogiannea, M., Thorarinsdottir, T., Fallon, L., Williams, A. J., Djarmati, A., Fantaneanu, T., Paulson, H. L., and Fon, E. A. (2011). The machado-joseph disease-associated mutant form of ataxin-3 regulates parkin ubiquitination and stability. Hum. Mol. Genet. *20*, 141–154.

Dürr, A. *et al.* (1996). Spinocerebellar ataxia 3 and Machado-Joseph disease: Clinical, molecular, and neuropathological features. Ann. Neurol. *39*, 490–499.

Ellisdon, A. M., Thomas, B., and Bottomley, S. P. (2006). The two-stage pathway of ataxin-3 fibrillogenesis involves a polyglutamine-independent step. J. Biol. Chem. *281*, 16888–16896.

Evert, B. O., Araujo, J., Vieira-saecker, A. M., Vos, R. A. I. De, Harendza, S., Klockgether, T., and Wu, U. (2006). Ataxin-3 Represses Transcription via Chromatin Binding , Interaction with Histone Deacetylase 3 , and Histone Deacetylation. Neurobiol. Dis. *26*, 11474–11486.

Evert, B. O., Vogt, I. R., Kindermann, C., Ozimek, L., de Vos, R. a, Brunt, E. R., Schmitt, I., Klockgether, T., and Wüllner, U. (2001). Inflammatory genes are upregulated in expanded ataxin-3-expressing cell lines and spinocerebellar ataxia type 3 brains. J. Neurosci. *21*, 5389–5396.

Evert, B., Vogt, I., Vieira-Saecker, A., Ozimek, L., de Vos, R., Brunt, E., Klockgether, T., and Wüllner, U. (2003). Gene Expression Profiling in Ataxin-3 Expressing Cell Lines Reveals Distinct Effects of Normal and Mutant Ataxin-3. J. Neuropathol. Exp. Neurol. *62*, 1006–1018.

Fei, E., Jia, N., Zhang, T., Ma, X., Wang, H., Liu, C., Zhang, W., Ding, L., Nukina, N., and Wang, G. (2007). Phosphorylation of ataxin-3 by glycogen synthase kinase 3β at serine 256 regulates the aggregation of ataxin-3. Biochem. Biophys. Res. Commun. *357*, 487–492.

Ferro, A. *et al.* (2007). NEDD8: A new ataxin-3 interactor. Biochim. Biophys. Acta - Mol. Cell Res. *1773*, 1619–1627.

Frank, S., Gaume, B., Bergmann-leitner, E. S., Leitner, W. W., Robert, E. G., Smith, C. L., and Youle, R. J. (2001). The Role of Dynamin-Related Protein 1 , a Mediator of Mitochondrial Fission , in Apoptosis. Dev. Cell *1*, 515–525.

Fu, Y. H., Kuhl, D. P., Pizzuti, A., Pieretti, M., Sutcliffe, J. S., Richards, S., Verkerk, A. J., Holden, J. J., Fenwick, R. G., and Warren, S. T. (1991). Variation of the CGG repeat at the fragile X site results in genetic instability: resolution of the Sherman paradox. Cell *67*, 1047–1058.

Gales, L., Cortes, L., Almeida, C., Melo, C. V., Costa, M. D. C., Maciel, P., Clarke, D. T., Damas, A. M., and Macedo-Ribeiro, S. (2005). Towards a structural understanding of the fibrillization pathway in Machado-Joseph's disease: Trapping early oligomers of non-expanded ataxin-3. J. Mol. Biol. *353*, 642–654.

Gatchel, J. R., and Zoghbi, H. Y. (2005). Diseases of unstable repeat expansion: mechanisms and common principles. Nat. Rev. Genet. *6*, 743–755.

Geisler, S., Holmström, K. M., Skujat, D., Fiesel, F. C., Rothfuss, O. C., Kahle, P. J., and

Springer, W. (2010). PINK1/Parkin-mediated mitophagy is dependent on VDAC1 and p62/SQSTM1. Nat. Cell Biol. *12*, 119–131.

Haacke, A., Broadley, S. A., Boteva, R., Tzvetkov, N., Hartl, F. U., and Breuer, P. (2006). Proteolytic cleavage of polyglutamine-expanded ataxin-3 is critical for aggregation and sequestration of non-expanded ataxin-3. Hum. Mol. Genet. *15*, 555–568.

Haberhausen, G., Damian, M. S., Leweke, F., and M??ller, U. (1995). Spinocerebellar ataxia, type 3 (SCA3) is genetically identical to Machado-Joseph disease (MJD). J. Neurol. Sci. *132*, 71–75.

Hamilton, J., Pellman, J. J., Brustovetsky, T., Harris, R. A., and Brustovetsky, N. (2015). Oxidative metabolism in YAC128 mouse model of Huntington ' s disease. 1–47.

Heir, R., Ablasou, C., Dumontier, E., Elliott, M., Fagotto-Kaufmann, C., and Bedford, F. K. (2006). The UBL domain of PLIC-1 regulates aggresome formation. EMBO Rep. *7*, 1252–1258.

Herbert, A. D., Carr, A. M., Hoffmann, E., and Lichten, M. (2014). FindFoci: A focus detection algorithm with automated parameter training that closely matches human assignments, reduces human inconsistencies and increases speed of analysis. PLoS One *9*, 1–33.

Holmström, K. M., and Finkel, T. (2014). Cellular mechanisms and physiological consequences of redox-dependent signalling. Nat. Rev. Mol. Cell Biol. *15*, 411–421.

Horimoto, Y. *et al.* (2011). Longitudinal study on MRI intensity changes of Machado-Joseph disease: Correlation between MRI findings and neuropathological changes. J. Neurol. *258*, 1657–1664.

Hroudová, J., Singh, N., and Fisar, Z. (2014). Mitochondrial dysfunctions in neurodegenerative diseases: Relevance to alzheimer's disease. Biomed Res. Int. *2014*.

Ikeda, H., Yamaguchi, M., Sugai, S., Aze, Y., Narumiya, S., and Kakizuka, A. (1996). Expanded polyglutamine in the Machado-Joseph disease protein induces cell death in vitro and in vivo. Nat. Genet. *13*, 196–202.

Ishihara, N., Eura, Y., and Mihara, K. (2004). Mitofusin 1 and 2 play distinct roles in mitochondrial fusion reactions via GTPase activity. J. Cell Sci. *117*, 6535–6546.

Ishihara, N., Fujita, Y., Oka, T., and Mihara, K. (2006). Regulation of mitochondrial morphology through proteolytic cleavage of OPA1. EMBO J. *25*, 2966–2977.

Jastroch, M., Divakaruni, A. S., Mookerjee, S., Treberg, J. R., and Martin, D. (2011). Mitochondrial proton and electron leaks. 53–67.

Jeub, M., Herbst, M., Spauschus, A., Fleischer, H., Klockgether, T., Wuellner, U., and Evert, B. O. (2006). Potassium channel dysfunction and depolarized resting membrane potential in a cell model of SCA3. Exp. Neurol. *201*, 182–192.

Jin, S. M., Lazarou, M., Wang, C., Kane, L. A., Narendra, D. P., and Youle, R. J. (2010). Mitochondrial membrane potential regulates PINK1 import and proteolytic destabilization by PARL. J. Cell Biol. *191*, 933–942.

Kaufman, B., Durisic, N., Mativetsky, J., Constantino, S., Hancock, M., Grutter, P., and Shoubridge, E. (2007). The Mitochondrial Transcription Factor TFAM Coordinates the Assembly of Multiple DNA Molecules into Nucleoid-like Structures. Mol. Biol. Cell *18*, 3225–3236.

Kawaguchi, Y. *et al.* (1994). CAG expansions in a novel gene for Machado-Joseph Disease at chromosome 14q32.1. Nat. Genet. *8*, 221–228.

Kawai, Y., Takeda, A., Abe, Y., Washimi, Y., Tanaka, F., and Sobue, G. (2004). Cognitive impairments in Machado-Joseph disease. Arch Neurol *61*, 1757–1760.

Kazachkova, N., Raposo, M., Montiel, R., Cymbron, T., Bettencourt, C., Silva-Fernandes, A., Silva, S., MacIel, P., and Lima, M. (2013). Patterns of mitochondrial DNA damage in blood and brain tissues of a transgenic mouse model of machado-joseph disease. Neurodegener. Dis. *11*, 206–214.

Kim, J., Moody, J. P., Edgerly, C. K., Bordiuk, O. L., Cormier, K., Smith, K., Flint Beal, M., and Ferrante, R. J. (2010). Mitochondrial loss, dysfunction and altered dynamics in Huntington's disease. Hum. Mol. Genet. *19*, 3919–3935.

Klionsky, D. J. *et al.* (2012). Guidelines for the use and interpretation of assays for monitoring autophagy. Autophagy *8*, 445–544.

Klockgether, T. *et al.* (1998). Autosomal dominant cerebellar ataxia type I. MRI-based volumetry of posterior fossa structures and basal ganglia in spinocerebellar ataxia types 1, 2 and 3. Brain *121*, 1687–1693.

Korshunov, S. S., Skulachev, V. P., and Starkov, A. A. (1997). High protonic potential actuates a mechanism of production of reactive oxygen species in mitochondria. FEBS Lett. *416*, 15–18.

Koshiba, T. (2004). Structural Basis of Mitochondrial Tethering by Mitofusin Complexes.

Science (80-.). *305*, 858–862.

Laço, M. N., Cortes, L., Travis, S. M., Paulson, H. L., and Rego, A. C. (2012a). Valosin-Containing Protein (VCP/p97) Is an Activator of Wild-Type Ataxin-3. PLoS One *7*, 1–13.

Laço, M. N., Oliveira, C. R., Paulson, H. L., and Rego, A. C. (2012b). Compromised mitochondrial complex II in models of Machado-Joseph disease. Biochim. Biophys. Acta - Mol. Basis Dis. *1822*, 139–149.

Li, F., Macfarlan, T., Pittman, R. N., and Chakravarti, D. (2002). Ataxin-3 is a histone-binding protein with two independent transcriptional corepressor activities. J. Biol. Chem. *277*, 45004–45012.

Li, S. H., and Li, X. J. (2004). Huntingtin-protein interactions and the pathogenesis of Huntington's disease. Trends Genet. *20*, 146–154.

Lima, L., and Coutinho, P. (1980). Clinical criteria for diagnosis of Machado–Joseph disease: report of a non-Azorena Portuguese family. Neurology *30*, 319–322.

Lin, X., Li, S., Zhao, Y., Ma, X., Zhang, K., He, X., and Wang, Z. (2013). Interaction domains of p62: a bridge between p62 and selective autophagy. DNA Cell Biol. *32*, 220–227.

Macedo-Ribeiro, S., Cortes, L., Maciel, P., and Carvalho, A. L. (2009). Nucleocytoplasmic shuttling activity of ataxin-3. PLoS One *4*.

Maciel, P., Costa, M. C., Ferro, A., Rousseau, M., Santos, C. S., Gaspar, C., Barros, J., Rouleau, G. a, Coutinho, P., and Sequeiros, J. (2001). Improvement in the molecular diagnosis of Machado-Joseph disease. Arch. Neurol. *58*, 1821–1827.

Maciel, P., Gaspar, C., DeStefano, A. L., Silveira, I., Coutinho, P., Radvany, J., Dawson, D. M., Sudarsky, L., Guimarães, J., and Loureiro, J. E. (1995). Correlation between CAG repeat length and clinical features in Machado-Joseph disease. Am. J. Hum. Genet. *57*, 54–61.

Mäkelä, J. *et al.* (2015). Peroxisome proliferator-activated receptor-γ coactivator-1α (PGC-1α) mediates neuroprotection against excitotoxic brain injury in transgenic mice - role of mitochondria and X-linked inhibitor of apoptosis protein. Eur. J. Neurosci., n/a – n/a.

Masino, L., Nicastro, G., De Simone, A., Calder, L., Molloy, J., and Pastore, A. (2011). The Josephin domain determines the morphological and mechanical properties of ataxin-3 fibrils. Biophys. J. *100*, 2033–2042.

Matos, C. A., de Macedo-Ribeiro, S., and Carvalho, A. L. (2011). Polyglutamine diseases: The special case of ataxin-3 and Machado-Joseph disease. Prog. Neurobiol. *95*, 26–48.

Mazzucchelli, S. *et al.* (2009). Proteomic and biochemical analyses unveil tight interaction of ataxin-3 with tubulin. Int. J. Biochem. Cell Biol. *41*, 2485–2492.

McCampbell, a *et al.* (2000). CREB-binding protein sequestration by expanded polyglutamine. Hum. Mol. Genet. *9*, 2197–2202.

Mears, J. a, Lackner, L. L., Fang, S., Ingerman, E., Nunnari, J., and Hinshaw, J. E. (2011). Conformational changes in Dnm1 support a contractile mechanism for mitochondrial fission. Nat. Struct. Mol. Biol. *18*, 20–26.

Mueller, T., Breuer, P., Schmitt, I., Walter, J., Evert, B. O., and Wüllner, U. (2009). CK2-dependent phosphorylation determines cellular localization and stability of ataxin-3. Hum. Mol. Genet. *18*, 3334–3343.

Murphy, M. P. (2009). How mitochondria produce reactive oxygen species. Biochem. J. *417*, 1–13.

Nakano, K. K., Dawson, D. M., and Spence, A. (1972). Machado disease. A hereditary ataxia in Portuguese emigrants to Massachusetts. Neurology *22*, 49–55.

Nascimento-Ferreira, I. *et al.* (2011). Overexpression of the autophagic beclin-1 protein clears mutant ataxin-3 and alleviates Machado-Joseph disease. Brain *134*, 1400–1415.

Natalello, A., Frana, A. M., Relini, A., Apicella, A., Invernizzi, G., Casari, C., Gliozzi, A., Doglia, S. M., Tortora, P., and Regonesi, M. E. (2011). A major role for side-chain polyglutamine hydrogen bonding in irreversible ataxin-3 aggregation. PLoS One *6*.

Nicastro, G., Menon, R. P., Masino, L., Knowles, P. P., McDonald, N. Q., and Pastore, A. (2005). The solution structure of the Josephin domain of ataxin-3: structural determinants for molecular recognition. Proc. Natl. Acad. Sci. U. S. A. *102*, 10493–10498.

Nicholls, D. G., and Ward, M. W. (2000). Mitochondrial membrane potential and neuronal glutamate excitotoxicity: Mortality and millivolts. Trends Neurosci. *23*, 166–174.

Oettinghaus, B., D'Alonzo, D., Barbieri, E., Restelli, L. M., Savoia, C., Licci, M., Tolnay, M., Frank, S., and Scorrano, L. (2016). DRP1-dependent apoptotic mitochondrial fission occurs independently of BAX, BAK and APAF1 to amplify cell death by BID and

oxidative stress. Biochim. Biophys. Acta - Bioenerg., 1–10.

Oliveira, J. M. A., Chen, S., Almeida, S., Riley, R., Gonçalves, J., Oliveira, C. R., Hayden, M. R., Nicholls, D. G., Ellerby, L. M., and Rego, A. C. (2006). Mitochondrial-dependent Ca2+ handling in Huntington's disease striatal cells: effect of histone deacetylase inhibitors. J. Neurosci. *26*, 11174–11186.

Pankiv, S., Clausen, T. H., Lamark, T., Brech, A., Bruun, J. A., Outzen, H., ??vervatn, A., Bjørkøy, G., and Johansen, T. (2007). p62/SQSTM1 binds directly to Atg8/LC3 to facilitate degradation of ubiquitinated protein aggregates by autophagy*[S]. J. Biol. Chem. *282*, 24131–24145.

Paulson, H. (2013). Machado-Joseph Disease/Spinocerebellar Ataxia Type 3. 437–449.

Paulson, H. L. (1999). Protein fate in neurodegenerative proteinopathies: polyglutamine diseases join the (mis)fold. Am. J. Hum. Genet. *64*, 339–345.

Paulson, H. L. (2007). Dominantly inherited ataxias: Lessons learned from Machado-Joseph disease/spinocerebellar ataxia type 3. Semin. Neurol. *27*, 133–142.

Paulson, H. L., Das, S. S., Crino, P. B., Perez, M. K., Patel, S. C., Gotsdiner, D., Fischbeck, K. H., and Pittman, R. N. (1997a). Machado-Joseph disease gene product is a cytoplasmic protein widely expressed in brain. Ann. Neurol. *41*, 453–462.

Paulson, H. L., Perez, M. K., Trottier, Y., Trojanowski, J. Q., Subramony, S. H., Das, S. S., Vig, P., Mandel, J., Fischbeck, K. H., and Pittman, R. N. (1997b). Intranuclear Inclusions of Expanded Polyglutamine Protein in Spinocerebellar Ataxia Type 3. Cell *19*, 333–344.

Paulson, H. L., and Pittman, R. N. (1998). Recruitment and the Role of Nuclear Localization in Polyglutamine-mediated Aggregation. J. Cell Biol. *143*, 1457–1470.

Pellman, J. J., Hamilton, J., Brustovetsky, T., and Brustovetsky, N. (2015). Ca2+ handling in isolated brain mitochondria and cultured neurons derived from the YAC128 mouse model of Huntington's disease. J. Neurochem. *134*, 652–667.

Perry, S. W., Norman, J. P., Barbieri, J., Brown, E. B., and Harris, A. (2011). Mitochondrial membrane potential probes and the proton gradient : a Practical Usage Guide. Biotechniques *50*, 98–115.

Pittman, N., Dibenedetto, J., and Mills, J. C. (1993). Cellular A System for Characterizing Neuronal Cell Death Programmed Molecular. *73*.

Ranum, L. P., Lundgren, J. K., Schut, L. J., Ahrens, M. J., Perlman, S., Aita, J., Bird, T. D.,

Gomez, C., and Orr, H. T. (1995). Spinocerebellar ataxia type 1 and Machado-Joseph disease: incidence of CAG expansions among adult-onset ataxia patients from 311 families with dominant, recessive, or sporadic ataxia. Am. J. Hum. Genet. *57*, 603–608.

Reina, C. P., Zhong, X., and Pittman, R. N. (2009). Proteotoxic stress increases nuclear localization of ataxin-3. Hum. Mol. Genet. *19*, 235–249.

Rich, P. R., and Marechal, A. (2010). The mitochondrial respiratory chain. Essays Biochem. *47*, 1–24.

Riess, O., Rüb, U., Pastore, A., Bauer, P., and Schöls, L. (2008). SCA3: neurological features, pathogenesis and animal models. Cerebellum *7*, 125–137.

Rodrigues, A. J., do Carmo Costa, M., Silva, T. L., Ferreira, D., Bajanca, F., Logarinho, E., and Maciel, P. (2010). Absence of ataxin-3 leads to cytoskeletal disorganization and increased cell death. Biochim. Biophys. Acta - Mol. Cell Res. *1803*, 1154–1163.

Rodríguez-Lebrón, E., Costa, M. doCarmo, Luna-Cancalon, K., Peron, T. M., Fischer, S., Boudreau, R. L., Davidson, B. L., and Paulson, H. L. (2013). Silencing mutant ATXN3 expression resolves molecular phenotypes in SCA3 transgenic mice. Mol. Ther. *21*, 1909–1918.

Rogers, G. W., Brand, M. D., Petrosyan, S., Ashok, D., Elorza, A. A., Ferrick, D. A., and Murphy, A. N. (2011). High throughput microplate respiratory measurements using minimal quantities of isolated mitochondria. PLoS One *6*.

Romanul, F. C., Fowler, H. L., Radvany, J., Feldman, R. G., and Feingold, M. (1977). Azorean disease of the nervous system. N. Engl. J. Med. *296*, 1505–1508.

Rosenberg, R. N., Nyhan, W. L., Bay, C., and Shore, P. (1976). Autosomal dominant striatonigral degeneration: A clinical, pathologic, and biochemical study of a new genetic disorder. Neurology *26*, 703–714.

Ross, C. A. (1995). When more is less: Pathogenesis of glutamine repeat neurodegenerative diseases. Neuron *15*, 493–496.

Rüb, U., Brunt, E., and Deller, T. (2008). New insights into the pathoanatomy of spinocerebellar ataxia type 3 (Machado-Joseph disease). Curr Opin Neurol *21*, 111–116.

Rüb, U., de Vos, R. A. I., Schultz, C., Brunt, E. R., Paulson, H., and Braak, H. (2002). Spinocerebellar ataxia type 3 (Machado-Joseph Disease): severe destruction of the

lateral reticular nucleus. Brain *125*, 2115–2124.

Rusten, T. E., and Stenmark, H. (2010). P62, an Autophagy Hero or Culprit? Nat. Cell Biol. *12*, 207–209.

Sakai, T., and Kawakami, H. (1996). Machado-Joseph disease: A proposal of spastic paraplegic subtype. Neurology *46*, 846–847.

Schmidt, T. *et al.* (1998). An isoform of ataxin-3 accumulates in the nucleus of neuronal cells in affected brain regions of SCA3 patients. Brain Pathol. *8*, 669–679.

Schöls, L., Bauer, P., Schmidt, T., Schulte, T., and Riess, O. (2004). Autosomal dominant cerebellar ataxias: Clinical features, genetics, and pathogenesis. Lancet Neurol. *3*, 291–304.

Scorrano, L., Ashiya, M., Buttle, K., Weiler, S., Oakes, S. A., Mannella, C. A., and Korsmeyer, S. J. (2002). A Distinct Pathway Remodels Mitochondrial Cristae and Mobilizes Cytochrome c during Apoptosis. Dev. Cell *2*, 55–67.

Shao, J., and Diamond, M. I. (2007). Polyglutamine diseases: Emerging concepts in pathogenesis and therapy. Hum. Mol. Genet. *16*, 115–123.

Shiba-Fukushima, K., Imai, Y., Yoshida, S., Ishihama, Y., Kanao, T., Sato, S., and Hattori, N. (2012). PINK1-mediated phosphorylation of the Parkin ubiquitin-like domain primes mitochondrial translocation of Parkin and regulates mitophagy. Sci. Rep. *2*, 1002.

Shimohata, T. *et al.* (2000). Expanded polyglutamine stretches interact with TAFII130, interfering with CREB-dependent transcription. Nat. Genet. *26*, 29–36.

Silva-Fernandes, A., Duarte-Silva, S., Neves-Carvalho, A., Amorim, M., Soares-Cunha, C., Oliveira, P., Thirstrup, K., Teixeira-Castro, A., and Maciel, P. (2014). Chronic Treatment with 17-DMAG Improves Balance and Coordination in A New Mouse Model of Machado-Joseph Disease. Neurotherapeutics *11*, 433–449.

Song, A. X., Zhou, C. J., Peng, Y., Gao, X. C., Zhou, Z. R., Fu, Q. S., Hong, J., Lin, D. H., and Hu, H. Y. (2010). Structural transformation of the tandem ubiquitin-interacting motifs in ataxin-3 and their cooperative interactions with ubiquitin chains. PLoS One *5*.

La Spada, A., Wilson, E., Lubahn, D., Harding, A. E., and Fischbeck, K. (1991). Androgen receptor gene mutations in X-linked spinal and bulbar muscular atrophy. Nature *352*, 77–79.

Stocchi, V., Cucchiarini, L., Magnani, M., Chiarantini, L., Palma, P., and Crescentini, G.

(1985). Simultaneous extraction and reverse-phase high-performance liquid chromatographic determination of adenine and pyridine nucleotides in human red blood cells. Anal. Biochem. *146*, 118–124.

St-Pierre, J. *et al.* (2006). Suppression of Reactive Oxygen Species and Neurodegeneration by the PGC-1 Transcriptional Coactivators. Cell *127*, 397–408.

Su, B., Wang, X., Zheng, L., Perry, G., Smith, M. A., and Zhu, X. (2010). Abnormal Mitochondrial Dynamics and Neurodegenerative Diseases. *1802*, 135–142.

Tait, D., Riccio, M., Sittler, A., Scherzinger, E., Santi, S., Ognibene, A., Maraldi, N. M., Lehrach, H., and Wanker, E. E. (1998). Ataxin-3 is transported into the nucleus and associates with the nuclear matrix. Hum. Mol. Genet. *7*, 991–997.

Takiyama, Y., Nishizawa, M., Tanaka, H., Kawashima, S., Sakamoto, H., Karube, Y., Shimazaki, H., Soutome, M., Endo, K., and Ohta, S. (1993). The gene for Machado-Joseph disease maps to human chromosome 14q. Nat. Genet. *4*, 300–304.

Tanida, I., Ueno, T., and Kominami, E. (2008). LC3 and autophagy. Methods Mol. Biol. *445*, 77–88.

Todd, P. K., and Paulson, H. L. (2010). RNA-mediated neurodegeneration in repeat expansion disorders. Ann. Neurol. *67*, 291–300.

Trottier, Y., Cancel, G., An-Gourfinkel, I., Lutz, Y., Weber, C., Brice, A., Hirsch, E., and Mandel, J. L. (1998). Heterogeneous intracellular localization and expression of ataxin-3. Neurobiol. Dis. *5*, 335–347.

Wang, G., Sawai, N., Kotliarova, S., Kanazawa, I., and Nukina, N. (2000). Ataxin-3, the MJD1 gene product, interacts with the two human homologs of yeast DNA repair protein RAD23, HHR23A and HHR23B. Hum. Mol. Genet. *9*, 1795–1803.

Wang, W., Wang, X., Fujioka, H., Hoppel, C., Whone, A. L., Caldwell, M. A., Cullen, P. J., Liu, J., and Zhu, X. (2015). Parkinson's disease-associated mutant VPS35 causes mitochondrial dysfunction by recycling DLP1 complexes. Nat. Med. *22*, 54–63.

Wang, X., Leverin, A. L., Han, W., Zhu, C., Johansson, B. R., Jacotot, E., Ten, V. S., Sims, N. R., and Hagberg, H. (2011). Isolation of brain mitochondria from neonatal mice. J. Neurochem. *119*, 1253–1261.

Wilkinson, K. D. (1997). Regulation of ubiquitin-dependent processes by deubiquitinating enzymes. FASEB J. *11*, 1245–1256.

Winborn, B. J., Travis, S. M., Todi, S. V., Scaglione, K. M., Xu, P., Williams, A. J., Cohen, R.

E., Peng, J., and Paulson, H. L. (2008). The deubiquitinating enzyme ataxin-3, a polyglutamine disease protein, edits Lys63 linkages in mixed linkage ubiquitin chains. J. Biol. Chem. *283*, 26436–26443.

Woods, B. T., and Schaumburg, H. H. (1972). Nigro-spino-dentatal degeneration with nuclear ophthalmoplegia. A unique and partially treatable clinico-pathological entity. J. Neurol. Sci. *17*, 149–166.

Yu, Y.-C., Kuo, C.-L., Cheng, W.-L., Liu, C.-S., and Hsieh, M. (2009). Decreased antioxidant enzyme activity and increased mitochondrial DNA damage in cellular models of Machado-Joseph disease. J. Neurosci. Res. *87*, 1884–1891.

Zhong, X., and Pittman, R. N. (2006). Ataxin-3 binds VCP/p97 and regulates retrotranslocation of ERAD substrates. Hum. Mol. Genet. *15*, 2409–2420.

Zoghbi, H. Y., and Orr, H. T. (2000). G Lutamine R Epeats and. Annu. Rev. Neurosci. *23*, 217–247.

Attachments

1. Supplementary Methods

1.1.1. Macros used to design the Region of Interest (ROI)

```
/*
   MitProt_AutoROIsupervised is an ImageJ macro developed to design ROIS of neurons to be used
to analyze mitochondria, protein levels and colocalization with MitoProt_analyzer
Copyright (C) 2014  Jorge Valero Gómez-Lobo.

MitProt_AutoROIsupervised is free software: you can redistribute it and/or modify
it under the terms of the GNU General Public License as published by
the Free Software Foundation, either version 3 of the License, or
   (at your option) any later version.

   MitProt_AutoROIsupervised is distributed in the hope that it will be useful,
but WITHOUT ANY WARRANTY; without even the implied warranty of
   MERCHANTABILITY or FITNESS FOR A PARTICULAR PURPOSE.  See the
   GNU General Public License for more details.

   You should have received a copy of the GNU General Public License
along with this program.  If not, see <http://www.gnu.org/licenses/>.
*/

//This macro has been developed by Dr Jorge Valero (jorge.valero@cnc.uc.pt).
//If you have any doubt about how to use it, please contact me.

//License
Dialog.create("GNU GPL License");
Dialog.addMessage(" MitProt_AutoROIsupervised  Copyright (C) 2014 Jorge Valero Gomez-Lobo.");
Dialog.setInsets(10, 20, 0);
Dialog.addMessage(" MitProt_AutoROIsupervised  comes with ABSOLUTELY NO WARRANTY; click on help button for details.");
Dialog.setInsets(0, 20, 0);
Dialog.addMessage("This is free software, and you are welcome to redistribute it under certain conditions; click on help button for details.");
Dialog.addHelp("http://www.gnu.org/licenses/gpl.html");
Dialog.show();


// This macro helps on ROI design and storage for posterior analysis

//Select initial folder

dir=getDirectory("Please, select the initial folder");
```

```
if (File.exists(dir+"ROIS/")==false) File.makeDirectory(dir+"ROIS");
	dirRois=dir+"ROIS"+File.separator;
if (File.exists(dir+"Processed/")==false) File.makeDirectory(dir+"Processed");
	dirPro=dir+"Processed"+File.separator;
if (File.exists(dir+"NONProcessed/")==false) File.makeDirectory(dir+"NONProcessed");
	dirNONPro=dir+"NONProcessed"+File.separator;

//detect Images folder
level1=getFileList(dir);
i=0;
while (i<level1.length) {
	if (level1[i]=="Images/") imagedir=dir+level1[i];
	i++;
}
	//error message if no Images folder exists
	if (i==level1.length+1){
		showMessage("NO Images folder found");
		beep();
		exit();
	}

	//detect n folder
	level2=getFileList(imagedir);
	for (i=0; i<level2.length; i++) {
		ene=File.getName(imagedir+level2[i]);
		enesem=substring(ene, 1);
		if (endsWith(level2[i], "/")){
			direne=imagedir+level2[i];

			//detect group folder
			level3=getFileList(direne);
			for (ii=0; ii<level3.length; ii++){
				group=File.getName(direne+level3[ii]);
				diris=newArray(ene, group);
				if (File.exists(dirRois+ene+"/"+group+"/")==false)
creardir(dirRois, diris);
				dirRoisgroup=dirRois+ene+"/"+group+"/";
				if (File.exists(dirPro+ene+"/"+group+"/")==false)
creardir(dirPro, diris);
				dirProgroup=dirPro+ene+"/"+group+"/";
				if (endsWith(level3[ii], "/")){
					dirgroup=direne+level3[ii];

					//detect images
					level4=getFileList(dirgroup);
					for (iii=0; iii<level4.length; iii++){
						imagepath=dirgroup+level4[iii];
```

```
                                                work();
                                        }
                                }
                        }
                }
        }
}


function work(){
        //Open image
        run("Bio-Formats Importer", "open=["+imagepath+"] color_mode=Default
open_files view=Hyperstack stack_order=XYCZT");

        //get image name
        imopen=getTitle();
        imagename=File.name;
        raiz=File.nameWithoutExtension;

        // ROIs design
        cont=false;
        skip=false;
        while (cont==false){

                autoroi();
                rois=roiManager("count");
                if (rois==0) {
                        waitForUser("NO ROIS DETECTED");
                        skip=getBoolean("Do you want to skip this image?");
                        if (skip==true) cont=true;
                        else Roidesign();
                }
                else {
                        roiManager("Show All");
                        cont=getBoolean("Do you want to continue with the next
image?");
                        if (cont==false) {
                                roiManager("Deselect");
                                roiManager("Delete");
                                Dialog.create("OPTIONS");
                                Dialog.addChoice("Select an option:",
newArray("Separate cells using a line", "Design ROIs by myself", "Try to improve the
image"))
                                Dialog.show();
                                option=Dialog.getChoice();
                                if (option=="Separate cells using a line") Lineseparator();
                                if (option=="Design ROIs by myself") {
                                        Roidesign();
```

```
137                                         cont=true;
138                                         rois=0;
139                                     }
140                                     if (option=="Try to improve the image")
141 waitForUser("Now you have time to improve the image");
142                                 }
143                         }
144                 }
145                 if (skip==true) {
146                         if (File.exists(dirNONPro+ene+"/"+group+"/")==false)
147 creardir(dirNONPro, diris);
148                         dirNONProgroup=dirNONPro+ene+"/"+group+"/";
149                         File.rename(imagepath, dirNONProgroup+imagename);
150                         selectWindow(imopen);
151                         close();
152                 }
153                 if (skip==false && rois>0){
154                         roiManager("Save", dirRoisgroup+raiz+".zip");
155                         roiManager("Deselect");
156                         roiManager("Delete");
157                         File.rename(imagepath, dirProgroup+imagename);
158                         selectWindow(imopen);
159                         close();
160                 }
161
162
163
164
165 }
166 // this function creates folders
167 function creardir(inidir, pathes){
168         for (i=0; i<pathes.length; i++){
169                 File.makeDirectory(inidir+pathes[i]);
170                 inidir=inidir+pathes[i]+"/";
171         }
172
173 }
174 //automatic detection of cells
175 function autoroi(){
176         selectWindow(imopen);
177         run("Channels Tool...");
178         run("Make Composite", "display=Composite");
179         Stack.setDisplayMode("composite");
180         Stack.setActiveChannels("11");
181         run("Stack to RGB");
182         run("8-bit");
183         run("Median...", "radius=5");
```

```
184             setAutoThreshold("Triangle dark");
185             run("Analyze Particles...", "size=150-Infinity add");
186             close();
187             roiManager("Select",0);
188     }
189
190     function Roidesign(){
191             cont=false;
192             skip=false;
193             while (cont==false){
194                     setTool("polygon");
195                     waitForUser("Please, draw ROIs and add to ROI Manager by pressing t");
196                     rois=roiManager("count");
197                     if (rois==0) {
198                             waitForUser("NO ROIS DESIGNED");
199                             skip=getBoolean("Do you want to skip this image?");
200                             if (skip==true) cont=true;
201                     }
202                     else {
203                             roiManager("Show All");
204                             cont=getBoolean("Do you want to continue with the next step?")
205             }
206             }
207             if (skip==true) {
208                     if (File.exists(dirNONPro+ene+"/"+group+"/")==false)
209     creardir(dirNONPro, diris);
210                     dirNONProgroup=dirNONPro+ene+"/"+group+"/";
211                     File.rename(imagepath, dirNONProgroup+imagename);
212             }
213             else{
214                     roiManager("Save", dirRoisgroup+raiz+".zip");
215                     roiManager("Deselect");
216                     roiManager("Delete");
217                     File.rename(imagepath, dirProgroup+imagename);
218             }
219             selectWindow(imopen);
220             close();
221
222
223     }
224
225     function Lineseparator() {
226             lines=0;
227             while(lines==0){
228                     selectWindow(imopen);
229                     setTool("line");
230                     waitForUser("Please draw lines and add to the ROi manager");
```

```
231                     lines=roiManager("count");
232                     if (lines>0){
233                             for (i=0; i<lines; i++){
234                                     roiManager("Select", i);
235                                     run("Line to Area");
236                                     run("Enlarge...", "enlarge=2 pixel");
237                                     setBackgroundColor(0, 0, 0);
238                                     run("Clear");
239                             }
240                             roiManager("Deselect");
241                             roiManager("Delete");
242                     }
243                     else{
244                             nolines=getBoolean("No lines, do you want to retry without
245     lines?");
246                             if (nolines==true) lines=-1;
247                     }
248             }
249
250     }
251
252
```

1.1.2. Macros used to analyse mitochondrial morphology

```
/*
   MitoProt_analyzer is an ImageJ macro developed to analyze mitochondria,
protein levels and colocalization
   Copyright (C) 2014  Jorge Valero Gómez-Lobo.

   MitoProt_analyzer is free software: you can redistribute it and/or modify
it under the terms of the GNU General Public License as published by
the Free Software Foundation, either version 3 of the License, or
   (at your option) any later version.

   MitoProt_analyzer is distributed in the hope that it will be useful,
but WITHOUT ANY WARRANTY; without even the implied warranty of
   MERCHANTABILITY or FITNESS FOR A PARTICULAR PURPOSE.  See the
   GNU General Public License for more details.

   You should have received a copy of the GNU General Public License
along with this program.  If not, see <http://www.gnu.org/licenses/>.
*/

//This macro has been developed by Dr Jorge Valero (jorge.valero@cnc.uc.pt).
//If you have any doubt about how to use it, please contact me.

//License
Dialog.create("GNU GPL License");
Dialog.addMessage(" MitoProt_analyzer  Copyright (C) 2014 Jorge Valero Gomez-
Lobo.");
Dialog.setInsets(10, 20, 0);
Dialog.addMessage(" MitoProt_analyzer  comes with ABSOLUTELY NO WARRANTY;
click on help button for details.");
Dialog.setInsets(0, 20, 0);
Dialog.addMessage("This is free software, and you are welcome to redistribute it
under certain conditions; click on help button for details.");
Dialog.addHelp("http://www.gnu.org/licenses/gpl.html");
Dialog.show();


//This Macro does not work adequately using Batchmode

//This is a global variable that it will be used by infoTab to substitute return;
var infovar=0;

//Dialog of initial parameters

Dialog.create("MITOCHONDRIA PARAMETERS");

Dialog.addNumber("Background subtraction rollingball radius:", 10)
```

```
299
300 Dialog.addMessage("FIND FOCI parameters")
301 Dialog.addNumber("Gaussian blur:", 0.5);
302  Dialog.addNumber ("Absolute threshold:", 10);
303 Dialog.addNumber("Peak Search parameter", 0.3);
304 Dialog.addNumber("Peak fusion parameter", 0.5);
305 Dialog.addNumber("Minimum size", 5);
306  Dialog.show();
307
308 rolling=Dialog.getNumber();
309 gaussian=Dialog.getNumber();
310 backparam=Dialog.getNumber();
311 searchparam=Dialog.getNumber();
312 peakparam=Dialog.getNumber();
313 minsize=Dialog.getNumber();
314
315
316
317
318
319 //This helps to localize the folders
320
321 dir=getDirectory("Please, select the initial folder");
322 dirRois=dir+"ROIS"+File.separator;
323 dirPro=dir+"Processed"+File.separator;
324 if (File.exists(dir+"Results/")==false) File.makeDirectory(dir+"Results");
325 dirRes=dir+"Results"+File.separator;
326
327
328 //detect Images folder
329 level1=getFileList(dir);
330 i=0;
331 while (i<level1.length) {
332         if (level1[i]=="Processed/") imagedir=dir+level1[i];
333         i++;
334 }
335         //error message if no Processed folder exists
336         if (i==level1.length+1){
337                 showMessage("NO Processed folder found");
338                 beep();
339                 exit();
340         }
341
342         //detect n folder
343         level2=getFileList(imagedir);
344         for (i=0; i<level2.length; i++) {
345                 ene=File.getName(imagedir+level2[i]);
```

```
346                     enesem=substring(ene, 1);
347                     summtables();
348                     if (endsWith(level2[i], "/")){
349                             direne=imagedir+level2[i];
350
351                             //detect group folder
352                             level3=getFileList(direne);
353                             for (ii=0; ii<level3.length; ii++){
354                                     group=File.getName(direne+level3[ii]);
355                                     diris=newArray(ene, group);
356                                     dirRoisgroup=dirRois+ene+"/"+group+"/";
357                                     if (File.exists(dirRes+ene+"/"+group+"/")==false)
358 creardir(dirRes, diris);
359                                     dirResgroup=dirRes+ene+"/"+group+"/";
360                                     if (endsWith(level3[ii], "/")){
361                                             dirgroup=direne+level3[ii];
362
363                                             //detect images
364                                             level4=getFileList(dirgroup);
365                                             sptables();
366                                             for (iii=0; iii<level4.length; iii++){
367                                                     imagepath=dirgroup+level4[iii];
368                                                     work();
369                                             }
370                             }
371                             printsumm();
372                     }
373                     savesumm();
374
375             }
376 }
377
378
379
380
381 function work(){
382         run("Bio-Formats Importer", "open=["+imagepath+"] color_mode=Default
383 open_files view=Hyperstack stack_order=XYCZT");
384
385         //get image name;
386         imopen=getTitle();
387         imagename=File.name;
388         raiz=File.nameWithoutExtension;
389         getPixelSize(unit, pixelWidth, pixelHeight);
390
391         //open rois
392         roiManager("Open", dirRoisgroup+raiz+".zip");
```

```
393		rois=roiManager("count");
394		Roiarea=0;
395		//analyze each roi
396		for (iroi=0; iroi<rois; iroi++){
397			selectWindow(imopen);
398			roiManager("Select", 0);
399			roiManager("Measure");
400			Roiarea=getResult("Area", iroi);
401			mitos();
402			closing();
403			}
404
405		selectWindow(imopen);
406		close();
407	}
408
409
410	function mitos(){
411		run("Duplicate...", "title=Duplicate duplicate channels=1-4");
412		roiManager("Add");
413		roiManager("Deselect");
414		run("Duplicate...", "title=Mitos duplicate channels=1");
415		run("Set Measurements...", "area perimeter shape feret's area_fraction
416	redirect=None decimal=3");
417		selectWindow("Mitos");
418		run("Grays");
419		run("Subtract Background...", "rolling="+rolling);
420		run("FindFoci", "mask=[None] background_method=Absolute
421	background_parameter="+backparam+" auto_threshold=Otsu statistics_mode=Both
422	search_method=[Fraction of peak - background] search_parameter="+searchparam+"
423	minimum_size="+minsize+" minimum_above_saddle minimum_peak_height=[Relative
424	above background] peak_parameter="+peakparam+" sort_method=[Total intensity]
425	maximum_peaks=1000000000 show_mask=Threshold fraction_parameter=1.0
426	gaussian_blur="+gaussian+" centre_method=[Max value (search image)]
427	centre_parameter=2.0");
428		run("Set Scale...", "distance=1 known="+pixelWidth+" pixel=1 unit="+unit);
429		setAutoThreshold("Default dark");
430		setOption("BlackBackground", false);
431
432		run("Duplicate...", "title=MaskMit");
433		setThreshold(2, 276);
434		run("Convert to Mask");
435		run("Analyze Particles...", "size=1-Infinity pixel display summarize add");
436		//waitForUser("");
437		selectWindow("Mitos FindFoci");
438		close();
439		selectWindow("MaskMit");
```

```
440		rename("Mitos FindFoci");
441		roiManager("Select", 0);
442		roiManager("Delete");
443		TOTROIS=roiManager("count");
444		inirois=rois-iroi;
445		ROIS=TOTROIS-inirois;
446		mitoarr=newArray(ROIS);
447		for (i=0; i<ROIS; i++) mitoarr[i]=i+inirois;
448		roiManager("Select", mitoarr);
449		roiManager("Combine");
450		roiManager("Add");
451		roiManager("Select", mitoarr);
452		roiManager("Delete");
453		roiManager("Select", inirois);
454		setBackgroundColor(0, 0, 0);
455		run("Clear");
456		selectWindow("Mitos");
457		close();
458
459
460		//take values
461		infoTab("Summary", 1, 3);
462		area=infovar;
463		infoTab("Summary", 1, 5);
464		perim=infovar;
465		Round=0;
466		AR=0;
467		perim=0;
468		areabis=0;
469		selectWindow("Results");
470		ress=getInfo();
471		row=split(ress, "\n");
472		limit=row.length-1;
473		for(irow=0; irow<limit; irow++){
474			Round=Round+getResult("Round", irow);
475			AR=AR+getResult("AR", irow);
476			perim=perim+getResult("Perim.",irow);
477			areabis=areabis+getResult("Area",irow);
478		}
479		Round=Round/limit;
480		AR=AR/limit;
481		selectWindow("Mitos FindFoci");
482		roiManager("Select", inirois-1);
483		run("Measure");
484		perArea=getResult("%Area", limit);
485
486
```

```
487             //populate tables
488             tablearray=newArray(ene, group, imagename, iroi, Roiarea, area, perim,
489     Round, AR, perArea);
490             tableprinter(ene+ group+ " Mit parameters", tablearray);
491
492
493             selectWindow("Results");
494             run("Close");
495             selectWindow("Summary");
496             run("Close");
497     }
498
499
500
501     function creardir(inidir, pathes){
502             for (i=0; i<pathes.length; i++){
503                     File.makeDirectory(inidir+pathes[i]);
504                     inidir=inidir+pathes[i]+"/";
505             }
506
507     }
508
509
510     function tablecreator(tabname, tablearray){
511             run("New... ", "name=["+tabname+"] type=Table");
512             headings=tablearray[0];
513             for (i=1; i<tablearray.length; i++)headings=headings+"\t"+tablearray[i];
514             print ("["+tabname+"]", "\\Headings:"+ headings);
515
516     }
517
518     function tableprinter(tabname, tablearray){
519             line=tablearray[0];
520             for (i=1; i<tablearray.length; i++) line=line+"\t"+tablearray[i];
521             print ("["+tabname+"]", line);
522
523     }
524
525
526     //This function obtains info from Threshold table channel "chann" and column
527     "column", values should be numeric
528
529     function infoTab(tablename, line, column){
530             selectWindow(tablename);
531             tableinfo=getInfo();
532             Ltab=split(tableinfo, "\n");
533             Ctab=split(Ltab[line], "\t");
```

```
534             infovar=Ctab[column];
535     }
536
537     function copytable(oldname, newname){
538             first=0;
539             if (isOpen(newname)==false) {
540                     run("New... ", "name=["+newname+"] type=Table");
541                     first=1;
542             }
543             selectWindow(oldname);
544             tableinfo=getInfo();
545             linetable=split(tableinfo, "\n");
546             for (t=0; t<linetable.length; t++){
547             if (t==0 && first==1) print("["+newname+"]","\\Headings:"+linetable[t]);
548             else if (t!=0) print("["+newname+"]",""+linetable[t]);
549             }
550     }
551
552     function mean(oldname, newname){
553             first=0;
554             if (isOpen(newname)==false) {
555                     run("New... ", "name=["+newname+"] type=Table");
556                     first=1;
557             }
558             selectWindow(oldname);
559             tableinfo=getInfo();
560             linetable=split(tableinfo, "\n");
561             for (t=0; t<linetable.length; t++){
562             if (t==0 && first==1) print("["+newname+"]","\\Headings:"+linetable[t]);
563             else if (t!=0) print("["+newname+"]",""+linetable[t]);
564             }
565     }
566
567     function  savetab(tablename, dirdest){
568                     selectWindow(tablename);
569                     saveAs("Text", dirdest+tablename+".xls");
570             }
571
572     function closing(){
573             selectWindow("Mitos FindFoci");
574             close();
575             selectWindow("Duplicate");
576             close();
577             rois=roiManager("Count");
578             for (i=1; i<3; i++){
579                     roiManager("Select", rois-i);
580                     roiManager("Delete");
```

```
581             }
582     }
583
584
585
586     function sptables(){
587             //creating tables
588                     tablearray=newArray("Exp group", "Genotype", "Image", "ROI",
589     "ROIArea", "Area", "Perimeter", "Round", "AR", "% Area Mit into cells");
590                     tablecreator (ene+ group+ " Mit parameters", tablearray);
591
592     }
593
594     function summtables(){
595             //creating tables
596                     tablearray=newArray("Exp group", "Genotype", "Area",
597     "Perimeter", "Round", "AR", "% Area Mit into cells");
598                     tablecreator (ene+" Summary Mit parameters", tablearray);
599
600     }
601
602     function printsumm(){
603
604             meandata(ene+ group+ " Mit parameters", ene+" Summary Mit parameters",
605     "");
606             savetab(ene+ group+ " Mit parameters", dirResgroup);
607             selectWindow(ene+ group+ " Mit parameters");
608             run("Close");
609
610     }
611     //print mean tables
612     function meandata(datatab, destinytab, extra){
613             selectWindow(datatab);
614             tableinfo=getInfo();
615             linetable=split(tableinfo, "\n");
616             if (linetable.length>1){
617             coltable=split(linetable[1], "\t");
618             means=newArray(coltable.length-2);
619             infoTab(datatab, 1, 0);
620             means[0]=infovar;
621             infoTab(datatab, 1, 1);
622             means[1]=infovar+" "+extra;
623             for(c=4; c<coltable.length; c++){
624                     n=0;
625                     for (t=1; t<linetable.length; t++){
626                             infoTab(datatab, t, c);
627                             infovar=parseFloat(infovar);
```

```
628                             means[c-2]=means[c-2]+infovar;
629                             n++;
630                     }
631                     means[c-2]=means[c-2]/n;
632             }
633             tableprinter(destinytab, means);
634             }
635     }
636
637     function savesumm(){
638             savetab(ene+" Summary Mit parameters", dirRes+ene+"/");
639             selectWindow(ene+" Summary Mit parameters");
640             run("Close");
641
642     }
643
```

2. Supplementary Data

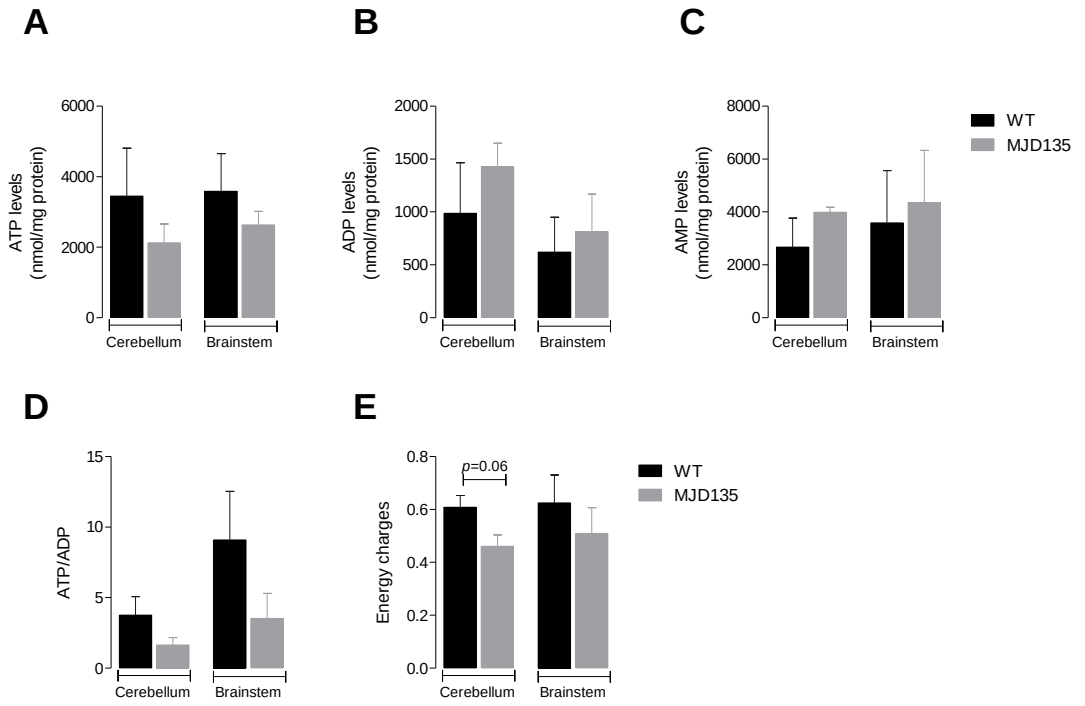

Figure S1 - Unchanged levels of adenine nucleotides in MJD135 mouse cerebellum and brainstem.

Total extracts from cerebellum and brainstem of 24-week-old MJD135 and WT mice were performed with 0.6 M perchloric acid supplemented with 25 mM EDTA-Na^+. The total levels of ATP (**A**), ADP (**B**), and AMP (**C**) were determined by reverse phase HPLC with a detection wavelength of 254 nm. The ATP/ADP ratio is presented in (**D**) and the variations in energy charges were determined as ([ATP]+0.5 [ADP])/([ATP]+[ADP]+[AMP]) and are presented in (**E**). Data are mean ± SEM of 3-4 mice from each genotype, run in triplicates.

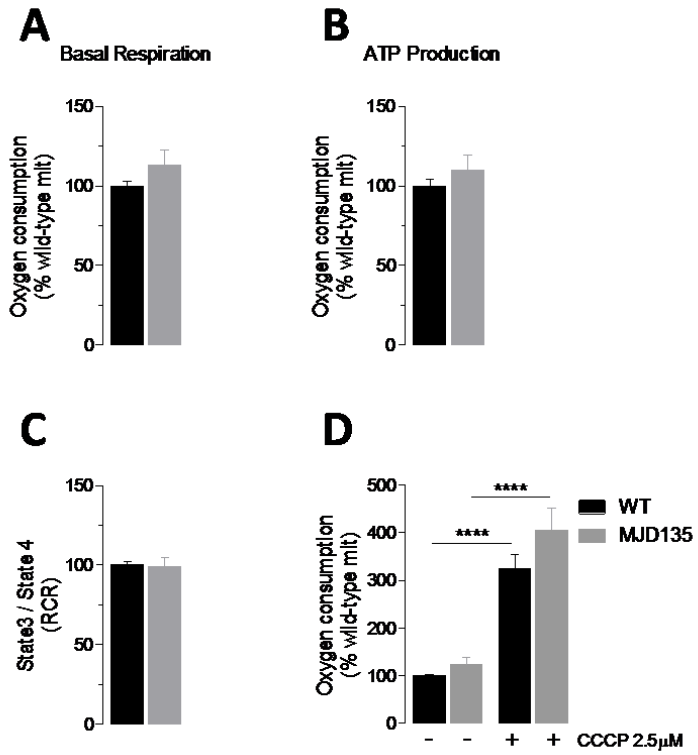

Figure S2 - MJD135 mice show no differences in brainstem mitochondrial oxygen consumption by the oxygraph apparatus.

Mitochondria were isolated from the brainstem of 24-week-old MJD135 and WT mice. The rate of oxygen (O_2) consumption was measured at 30°C, using an O_2 Clark electrode before (**A**) and after sequential addition of 3 mM succinate, 25 µM ADP, 2 µg/mL oligomycin and 2 µM CCCP. The phosphate/oxygen (P/O) ratio is represented in (**B**) and expresses the relation between ATP synthesis and O_2 consumption after addition of ADP. The respiratory control ratio (RCR) (**C**) was calculated through the ratio between the rates of O_2 consumption in the absence (state 4) and in the presence (state 3) of ADP. Maximal respiration was achieved following addition of CCCP (**D**). Data are mean ± SEM of 5 mice from each genotype, run in duplicates. Statistical analysis was performed by Student's *t*-test for (**A**-**C**). In (**D**) Statistical analysis was performed, by two-way ANOVA, and Bonferroni post-hoc test: $^{****}p<0.0001$.

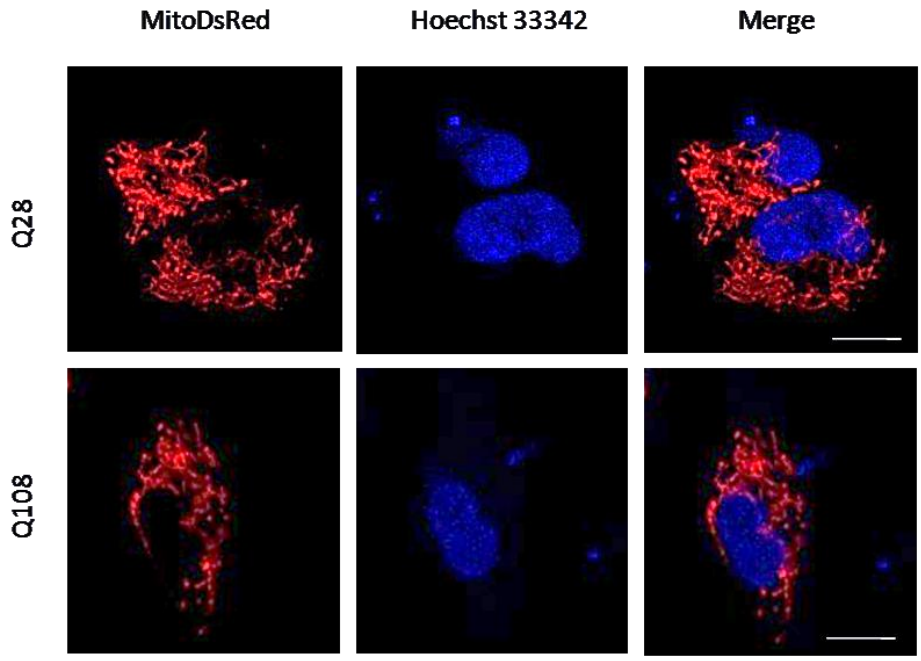

Figure S3 - Labeling of mitochondria in PC6-3 cells.

Confocal images of PC6-3 cells were obtained with a 63x objective, NA=1.4 on a Zeiss LSM 70 inverted microscope. PC6-3 cells (Q28 and Q108) were transfected with the plasmid MitoDsRed, which labels mitochondria, and stained with Hoechst 33342 in order to visualize the nuclei. Scale bar: 10 µm.